SETCOR
Conferences & Exhibitions

The International Nanotechnology & Nanoscience Conference & Exhibition

Nanotech France 2018

June 27 to 29, 2018, Paris - France

Conference Proceedings

DOI: https://doi.org/10.26799/cp-nanotechfrance2018

Proceedings of the Nanotech France 2018
Paris -, France – June 27 – 29, 2018
DOI: https://doi.org/10.26799/cp-nanotechfrance2018

Biopolymer nanofiber doped with nanospinels by electrospinning and microbiological assays

Christian Cruzat [1,2], Eulalia Vanegas[1,2*], Denisse Peña[3], Ramón Arrue[4], Nestor Novoa[4], Guillermina Pauta[5], Diego Ponce[5], Gabriela Vazquez[5], Octavio Peña[6]

[1]University of Cuenca, CEA (Centre for Enviromental Studies), Cuenca – Ecuador
[2]University of Cuenca, Faculty of Chemistry Sciences, Cuenca – Ecuador
christian.cruzat@ucuenca.edu.ec
eulalia.vanegas@ucuenca.edu.ec

[3]University of Cuenca, Faculty fo Agrocultural Sciences, Cuenca – Ecuador
denisse.peña@ucuenca.edu.ec

[4]University of Concepción, Faculty of Chemistry Sciences, Concepción – Chile
nenovoa@udec.cl
rarrue@udec.cl

[5]University of Cuenca, Engineering Faculty, Cuenca – Ecuador
diego.ponce@ucuenca.edu.ec
guillermina.pauta@ucuenca.edu.ec
gabriela.vazquez@ucuenca.edu.ec

[6]Sciences Chimiques de Rennes, UMR 6226, Université de Rennes1, Rennes – France
octavio.pena@univ-rennes1.fr

Abstract

Aim of this work was investigated the change in physical-chemical properties of biopolymer (poly(lactic acid)(PLA)) nanofiber doped with magnetic nanospinels and study of antimicrobial activity of these matrix for a possible use as fungical or carrier drug used in the organic farming. The spinel nanoparticles ($Ni_{0.5}Fe_{2.5}O_4$) were synthesized by Sol-gel method and the incorporation to polymeric matrix was performed by impregnation method and nanofiber synthetized by electrospinning. Nanoparticles were characterized by FESEM, DRX and SQUID. PLA was characterized by SEM and DSC and nanoparticles supported on biopolymer were characterized by DSC and were realized bioassays (antibiograms in font to *Fusarium sp*). Through powder X-rays, the average crystalline size of nanoparticles was determined using Scherrer's formula and the network parameters by FullProf suite, via Rietveld's method. The average size measurements were between 5 nm and 35 nm. Magnetic susceptibility measurements were performed to determine the blocking temperature of the nanoparticles, the compounds present magnetic irreversibility at room temperature. The nanofiber characterization by SEM showed that all fibers have nanometric size. In addition, bioassays of nanoparticles showed an inhibitory activity for different concentration of nanoparticles, by contrast in biopolymer nanofiber doped with nanospinels no showed activity in a preliminary test. These results suggest a possible use of nanofibers with a higher concentration of nanoparticles as organic fungicides.

Keywords: nanoparticles, nanofibers, electrospinning, biopolymer, nanomagnetism

1. Introduction

In the last decade, nanoparticles have got increasingly importance in science and technology because both common and sophisticated devices can be made with these materials [1,2]. it is possible to use nanoparticles in technological applications because new chemical and physical phenomena appear when the metric scale decreases below 100 nm [3]. the aim of this work was proposed to investigate the capabilities of encapsulation of biopolymer (poly(lactic acid)(PLA)) nanofiber doped with magnetic nanospinnels and study of antimicrobial activity of these matrix for a possible use as fungicidal or carrier drug used in the organic farming [4]. Today, pest control depends mainly on the use of synthetic agrochemicals, which has

DOI: https://doi.org/10.26799/cp-nanotechfrance2018

increased the population of resistant phytopathogens, causing a significant increase in production costs and serious pollution problems. [5] As a result, global markets for certified organic products have grown dramatically in recent years. A fungicide of plant origin such as biopolymers (PLA), increasing its action with the use of metal nanoparticles (Ni, Fe), to be applied in the production of organic products, would be a very good alternative as a fungicidal.

2. Experimental Part

The nanoparticles synthesis was realized by Sol-gel method (Figure 1a)[6], All reagents were of analytical grade. Iron (III) nitrate nonahydrate, nickel (II) nitrate hexahydrate, citric acid and ethylene glycol were purchased from Aldrich. Metal reagents (nickel and iron nitrates) were dissolved separately in distilled water with a specific molar relation, depending on the desired stoichiometry[7]. Citric acid was added under strong stirring, keeping a metal/acid ratio of 1:2. The solution was heated at 60°C for 4 hours adding ethylene glycol in a ratio of 1:2 with respect to citric acid. The sample was dried in an oven at 90°C overnight. A brown dense gel was then formed. The calcination temperature profile was as follows: from room temperature to 450°C at 3°C/min, kept at 450°C for 180 minutes, and cooled from 450°C to room temperature at 3°C/min. After that, the compound was pulverized into a mortar and pressed into pellets for further analysis. Incidentally, Nanoparticles with PLA (260000 g/mol) will be dissolved in a 3/7 vol/vol mixture of dimethylsulfoxide (DMS) and dichlorometane (MC) in water/acetic acid to achieve a polymer concentration of 2 wt% in solution. The process will be conducted at room temperature using a magnetic stirrer until complete polymer dissolution. The polymer solution (10g) will be placed in a commercial plastic syringe (10mL) fitted with a steel needle (gauge 20). Electrospinning will be conducted by applying a voltage between 12kV. A syringe pump (from Syringepump) fed the polymer solution into the needle tip at a rate between 2 ml/h. The electrospun fibers will be collected on a grounded collecting drum placed 10 cm away from the needle at room temperature. The linear rate of the rotating disk at edge was set to 1000rpm (Figure 1b).

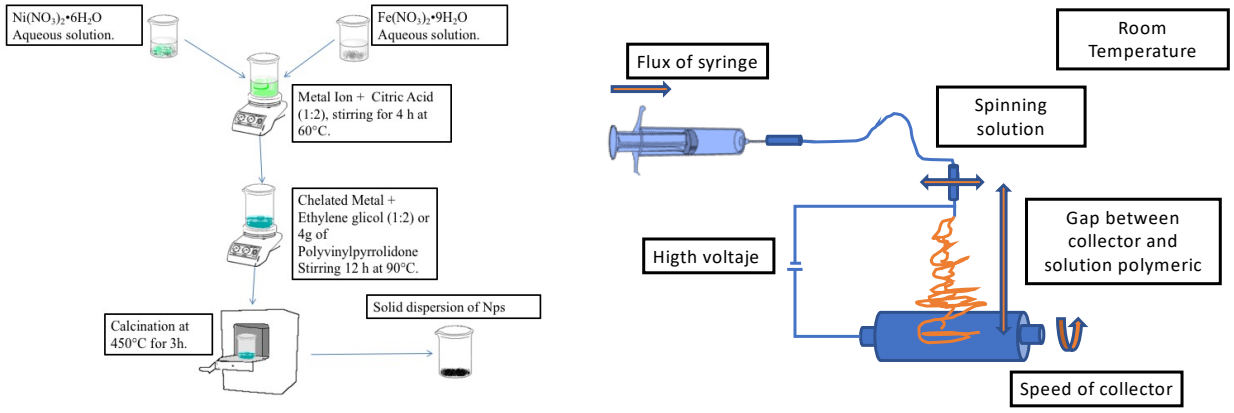

Figure 1. a) Sol-gel method for obtaining nanoparticles, b) Scheme of electrospinning machine

Nanoparticles was analyzed by FESEM, DRX, SEM, SQUID, DSC of PLA nanofibers with and without nanoparticles was also carried out and an antibiogram analysis was made for observed the behavior of nanoparticles in front to a fungical microorganism.

3. Results and Discussion

Field Emission Scanning Electron Microscopy (FESEM)

The morphologies of the Nps were analyzed by field-emission scanning electron microscopy. All compounds showed particles agglomerates, no-homogenous and pores on the surface, the Nps has a spherical shape. After a post-synthetic procedure, the nanoparticles showed a drastic modification, maybe in their crystal habit or in their crystal space orientation. By crushing the samples into a mortar, this morphology was modified to a laminar shape, the samples being of spherical and laminar specimens, this change in the structure by used of mortar is the basis of mechanic synthesis techniques of

DOI: https://doi.org/10.26799/cp-nanotechfrance2018

nanocomposites[8]. FESEM Micrography in Figure 2a it is possible to appreciate the distribution size of the nanoparticles, but after a post-process in the manufacture of nanoparticle tablets, it possible to appreciate a change of conformation was observed in a portion of nanoparticles, which are more agglomerated and compacted, it showing a close relationship between nanoparticles (Figure 2b).

a) 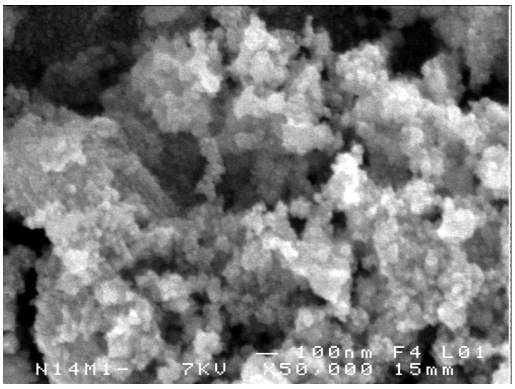

b) 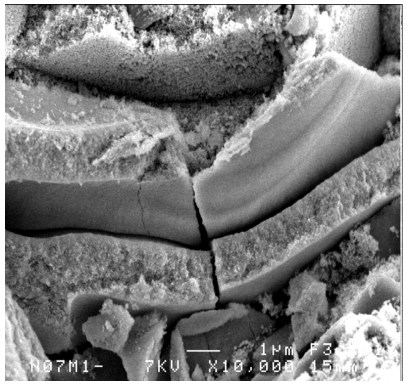

Figure 2. a) FESEM micrographs of $Ni_{0.5}Fe_{2.5}O_4$ Nps before a modification b) FESEM micrographs of $Ni_{0.5}Fe_{2.5}O_4$ Nps after a mortar procedure.

SQUID analysis

Magnetic susceptibility of Nps was measured in a superconducting quantum interference device magnetometer (SQUID, Quantum Design MPMS XL5), under an applied field of 1,000 Oe (0.1 T), from 5 to 300 K, and as a function of magnetic field, from 0 to 5 T at two temperatures (5 and 300 K). The samples were compacted on discs (50–80 mg) for further encapsulation in polystyrene of negligible contribution. One important parameter in nanomagnetism is the so-called "blocking temperature" (T_B) at which the particle moment appears blocked with respect to the time scale of the experiment. Magnetization measurements (ZFC/FC cycles) were performed at 100 Oe and are shown in Fig. 3. The analysis usually involves two well-known temperatures: the "blocking temperature" (T_B) at which the ZFC magnetization reaches a maximum value and the "irreversibility temperature" (T_{irr}) above which, the system shows a reversible behavior. These two temperatures, T_B and T_{irr}, are clearly visible in some nanoparticles but, It is important to note that for $Ni_{0.5}Fe_{2.5}O_4$ Nps (Fig.3) both the blocking and irreversibility temperatures are much higher than room temperature. This result may be correlated to a large distribution of particle sizes, as seen in the FE-SEM images. Thus, these nanospinel are very interesting candidates for hyperthermia treatments, as reported by Davila-Ibañez et al.[9], since they would present a large magnetic hysteresis that could be transferred as heat when subjected to an oscillating field.

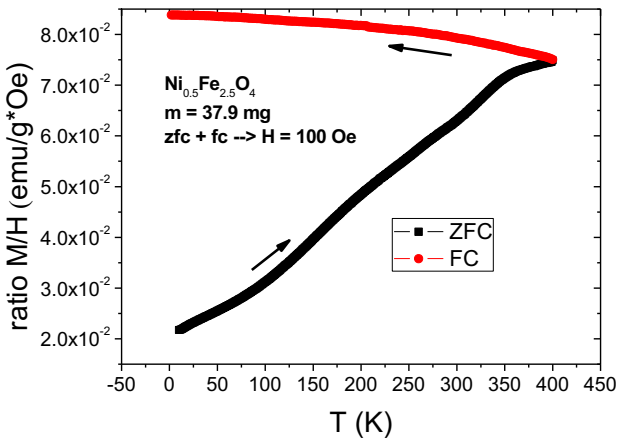

Figure 3. ZFC / FC cycles

DOI: https://doi.org/10.26799/cp-nanotechfrance2018

X-ray Powder Diffraction (XRD)

The identification and structural analysis of the phase spinel was obtained from powder X-ray diffraction data using the FullProf program and Rietveld method. Peaks shape was assumed through a Pseudo-Voigt function, background was fixed with a polynomial function of 6 factors, a correction by peaks asymmetry was made and also it was refined the zero point. No correction by preferential orientation was made. The residual factors are given in table 1: Profile Factor (R_p), Weighted Profile Factor (R_{wp}), Expected Weighted Profile Factor (R_{exp}) and value of the "goodness-of-fit" (χ^2). Fig. 4 shows the XRD patterns, which confirm that all compounds had the spinels structure. Due to the small size of the particles, the XRD patterns showed broad peaks and an important background, as it may occur in amorphous materials; despite of this, it was possible to index all diffractograms by using the FullProf program.

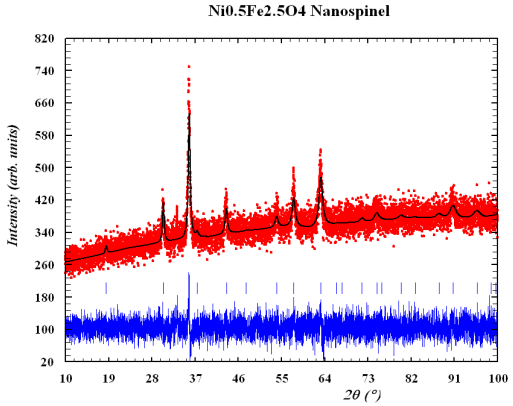

Figure 4. X ray diffraction pattern

Table 1: Structural parameters of Nps, data obtained by the Rietveld method and sizes calculated by powder X-ray.

Name	Space grupe	a /Å	c /Å	Cell volumen/Å^3	d(cristal size)/nm
$Ni_{0.5}Fe_{2.5}O_4$	$Fd\bar{3}m$	8.317297	8.317297	575.369 (0.707)	10

Scanning Electron Microscopy (SEM)

Scanning electron microscopy analysis for $Ni_{0.5}Fe_{2.5}O_4$ Nps showed in Figure 5, the analysis concludes a possible structural formula derived from the composition analyzed on its surface.

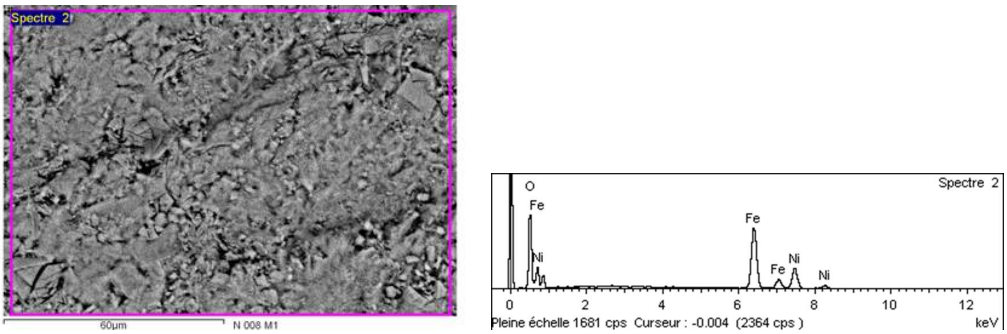

sample	Initial molar of Ni	Initial molar of Fe	% Atoms Ni K	% Atoms Fe K	% Atoms O K	Stoichiometry estimated
$Ni_{0.5}Fe_{2.5}O_4$	0,005	0,01	12.30	26.34	61.36	$NiFe_{2.14}O_{4.99}$

Figure 5. Nanoparticles micrograph and their composition

DOI: https://doi.org/10.26799/cp-nanotechfrance2018

It is possible observed in Figure 6 the SEM of PLA nanofiber synthetized by electrospinning technique, the nanofibers presented in the sample have nanometric size from 96 to 136 nm.

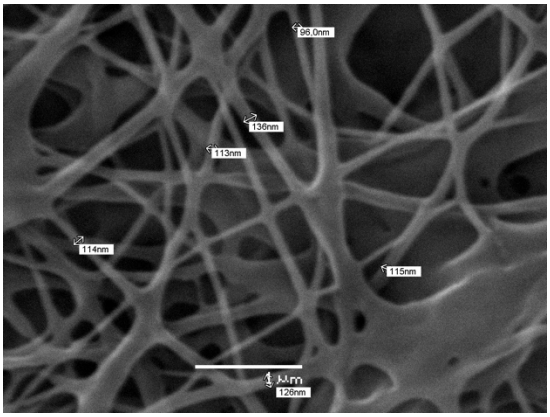

Figure 6. PLA nanofibers SEM micrographs

DSC thermograms

The PLA nanofiber and PLA nanofiber/nanospinels were semi-crytalline polymer under the measurement conditions. During the first heating, polymer thermograms consist of a glass transition ($T_{g,n}$ = 57°C, $T_{g,n/n}$ = 60°c), crystallization exotherms ($T_{c,n}$ = 77°C, $T_{c,n/n}$ = 80°C) and melting endotherm peaks ($T_{m,n}$= 179°C, $T_{m,n/n}$ = 178°C). The glass transition and crystallization behavior shift to higher temperature when nanospinels were added into nanofibers, indicating that the mobility of macromolecules chain was affected and crystallization kinetics too, while the melting point was not influenced by the incorporation of nanoparticles.

Antibiograms

Antibiograms of $Ni_{0.5}Fe_{2.5}O_4$ nanoparticles in font to *Fusarium sp,* fungi from Solanum Betaceum was carried out. It is possible to see an inhibition ring present in petri dishes containing different amounts of nanoparticles (Figure 7)

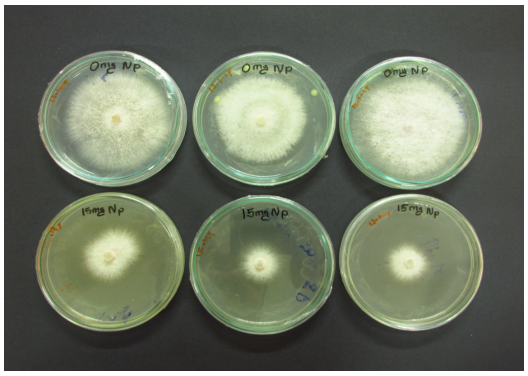

Figure 7. test of up) Fungi down) 15 mg of nanoparticles in fungi

4. Conclusions

Nanoparticles of small size compared to other elaboration techniques were obtained by the Pechini method. The quite homogeneous compounds were obtained at low temperature of synthesis. The X-ray powder diffraction confirms their spinel structural type, similar to the macroscopic compounds. Magnetization measurements showed in the ferrite nanoparticles, the blocking temperatures occurred above room temperature, which makes these compounds to be good candidates for their use

DOI: https://doi.org/10.26799/cp-nanotechfrance2018

in hyperthermia. SEM analyses showed that it is possible to obtain a nanofiber of PLA with a homogeneous form by electrospinning. On the other hand, microbiological tests showed that Nps have fungal activity in front to *Fusarium sp*, while nanoparticles supported in PLA, not showed clear activity, this can be associated to the fact that the amount of nanoparticle supported in the biopolymer is not appropriate.

Acknowledgements

The authors thanks to DIUC, BECACHILE and CONICYT for financial support, to UMR—CNRS 6226, and the Microscopy Center of Université de Rennes1

References

1. Zhao, L., Deng, J., Sun, P., Liu, J., Ji, Y., Nakada, N., … Yang, Y. (2018). "Nanomaterials for treating emerging contaminants in water by adsorption and photocatalysis: Systematic review and bibliometric analysis". *Science of the Total Environment*, 627, 1253–1263.
2. Ahmad, R., Mahmoudi, T., Ahn, M. S., & Hahn, Y. B. (2018). "Recent advances in nanowires-based field-effect transistors for biological sensor applications". *Biosensors and Bioelectronics*, *100*(September 2017), 312–325.
3. Cárdenas, G., Sáez, V., & Cruzat, C. (2017). "Preparation of Gold Nanoparticles Using 2-Ethoxyethanol, 2-Methoxyethanol and 1,3-Butyleneglycol Supported in Chitosan". *Journal of Cluster Science*, *28*(3), 1127–1144.
4. El Beyrouthya, M. (2014). "Nanotechnologies: Novel Solutions for Sustainable Agriculture". *Advances in Crop Science and Technology*, *02*(03), 8863.
5. Justino, C. I. L., Gomes, A. R., Freitas, A. C., Duarte, A. C., & Rocha-Santos, T. A. P. (2017). "Graphene based sensors and biosensors". *TrAC - Trends in Analytical Chemistry*, *91*, 53–66.
6. Cárdenas-Triviño, G., Elgueta, C., Vergara, L., Ojeda, J., Valenzuela, A., & Cruzat, C. (2017). "Chitosan doped with nanoparticles of copper, nickel and cobalt". *International Journal of Biological Macromolecules*, *104*, 498–507.
7. Durán, P.; Tartaj, J.; Rubio, F.; Moure, C.; Peña, O. (2004) "Preparation and Powder Characterization of Spinel-Type CoxNiMn2−xO4 (0.2⩽x⩽1.2) by the Ethylene Glycol–metal Nitrate Polymerized Complex Process". *J. Eur. Ceram. Soc.*, 24, 3035–3042.
8. Nazemi, M. K.; Sheibani, S.; Rashchi, F.; Gonzalez-DelaCruz, V. M.; Caballero, A. (2012) "Preparation of Nanostructured Nickel Aluminate Spinel Powder from Spent NiO/Al2O3 Catalyst by Mechano-Chemical Synthesis". *Adv. Powder Technol.*, 23, 833–838.
9. Davila-Ibanez, A. B.; Salgueirino, V.; Martinez-zorzano, V.; Mariño-Fernández, R.; García-Lorenzo, A.; Maceira-Campos, M.; Muñoz-Ubeda, M.; Junquera, E.; Aicart, E.; Rivas, J.; et al.(2012) "Magnetic Silica Nanoparticle Cellular Uptake and Cytotoxicity Regulated by Electrostatic Polyelectrolytes-DNA Loading at Their Surface". *ACS Nano*, 6, 747–759.

Proceedings of the Nanotech France 2018 International Conference (Nanotech France 2018)
Paris, France, June 27 - 29, 2018
DOI: https://doi.org/10.26799/cp-nanotechfrance2018

Design of Polyelectrolyte Microcapsules Encoded with Excitonic Nanoparticles and Prospects of Their Applications as Novel Bioimaging and Theranostic Tools

G. Nifontova[1], M. Zvaigzne[2], M. Baryshnikova[3], E. Korostylev[4], F. Ramos-Gomes[5], F. Alves[6], I. Nabiev[7], A. Sukhanova[8]

[1] National Research Nuclear University MEPhI (Moscow Engineering Physics Institute)
Kashirskoye Shosse 31, 115409 Moscow, Russian Federation, nifontovago@gmail.com
[2] National Research Nuclear University MEPhI (Moscow Engineering Physics Institute)
Kashirskoye Shosse 31, 115409 Moscow, Russian Federation, mariazvaigzne@gmail.com
[3] National Research Nuclear University MEPhI (Moscow Engineering Physics Institute)
Kashirskoye Shosse 31, 115409 Moscow, and
N.N. Blokhin National Medical Research Center of Oncology
Kashirskoye Shosse 24, 115478 Moscow, Russian Federation, ma_ba@mail.ru
[4] Moscow Institute of Physics and Technology (State University),
Institutskiy per. 9, 141701 Dolgoprudny, Moscow Region, Russian Federation, golavl.itachi@gmail.com
[5] Translational Molecular Imaging, Max-Planck-Institute of Experimental Medicine
Hermann Rein-Str. 3, D37075 Göttingen, Germany, ramos@em.mpg.de
[6] Translational Molecular Imaging, Max-Planck-Institute of Experimental Medicine
Hermann Rein-Str. 3, D37075 Göttingen, Germany, and
Clinic of Haematology and Medical Oncology, University Medical Center Göttingen
Robert Koch-Str. 40, 37075 Göttingen, Germany, falves@gwdg.de
[7] National Research Nuclear University MEPhI (Moscow Engineering Physics Institute)
Kashirskoye Shosse 31, 115409 Moscow, Russian Federation, and
Laboratoire de Recherche en Nanosciences (LRN-EA4682), Université de Reims Champagne-Ardenne
rue Cognacq Jay 51, 51095 Reims, France, igor.nabiev@univ-reims.fr
[8] National Research Nuclear University MEPhI (Moscow Engineering Physics Institute)
Kashirskoye Shosse 31, 115409 Moscow, Russian Federation, and
Laboratoire de Recherche en Nanosciences (LRN-EA4682), Université de Reims Champagne-Ardenne
rue Cognacq Jay 51, 51095 Reims, France, alyona.sukhanova@univ-reims.fr

Abstract
The use of microparticles, in particular, polyelectrolyte microcapsules as carriers of active pharmaceutical ingredients, fluorescent dyes, and specific diagnostic bioconjugates has been proved to be a promising approach to development of bioimaging and theranostic tools. Excitonic nanoparticles, namely, fluorescent semiconductor nanocrystals referred to as quantum dots (QDs) have high photostability and brightness, wide absorption spectra, and narrow, size-dependent fluorescence spectra, which makes QDs an advanced alternative to organic dyes. Encoding of polyelectrolyte microcapsules with QDs results in highly fluorescent microparticles with a narrow size distribution. Here, we describe an approach to design, preparation, and characterisation of hollow polyelectrolyte microcapsules encoded with stable ultrabright water-soluble CdSe/ZnS QDs modified with thiol-PEG-acid derivative. Laser Doppler micro-electrophoresis and optical, fluorescent, and confocal microscopies have shown that the QD-encoded microcapsules developed have size distribution, surface ζ-potential and fluorescence properties well adapted for live cell imaging. The obtained data pave the way for use of developed system as a versatile platform for imaging and theranostic purposes.

Keywords: polyelectrolyte microcapsules, quantum dots, microencapsulation, theranostics, live cell imaging.

Proceedings of the Nanotech France 2018 International Conference (Nanotech France 2018)
Paris, France, June 27 - 29, 2018
DOI: https://doi.org/10.26799/cp-nanotechfrance2018

1. Introduction

Development of bioimaging and theranostic agents is a challenging task in the field of drug delivery system design. Microparticles (especially polyelectrolyte microcapsules) are well adapted for this purpose because they can carry drugs (including proteins, nucleic acids, and antitumor drugs), magnetic, silver, or gold nanoparticles, fluorescent labels and specific diagnostic nanoprobes both in the microcapsule interior and in its shell (Fig. 1). Microcapsules are known to be used as stimulus-responsive delivery vehicles that may be controlled or opened by magnetic field, ultrasound, or photoexcitation due to the reaction of embedded metal, magnetic or fluorescent nanoparticles on the external stimuli [1]. Therefore, such systems provide an opportunity to develop a versatile platform for controlled drug delivery, imaging, and diagnosis.

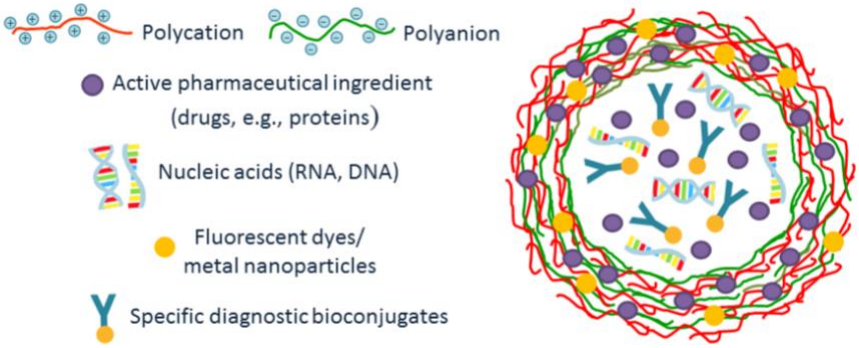

Fig. 1: Schematic diagram of a bioimaging and theranostic tool based on polyelectrolyte microcapsules.

Fluorescent microcapsules have been also shown to be promising candidates for bioimaging. The traditional approaches to obtaining fluorescently labelled polyelectrolyte microcapsules are based on the use of polymers mixed or conjugated with fluorescent dyes for polyelectrolyte matrix formation or entrapment of proteins labelled with the dyes into the microcapsule interior [2, 3]. Excitonic nanoparticles "quantum dots" (QDs), are an excellent alternative to organic dyes typically used for optical encoding [4-6]. QDs are fluorescent semiconductor nanocrystals 2–10 nm in diameter, which are characterised by a wide absorption spectrum and a narrow, symmetrical fluorescence spectrum with position depending on nanoparticle diameter [7, 8]. This allows QDs with different fluorescence maxima to be excited from a single radiation source, offering the possibility of their use as fluorophores for multiplexed optical encoding. QDs are highly photostable and bright, having the quantum yield close to 100% [9].

In this study, we describe all steps of the preparation of QD-encoded polyelectrolyte microcapsules and characterise their physicochemical and functional properties. We demonstrate the successful application of the developed microcapsules to live cell imaging and monitoring of living cells transport. The obtained data may pave the way to the creation of versatile platform for development of the novel bioimaging and theranostic tools based on the fluorescent microcapsules encoded with water-soluble QDs.

2. Experimental

Calcium carbonate microparticles were obtained as described elsewhere [10]. Equal aliquots of 0.33 M $CaCl_2$ and 0.33 M Na_2CO_3 were mixed at room temperature using a magnetic stirrer. The resultant pellet of calcium carbonate microparticles was washed with MilliQ water by resuspending and centrifuging repeated four times. Then the pellet was dried in an oven at 60°C.

The microparticles were encoded with QDs using a modified technique of layer-by-layer deposition of oppositely charged polymers and carboxylated water-soluble QDs at the surface of prepared calcium carbonate microparticles, which served as a matrix. The polyelectrolyte layers consisted of pairs of polymers: the polycation poly(allylamine hydrochloride), PAH, MW ≈ 15 kDa, and the polyanion poly(sodium 4-styrenesulfonate), PSS, MW ≈ 70 kDa. CdSe/ZnS core/shell QDs with a fluorescence maximum λ_{max} equal to 590 nm, covered with 12-unit PEG derivative containing thiol and carboxyl end groups, were used for optical encoding. QD solubilisation procedure was performed as described elsewhere [11].

Calcium carbonate microparticles were suspended in ultrapure water by sonication in an ultrasonic bath, after which, the polyelectrolyte solutions in 0.5 M sodium chloride were added. The obtained suspension was sonicated and incubated while shaking. The excess of polymer was removed by washings and resuspendings in ultrapure water. Negatively charged water-soluble QDs were adsorbed at the polycation-covered microparticle surface and further covered with additional alternately charged polyelectrolyte layers [4, 11]. The microcapsules were subsequently

DOI: https://doi.org/10.26799/cp-nanotechfrance2018

obtained by removing the calcium carbonate core from the prepared encoded microparticles using 0.2 M disodium ethylenediaminetetraacetate (EDTA), pH 6.5. The resultant encoded microcapsules were washed of excess EDTA and stored at 4°C in the dark. Coating of the encoded microcapsules with bovine serum albumin (BSA) was performed by dispersion of the microparticles containing the final layer of polyanion polyacrylic acid (PAA, MW ≈15.0 kDa) in a 50 mM phosphate buffer solution (pH 7.4) containing 1% of BSA.

The surface charges of the solubilised QDs and microparticles as well as the hydrodynamic diameters of the solubilised QDs were determined with the Zetasizer NanoZS device (Malvern, UK). The morphology of calcium carbonate microparticles was analysed by scanning electron microphotography (SEM). Size distribution and fluorescent properties of the microparticles were analysed by optical and fluorescent microscopy. Fluorescent lifetime of the QD-encoded microcapsules was measured at the wavelength of the QDs fluorescence maximum using the second harmonic of an YAG:Nd3+ laser as an excitation source. *In vitro* uptake of polyelectrolyte microcapsules encoded with QDs by live cells was studied using murine alveolar macrophages as a cell model and confocal microscopy as the imaging technique.

3. Results and Discussion

The synthesised calcium carbonate microparticles were characterised by a mean size ranging from 4.0 to 6.0 μm, a slightly negative surface charge (ζ-potential = - 6.0 ± 1.6 mV), and porous, rough surface (Fig. 2),which allowed them to be used as a matrix for the deposition of oppositely charged polyelectrolytes and QDs. The PAH polycation and PSS polyanion containing amine and sulphate groups, respectively, ensured electrostatic interaction between the polymer layers, which resulted in the formation of interpolymer complexes (Fig. 3). The prepared water-soluble QDs had a wide absorption spectrum and a narrow fluorescence spectrum with an emission maximum at 590 nm. The hydrodynamic diameter of the solubilised QD samples varied from 24.0 to 28.2 nm, and their ζ-potential was − 21.9 ± 0.4 mV. This ensured effective adsorption of QDs on the polycation-coated surface of the calcium carbonate microparticles. The prepared encoded microparticles consisted of 12 polymer layers containing a layer of solubilised QDs between the 5th and 7th PAH layers.

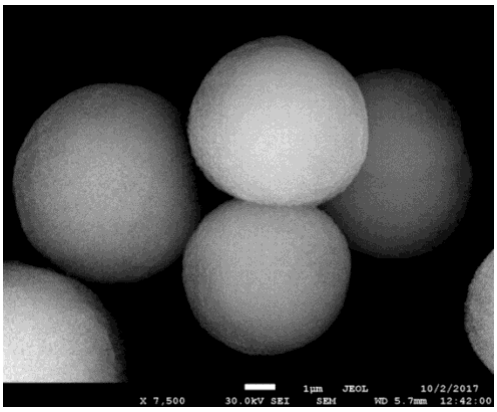

Fig.2: Microphotograph of the synthesised calcium carbonate microparticles obtained by scanning electron microphotography.

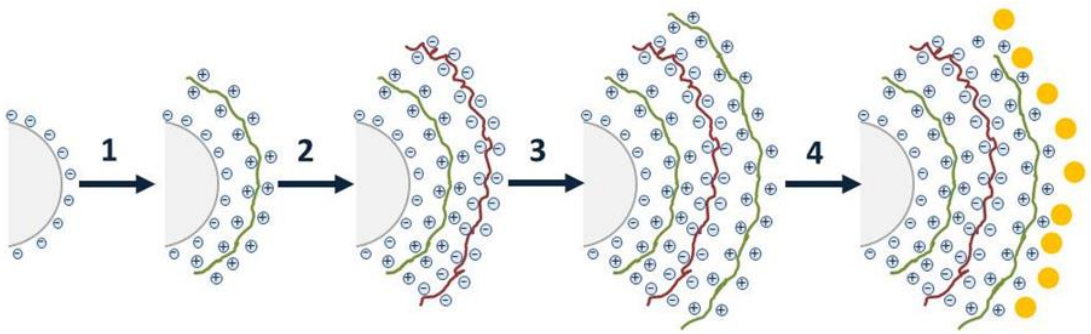

Fig.3: The procedure of the encoding of calcium carbonate microparticles.

The formation of layers upon addition of the polycation (1, 3), polyanion (2), and solubilised QDs (4) are shown.

Proceedings of the Nanotech France 2018 International Conference (Nanotech France 2018)
Paris, France, June 27 - 29, 2018
DOI: https://doi.org/10.26799/cp-nanotechfrance2018

The QD-encoded microparticles and polyelectrolyte microcapsules had a spherical or nearly spherical shape and a size from 3.8 to 6.5 µm (Fig. 4A). Analysis of the morphology and structure of the microparticles and microcapsules in the fluorescent mode showed cavities within the polyelectrolyte microcapsules, as evident by their transparency (Fig. 4B). This demonstrated that the procedure of microparticles core dissolution with EDTA was efficient. Fluorescence lifetime of the QD-encoded microcapsules was 5.99 ns and was characterised by monoexponential dependence of fluorescent intensity on time. Hence, the resultant QD-encoded microcapsules were found to be stable fluorescent microparticles what demonstrates encoding efficiency of the suggested technique of QDs embedding within the polymer shell.

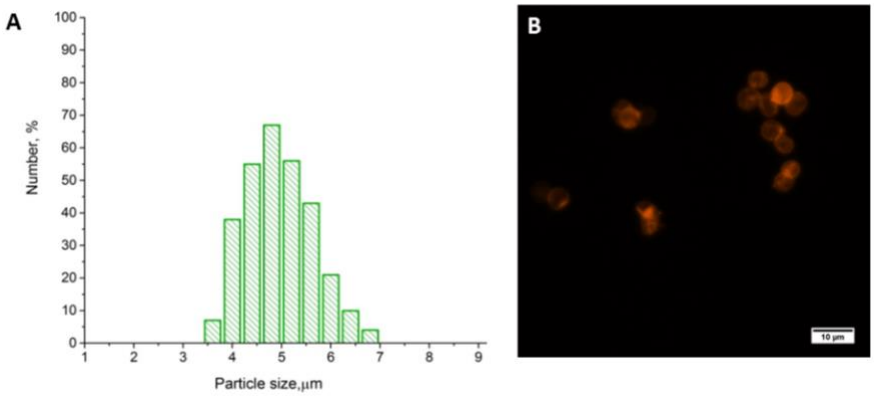

Fig. 4: The size distribution (A) and a fluorescent microscopy image (B) of the QD-encoded microcapsules.

Murine alveolar macrophages were used as a model of phagocytising cells. The signs of the primary uptake of the microcapsules were observed after 4 and 24 h of incubation using confocal microscopy. After 4 h of incubation, single microcapsules underwent uptake prior to conglomerates. Incubation of the microcapsules and the macrophages during 24 h led to the uptake of the conglomerates. The amount of the conglomerates of the polyelectrolyte microcapsules undergoing uptake and located inside the cells or at least attached to the cell surface was larger than after the short-term incubation (Fig. 5). Thus, the polyelectrolyte microcapsules obtained in this study are promising tools for imaging and tracking live cells.

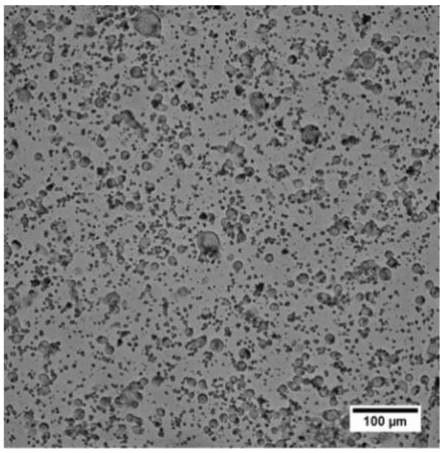

Fig. 5: Phase contrast confocal images of the murine macrophages upon addition of the QD-encoded polyelectrolyte microcapsules coated with BSA.

4. Conclusion

We have shown that the developed QD solubilisation technique provides the transfer of the QDs into the aqueous phase and preparation of sufficiently homogeneous and stable colloidal nanocrystal samples. Encapsulation of water-soluble QDs into the polymer membrane of the microcapsules results in their efficient encoding and formation of highly fluorescent and stable microparticles with a narrow size distribution. Efficient uptake of the prepared QD-encoded microcapsules by murine macrophages has been demonstrated. Hence, the system developed can be used for live cell imaging as well as for intracellular visualization of microcapsule transport and delivery. The obtained results pave the

way to novel applications of QD-encoded microcapsules as delivery and diagnostic platforms that can be used for tracking, imaging and remote control of these processes.

Acknowledgements

This study was supported by the Russian Ministry of Education and Science, State Contract no. 16.1034.2017/ПЧ.

References

1. J. L. Santos, A. Nouri, T. Fernandes, J. Rodrigues, and H. Tomás, "Gene delivery using biodegradable polyelectrolyte microcapsules prepared through the layer-by-layer technique," *Biotechnol. Prog.*, vol. 28, no. 4, pp. 1088–1094, 2012.
2. Q. Zhao and B. Li, "pH-controlled drug loading and release from biodegradable microcapsules," *Nanomedicine: NBM*, vol. 4, no. 4, pp. 302–310, 2008.
3. S. H. Hu, C. H. Tsai, C. F. Liao, D. M. Liu, and S. Y. Chen, "Controlled rupture of magnetic polyelectrolyte microcapsules for drug delivery," *Langmuir*, vol. 24, no. 20, pp. 11811–11818, 2008.
4. K. Brazhnik, Z. Sokolova, M. Baryshnikova, R. Bilan, A. Efimov, A., I. Nabiev, and A. Sukhanova, "Quantum dot-based lab-on-a-bead system for multiplexed detection of free and total prostate-specific antigens in clinical human serum samples," *Nanomedicine: NBM*, vol. 11, no. 5, pp. 1065–1075, 2015.
5. A. Sukhanova, J. Devy, L. Venteo, H. Kaplan, M. Artemyev, V. Oleinikov, D. Klinov, M. Pluot, M., J.H.M. Cohen, and I. Nabiev, "Biocompatible fluorescent nanocrystals for immunolabeling of membrane proteins and cells," *Anal. Biochem.*, vol. 324, pp. 60-67, 2004.
6. A. Sukhanova, L. Venteo, J. Devy, M. Artemyev, V. Oleinikov, M. Pluot, and I. Nabiev, "Highly stable fluorescent nanocrystals as a novel class of labels for immunohistochemical analysis of paraffin-embedded tissue sections," *Lab. Invest.*, vol. 82, pp. 1259-1262, 2002.
7. P. Samokhvalov, M. Artemyev, and I. Nabiev, "Basic principles and current trends in colloidal synthesis of highly luminescent semiconductor nanocrystals," *Chemistry - Eur. J.*, vol. 19, no. 5, pp. 1534-1546, 2013.
8. R. Bilan, F. Fleury, I. Nabiev, and A. Sukhanova, "Quantum dot surface chemistry and functionalization for cell targeting and imaging," *Bioconj. Chem.*, vol. 26, no. 4, pp. 609–624, 2015.
9. R. Bilan, A. Ametzazurra, K. Brazhnik, S. Escorza, D. Fernández, M. Uríbarri, I. Nabiev, and A. Sukhanova, "Quantum-dot-based suspension microarray for multiplex detection of lung cancer markers: preclinical validation and comparison with the Luminex xMAP® system," *Sci. Rep.*, vol. 7, p. 44668, 2017.
10. B. Parakhonskiy, M. V Zyuzin, A. Yashchenok, S. C. Romero, J. Rejman, H. Möhwald, W. J. Parak, and A. G. Skirtach, "The influence of the size and aspect ratio of anisotropic, porous $CaCO_3$ particles on their uptake by cells," *J. Nanobiotechnol.*, vol. 13, no. 53, pp. 1–13, 2015.
11. G. Nifontova, M. Zvaigzne, M. Baryshnikova, E. Korostylev, F. Ramos-Gomes, F. Alves, I. Nabiev, and A. Sukhanova, "Next-generation theranostic agents based on polyelectrolyte microcapsules encoded with semiconductor nanocrystals: Development and functional characterization," *Nanoscale Res. Lett.*, vol. 13, no. 1:30, pp. 1-12, 2018.

Proceedings of the Nanotech France 2018 International Conference (Nanotech France 2018)
Paris, France, June 27 - 29, 2018
DOI: https://doi.org/10.26799/cp-nanotechfrance2018

A biophysical approach to formulation development: drug-plasma protein interaction

Eduarda Fernandes[1§], Telma Soares[2§], M.E.C.D. Real Oliveira[3], Carla M. Lopes[4], Marlene Lúcio[5]
[1] CF-UM-UP - Centro de Física das Universidades do Minho e do Porto
Campus de Gualtar, Braga, Portugal, eduardabfer@gmail.com
[2] CF-UM-UP - Centro de Física das Universidades do Minho e do Porto
Campus de Gualtar, Braga, Portugal, telmabsoares@gmail.com
[3] CF-UM-UP - Centro de Física das Universidades do Minho e do Porto
Campus de Gualtar, Braga, Portugal, beta@fisica.uminho.pt
[4] FP-ENAS/CEBIMED - Fernando Pessoa Energy, Environment and Health Research Unit/Biomedical Research Centre, Faculty of Health Sciences, Fernando Pessoa University
Porto, Portugal, cmlopes@ufp.edu.pt
[5] CF-UM-UP - Centro de Física das Universidades do Minho e do Porto
Campus de Gualtar, Braga, Portugal, mlucio@fisica.uminho.pt

§The authors have equally contributed to this work

Abstract
In this work, the binding constant of ACV to human serum albumin was determined by binding isotherms. Nonlinear least-squares best fit to intrinsic fluorescence quenching effect of the drug was used to determine the association constants between drug and the serum protein at one affinity binding site (K_b=1.79x$10^3$$M^{-1}$). A red shift of the fluorescent spectra confirms association. Thermodynamic parameters for the binding indicated that electrostatic interactions are predominantly involved in the binding of this drug to human serum albumin. This was further confirmed by electrophoretic and dynamic light scattering, where a progressive charge neutralization of the protein was followed by an increase of the size of albumin-drug complex.

Keywords: Human serum albumin; Fluorescence quenching; Dynamic and electrophoretic light scattering; Acyclovir.

1. Introduction

Plasma protein binding properties are determinant in the pharmacokinetic profile of drugs and ultimately in the therapeutic effect achieved. Therefore, for guiding formulation development it is important to proceed with biophysical screening tests to evaluate important parameters such as plasma protein binding constants, as well as to assess the nature of such binding which may give important clues to refine drug formulation at early development stages [1].
For most of routes of administration, the bloodstream is responsible for the drug distribution by the different target and/or off-target tissues. The blood plasma constitutes around 55% of all human blood, and about 7% of plasma is composed by plasma proteins. Human Serum Albumin (HSA) is the most abundant protein in the plasma possessing numerous physiological functions among which is the role as drug carrier [2-4]. Each HSA molecule presents at least 6 binding sites, 2 of which are mainly occupied by drugs [2, 5, 6].
The association between drugs and HSA can be stablished by several types of interactions including hydrophobic, van der Waals and hydrogen bonding or electrostatic interactions. In the event of formation of HSA-drug complexes, these do not have the ability to permeate cell membranes, being confined to the bloodstream, thereby limiting the drug distribution to the target tissues and affecting the desired pharmacological effect [3, 7, 8].
Acyclovir (ACV) is a drug with antiviral activity against HSV that presents a selective toxicity for the virus [9]. In spite of the therapeutic potential, ACV presents some pharmacokinetic parameters that have been the focus of numerous studies and optimizations either by the development of drug derivatives or nanocarriers to obtain antiviral formulations able to pass through several physiological barriers and to be distributed at therapeutic targets [9]. One of these pharmacokinetic parameters include the broad body distribution [10] that might be related with the low affinity of ACV for the plasma carrier protein – HSA.

DOI: https://doi.org/10.26799/cp-nanotechfrance2018

This study aims to provide a biophysical approach to study the extension of drug-HSA association by determination of the binding constant and the evaluation of the types of interaction established. For this purpose, we present ACV-HSA binding study as an example that can be followed for studying other drugs or nanoformulations. Taking advantage of HSA intrinsic fluorescence [11-12] it was possible to study ACV affinity for the carrier protein using fluorescence spectroscopy. Moreover, the complexation of ACV with HSA results in a binding complex with size and superficial charge properties different from the initial macromolecule and ligand. Thus, considering the hydrodynamic size described for HSA (≈ 6-8 nm [13]) and the negative charge of the protein at physiological pH [14] it was possible to use light scattering techniques to describe the ACV-HSA binding complex.

2. Material and Methods

2.1. Materials

Acyclovir was kindly provided by Labesfal Genéricos (Lisbon, Portugal) and Human Serum Albumin (purity ≥ 98.0%) was purchased to Sigma-Aldrich Química, S.L. (Sintra, Portugal). The buffer trizma base (pH 7.4) and HSA solution were prepared with ultrapure Milli-Q water. All chemical reagents and solvents were of analytic grade or above and used without further purification.

2.2. Fluorescence Studies

ACV binding affinity to HSA (K_b) was determined by quenching of intrinsic fluorescence of protein residues according to a previously described procedure [12]. Briefly, samples containing HSA concentration near its concentration in blood plasma - 3.5-5 $g.dL^{-1}$ [15] and increasing ACV concentrations (0 to 4.0 $x10^{-4}$ M) were prepared and incubated in the dark at physiological temperature and pH (37 ^{o}C, pH 7.4) for 30 minutes. Then, the fluorescence steady-state measurements were performed in a Perkin Elmer LS 50 spectrofluorimeter. The excitation fluorescence spectra were obtained in the 200-300 nm range with an emission wavelength of 342 nm and the emission fluorescence spectra were obtained in the 300-500 nm range with an excitation wavelength of 277 nm. To evaluate the type of binding in ACV-HSA interactions, fluorescence quenching determinations were also carried out at three other temperatures (25 ^{o}C, 30 ^{o}C and 45^{o}C) and thermodynamic parameters (ΔG, ΔH and ΔS) were calculated by applying van't Hoff linear fitting to plots of K_b (M^{-1}) as a function of 1/temperature (K^{-1}).

2.3. Dynamic and Electrophoretic Light Scattering studies

In order to confirm ACV binding to HSA, the size and Zeta-potential of HSA and ACV-HSA complexes were measured by Dynamic Light Scattering (DLS) and Electrophoretic Light Scattering (ELS) respectively. Samples containing HSA and increasing concentrations of ACV were prepared and incubated at the same conditions described above. DLS and ELS measurements were performed in a Zetasizer Nano ZS. For DLS measurements disposable polystyrene cells were used and the size values were obtained for intensity distributions with a stabilization time of 100 seconds. Zeta-potential was evaluated using cells containing a dip cell (ZEN1002) provided with electrodes. Results obtained are presented as the average ± standard deviation of at least three independent measurements.

3. Results and Discussion

3.1. ACV acts as a quencher of HSA intrinsic fluorescence

Figure 1 (A) presents the excitation and emission spectra of HSA in the presence of increasing concentrations of ACV where it is possible to observe a decrease in fluorescence intensity upon drug binding and a bathochromic shift of the emission. The decrease in fluorescence intensity is due to collisional quenching of tryptophan (responsible for HSA intrinsic fluorescence) upon drug binding. The shift can be explained by the fact of tryptophan being affected by surrounding environment. In the current case, ACV can induce a spectral shift upon establishing association with indole group of tryptophan [16].

DOI: https://doi.org/10.26799/cp-nanotechfrance2018

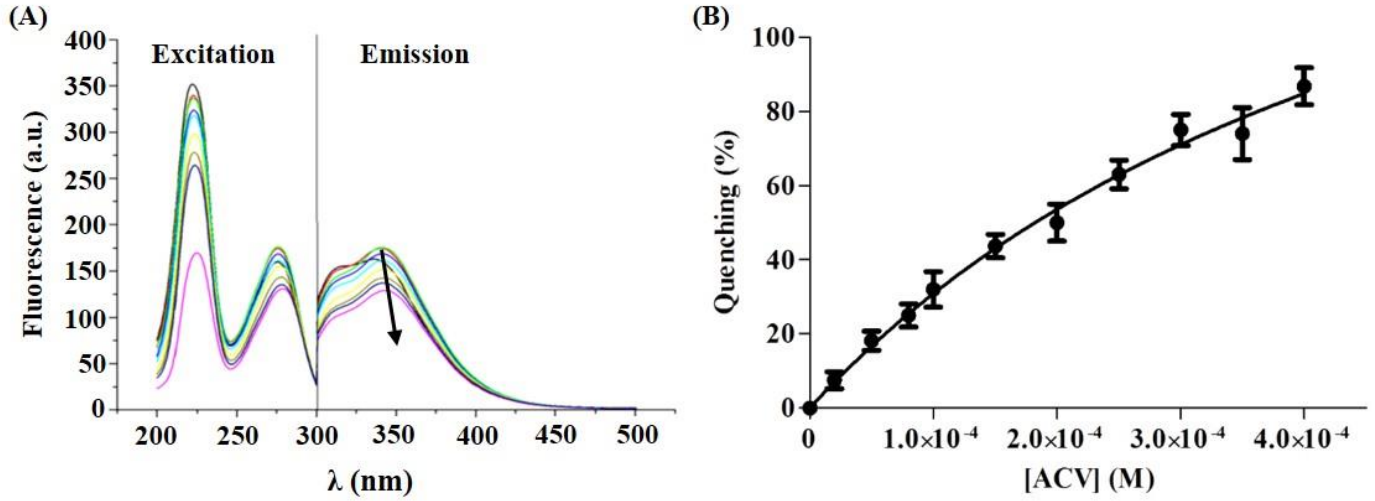

Fig. 1: (A) Excitation and emission spectra of HSA in the absence and presence of increasing concentrations of ACV [0-4.0x10^{-4} M) at 37 ^{o}C and physiological pH (7.4). Arrow indicates quenching effect and bathochromic shift. (B) Isotherm binding plot of fluorescence quenching (%) as a function of ACV concentration with a nonlinear least-squares best fit applied to the experimental data represented according to equation (1).

Figure 1 (B) presents the binding isotherm of ACV-HSA. The nonlinear fit to the experimental data was obtained using equation (1) from which it was possible to calculate K_d = 558 µM and n=1 indicating that the drug binds to HSA binds in one single site, probably binding site II, where the fluorescent tryptophan residue is located [14].

$$Quenching\ (\%) = \frac{y_{máx} n}{1 + \frac{K_d}{[ACV]}} \quad (1)$$

It is important to highlight that K_d value, being higher than 100 µM is indicative of a low affinity of ACV for the plasma protein studied, as confirmed by the determination of a low K_b value of 1.79x10^{3}M^{-1} (K_b=1/K_d). As referred before, HSA is responsible for the transport through the body of exogenous compounds. The low affinity of ACV for the carrier protein limits the drug transport to the therapeutic target, which may justify its broad body distribution. The thermodynamic parameters dependent of temperature were also calculated according to van't Hoff equation in order to elucidate interaction forces between HSA and ACV:

$$ln\ (K_b) = -\frac{\Delta H}{RT} + \frac{\Delta S}{R} \quad (2)$$

According to this an enthalpic variation of -1.72 KJ/mol and an entropic variation of 9.24 J/mol were obtained and a negative ΔG. Ross and Subramanian have characterized the sign and magnitude of the thermodynamic parameter associated with various individual kinds of interaction that may take place in protein association process, and accordingly it can be concluded that ACV and HSA binding are spontaneous and driven by electrostatic interactions [17]. The current results are in agreement with other studies that also concluded weak binding for ACV and albumin by electrostatic interactions, calculated by other methodologies (stern-volmer fitting plots and molecular simulations) [14, 18]. In this regard, it should be highlighted that previous works have used different concentrations of HSA that are not comparable to the typical concentrations found in serum [15]. Indeed the used HSA concentrations are clearly inferior to the physiological values. Aiming to get as closer as possible to the physiological conditions we have used HSA concentration

DOI: https://doi.org/10.26799/cp-nanotechfrance2018

within the reference limit of serum. Furthermore we have followed HSA-ACV binding by two complimentary techniques DLS and ELS.

In Figure 2 are plotted the zeta potential values obtained as function of ACV concentrations. In the absence of ACV, HSA shows a negative superficial charge closest to the value described in the literature for the protein (-15 mV) [19, 20]. The addition of ACV results in an increase of zeta potential towards less negative values (Figure 2 (A)). In fact, ACV has ionisable groups and a positive induced dipole at the amine residue with a cationic charge may neutralize the negatively charged residues of albumin. Thus, the initial increasing of the superficial charge can be directly associated with the amount of drug that binds to HSA (green coloured region of Figure 2 (A)) and the zeta-potential stabilization indicates the saturation of the binding sites (blue coloured region of Figure 2 (A)). The same conclusion can be achieved by evaluation of the size, where initially only albumin size is detected (pink coloured region of Figure 2 (B) and by charge neutralization upon drug binding, larger drug-HSA complexes are formed (green coloured region of Figure 2 (B)) until a stabilization point is reached and size does not increase anymore (blue coloured region of Figure 2 (B)).

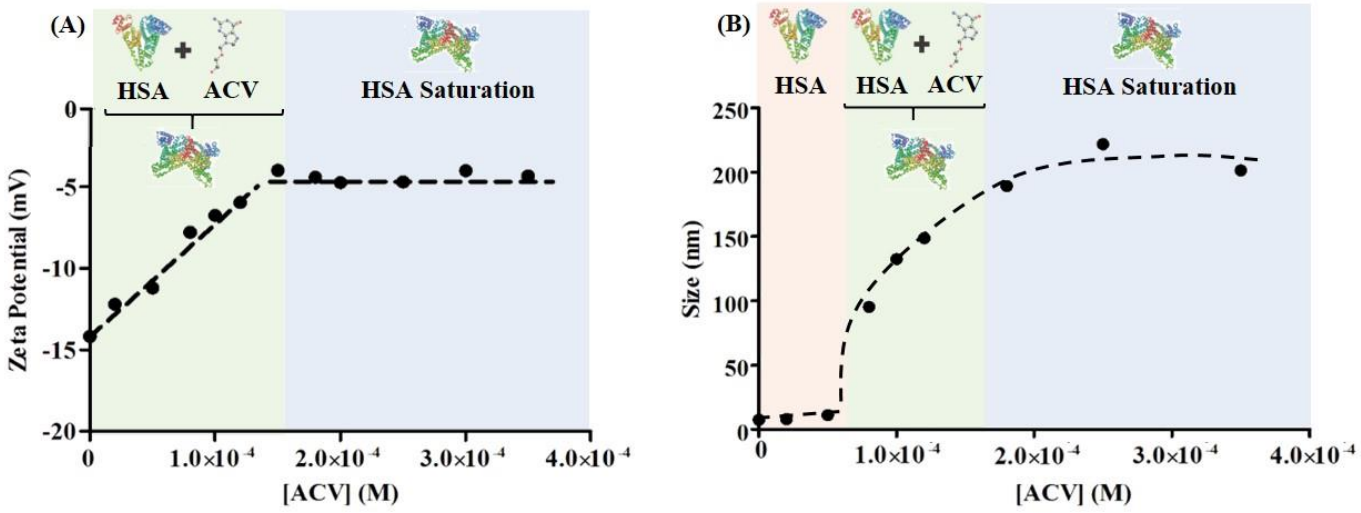

Fig. 2: Graphical representation of zeta-potential (A) and size (B) of HSA in the absence and presence of increasing concentrations of ACV. The different coloured areas represent the different phases of ACV-HSA binding. Dashed lines are guidelines to the eye.

4. Conclusion

Binding isotherms based on intrinsic fluorescence quenching at several temperatures combined with DLS/ELS constitute interesting screening techniques for an *in vitro* prediction of drug association with serum albumin, allowing researches to get insights about drugs and formulation pharmacokinetic behaviour.
ACV pharmacokinetic issues have been extensively described in the literature. The broad distribution can limit the ACV pharmacological action. The plasma protein binding was analysed by ACV interaction with HSA and demonstrates that the drug presents a low affinity for this plasma protein ruled by electrostatic interactions consequently associated with this broad distribution through the body

Acknowledgements

This work was supported by the Portuguese Foundation for Science and Technology (FCT) in the framework of the Strategic
Funding UID/FIS/04650/2013. ML acknowledges the exploratory project funded by FCT with the reference IF/00498/2012. EF acknowledges the scholarship CFUM-BI-10/2018 - UID/FIS/04650/2013.

References

[1] E.B. Fernandes, T. B. Soares, H. Gonçalves and M. Lúcio, "Spetroscopic studies as a toolbox for biophysical and chemical characterization of lipid-based nanotherapeutics", *Front. Chem.* , vol. 6, 2018

[2] L. Kerns, Edward H.; Di, *Drug-like Properties: Concepts, Structure Design and Methods - from ADME to Toxicity Optimization*. Oxford, UK: ElsevierInc., 2008.

[3] G. Lambrinidis, T. Vallianatou, and A. Tsantili-Kakoulidou, "In vitro, in silico and integrated strategies for the estimation of plasma protein binding. A review," *Adv. Drug Deliv. Rev.*, vol. 86, pp. 27–45, 2015.

[4] J. Ghuman, P. A. Zunszain, I. Petitpas, A. A. Bhattacharya, M. Otagiri, and S. Curry, "Structural basis of the drug-binding specificity of human serum albumin," *J. Mol. Biol.*, vol. 353, no. 1, pp. 38–52, 2005.

[5] X. M. He and D. C. Carter, "Atomic structure and chemistry of human serum albumin," *Nature*, vol. 358, no. 6383, pp. 209–215, 1992.

[6] S. S. Singh, "Preclinical Pharmacokinetics: An Approach Towards Safer and Efficacious Drugs," *Curr. Drug Metab.*, vol. 7, pp. 165–182, 2006.

[7] H. Wan and A. G. Holmen, "High throughput screening of physicochemical properties and in vitro ADME profiling in drug discovery," *Comb. Chem. High Throughput Screen.*, vol. 12, no. 3, pp. 315–329, 2009.

[8] J. Lin, C. Diana, S. M. F. De Morais, J. J. Xu, R. J. Polzer, and S. M. Winter, "The Role of Absorption, Distribution, Metabolism, Excretion and Toxicity in Drug Discovery," *Curr. Top. Med. Chem.*, vol. 3, no. 10, pp. 1125–1154, 2003.

[9] C. M. Lopes, J. Silva, M.E.C.D. Real Oliveira, M. Lúcio, "Lipid-based colloidal carriers for topical application of antiviral drugs" in *Design of Nanostructures for Versatile Therapeutic Applications*, Alexandru Mihai Grumezescu (ed), 2018, Elsevier Inc., Oxford, Chapter 14, p.565-622.

[10] O. L. Laskin, "Clinical Pharmacokinetics of Acyclovir," *Clin. Pharmacokinet.*, vol. 8, no. 3, pp. 187–201, 1983.

[11] K. M. Naik, D. B. Kolli, and S. T. Nandibewoor, "Elucidation of binding mechanism of hydroxyurea on serum albumins by different spectroscopic studies," *Springerplus*, vol. 3, no. January 2015, pp. 360–372, 2014.

[12] A. M. O. Azevedo, D. M. G. Ribeiro, P. C. A. G. Pinto, M. Lúcio, S. Reis, and M. L. M. F. S. Saraiva, "Imidazolium ionic liquids as solvents of pharmaceuticals: Influence on HSA binding and partition coefficient of nimesulide", *Int. J. Pharm*., vol. 433, no. 1-2, pp. 273-278,2013

[13] B. Jachimska, M. Wasilewska, and Z. Adamczyk, "Characterization of globular protein solutions by dynamic light scattering, electrophoretic mobility, and viscosity measurements.," *Langmuir*, vol. 24, no. 13, pp. 6866–6872, 2008.

[14] T. Liu and R. Guo, "Effects of Triton X-100 and Acyclovir on Human Serum Albumin Structure", *J. Surfactants Deterg.*, vol. 11, no. 1, pp. 33-39, 2008

[15] S. Choi, E. Y. Choi, D. J. Kim, J. H. Kim, T. S. Kim, and S. W. Oh, "A rapid, simple measurement of human albumin in whole blood using a fluorescence immunoassay (I)," *Clin. Chim. Acta*, vol. 339, no. 1–2, pp. 147–156, 2004.

[16] J. R. Lakowicz, *Principles of Fluorescence Spectroscopy*. 3rd edition. New York: Springer, 2006.

[17] P. D. Ross and S. Subramanian, "Thermodynamics of Protein Association Reactions: Forces Contributing to Stability," *Biochemistry*, vol. 20, pp. 3096-3102, 1981.

[18] A. S. Abdelhameed, A. H. Bakheit, F. M. Almutairi, H. AlRabiah, and A. A. Kadi, "Biophysical and in silico studies of the interaction between the anti-viral agents Acyclovir and Peniciclovir and Human Serum Albumin," *Molecules*, vol. 22, no. 11, pp. 1906, 2017.

[19] S. Sekowski, A. Kazmierczak, J. Mazur, M. Przybyszewska, M. Zaborski, D. Shcharbina and T. Gabryelaka, "The interaction between PAMAM G3.5 dendrimer, Cd^{2+}, dendrimer–Cd^{2+} complexes and human serum albumin," *Colloids and Surfaces B: Biointerfaces*, vol. 69, pp. 95-98, 2009.

[20] A. Hosainzadeh, M. Gharanfoli, M. R. Saberi and J. Chamani, "Probing the interaction of Human Serum Albumin

with bilirubin in the presence of Aspirin by multispectroscopic, molecular modeling and zeta potential techniques: insight on binary and ternary systems," *Journal of Biomolecular Structure and Dynamics*, vol. 29, no. 5, pp. 1013-1050, 2012.

Proceedings of the Nanotech France 2018 International Conference (Nanotech France 2018)
Paris, France, June 27 - 29, 2018
DOI: https://doi.org/10.26799/cp-nanotechfrance2018

Porous PDMS / CNF Nanocomposites for Sensing Applications

Wenyuan Luo, Mohammad Charara, Mrinal C. Saha, Yingtao Liu

School of Aerospace and Mechanical Engineering, University of Oklahoma
865 Asp Ave., Norman, Oklahoma, USA, msaha@ou.edu

Abstract
This paper reports the fabrication of highly flexible and electrically conducting porous PDMS/CNF nanocomposites using sugar particles as templates. CNF are transferred into the pores of the porous PDMS via the direct fabrication method. In this method, the sugar particles are first coated with CNF, ensuring good adhesion between the CNF and polymer during the fabrication process. Solvents with different CNF concentration are used to investigate the effectiveness of the CNF concentrations on the sensing properties. A high resolution scanning electron microscope is used to investigate the CNF distribution. Sensing response is measured via electrical resistivity using the two-probe method. The sensing capability of the porous PDMS/CNF nanocomposite is characterized under compressive cyclic load and their corresponding piezoresistive functions are evaluated.

Keywords: PDMS foam, carbon nanofiber, mechanical properties, compression behaviour, electrical conductivity.

1. Introduction

Highly stretchable and electrically conductive materials are of critical need in the emerging field of wearable electronics, prosthetics, robotic manipulation, and wearable health monitoring [1-3]. Polydimethylsiloxane (PDMS) elastomers are highly stretchable and have mechanical and deformation properties which can be tailored. Recent research has shown that porous PDMS can further improve its flexibility compare to its solid (i.e., nonporous) counterparts [4-6]. Piezoresistive sensing applications require that the porous PDMS be electrically conductive so that the change in resistance is proportional to the deformation. Carbon based nanomaterials such as carbon nanotubes, carbon nanofibers (CNFs), and graphene have previously been used as conducting fillers [7-12]. However, effective incorporation of carbon nanomaterials, such as CNFs, in porous PDMS nanocomposite remains a challenge in the development of highly flexible sensing materials and devices.

This paper reports a simple method to fabricate highly deformable and electrically conductive porous CNF/PDMS nanocomposites using the sugar template technique. Sugar particles were first coated with CNFs and used for the fabrication of sugar templates. Then, porous CNF/PDMS nanocomposites were manufactured by submerging the prepared sugar templates in PDMS pre-polymer. The porous nanocomposites were characterized to understand their microstructure, morphology, and electrical resistance. Finally, the piezoresistive sensing capabilities of the fabricated nanocomposites were tested under compressive cyclic loads.

2. Experimental

2.1. Materials

CNFs with average diameter 100 nm (Pyograf-III PR-24XT-LHT, Applied Science, Inc.) were used as the electrically conductive nanoparticles. Tetrahydrofuran (THF) was used as the organic solvent during the fabrication. PDMS (Sylgard 184 Dow Corning Co. Ltd.) was used as the base polymer. Pure cane sugar crystals (Florida Crystals, Inc.) were used as the porogen. Sugar crystals were filtered using a strainer to eliminate agglomerates. The average size of the filtered cane cubes was 500 μm.

2.2. Nanocomposite Fabrication

A pre-determined amount of CNFs were introduced into THF solvent solutions and dispersed using a high intensity ultrasonic probe for 6 hours to create the CNF-THF suspensions. The suspensions were stirred to partially evaporate the solvent to reduce the volume of CNF/THF suspensions. Cane sugar particles were added into the CNF/THF suspensions. The remaining solvent was evaporated on a hot plate. Once all THF was removed, sugar particles were coated with the CNFs, and used to manufacture sugar templates using an aluminium mould. Prepared CNF/sugar

DOI: https://doi.org/10.26799/cp-nanotechfrance2018

powders were compressed into the mould, heated at 120° C for 30 minutes in an oven, and cooled back to room temperature before removal from the mould. PDMS pre-polymer was prepared by mixing the pre-polymer base (part A) and a crosslinking curing agent (part B). The prepared sugar templates were submerged into the PDMS pre-polymer for 24 hours, allowing polymer to fully fill the pores in the sugar templates. Excess PDMS on sugar templates was trimmed off along the sugar surface. The manufactured samples were submerged in water to dissolve the sugar crystals, and fully dried. This practice was repeated using CNF/THF solutions with different concentrations to achieve CNF/PDMS samples with different CNF weight loading. Pristine porous PDMS foam was fabricated using a similar method as the CNF/PDMS nanocomposites, with uncoated sugar crystals. These control specimens were used to help identify the weight of PDMS in the CNF/PDMS nanocomposites. Fig. 1 shows the process from CNF coated sugar cube to porous CNF/PDMS nanocomposite sample.

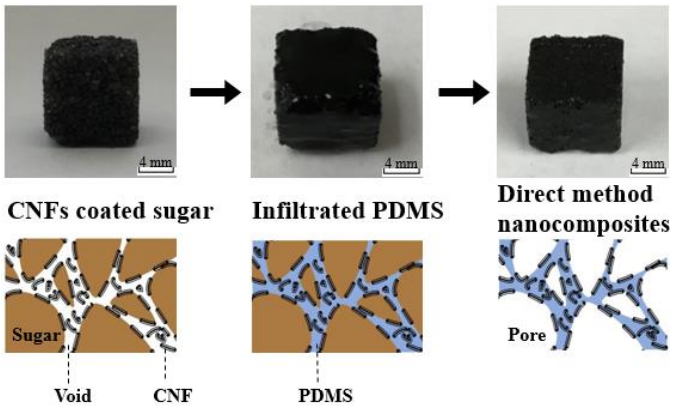

Fig. 1: Process from CNF coated sugar cube to porous CNF/PDMS nanocomposites.

2.3. Characterization of CNF/PDMS nanocomposites

The morphology of the porous CNF/PDMS nanocomposites was examined by a field emission scanning electron microscope (FESEM) at 20 kV. Each examined sample surface was sputter-coated with a thin layer of gold palladium alloy to improve the electrical conductivity. Electrical resistivity of the developed porous nanocomposites is critical for piezoresistive sensing applications. The two-probe method was used to measure the samples' electrical resistivity by inserting two needles into the cubic samples. A multi-meter (Agilent 34401A) connected to a data logger (RS-232) was used to record the electrical resistance data. The electrical resistance data was recorded for 20 seconds in each measurement.

To validate the sensing capability, the porous CNF/PDMS nanocomposites were clamped between two copper plates on an Instron 5900 column testing machine. A 0.1 N initial force was applied to ensure full contact on top and bottom sample surfaces throughout the entire tests. A cyclic compressive load was applied, deforming the sample with maximum strains of 1.25%, 2.5%, 5%, 10%, 20%, and 40% at a crosshead load rate of 1mm/min. The force, deformation, and electrical resistance were recorded continuously by the Instron testing machine and a multi-meter (Agilent 34401A).

3. Results and Discussions

The morphology and CNF distribution in porous nanocomposites was characterized using FESEM. As shown in Fig. 2, the CNFs were well-distributed on the PDMS walls, forming an electrical conductive network.

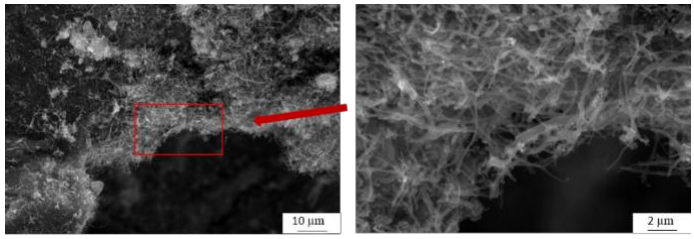

Fig. 2: SEM images showing the CNF distribution in porous nanocomposites.

The electrical property was critical for good piezoresistive sensing function. The electrical conductivity of porous CNF/PDMS was calculated using:

$$\sigma = \frac{L}{AR} \tag{1}$$

where σ is the electrical conductivity, R is the electrical resistance, A is the cross-sectional area of the sample, and L is the height of nanocomposites. The measured electrical conductivity of the manufactured nanocomposites is listed in Table 1.

Table 1. Electrical conductivity of porous CNF/PDMS nanocomposites.

CNF wt.%	Conductivity (S/m)
9	8.12E-03
6	2.56E-03
3	4.49E-04
1	1.36E-06

The sensing function of the porous CNF/PDMS nanocomposites with 3% CNF weight loading was characterized under compressive cyclic loading conditions. The tests were performed at maximum compressive strains of 1.25%, 2.5%, 5%, 10%, 20%, and 40%. Fig. 3 illustrates the relationship between the relative electrical resistance change and maximum strain during five cycles of the tests. As expected, the relative resistance change increased with increase in compressive strain. When the sample was deformed, the average distance between CNFs varied, resulting in the change of piezoresistive sensing due to tunnelling effects in the CNF networks. When the compressive force was unloaded, the CNFs returned to their original location, reversing the tunnelling effect of the electrical networks and increasing the electrical resistance back to the original level.

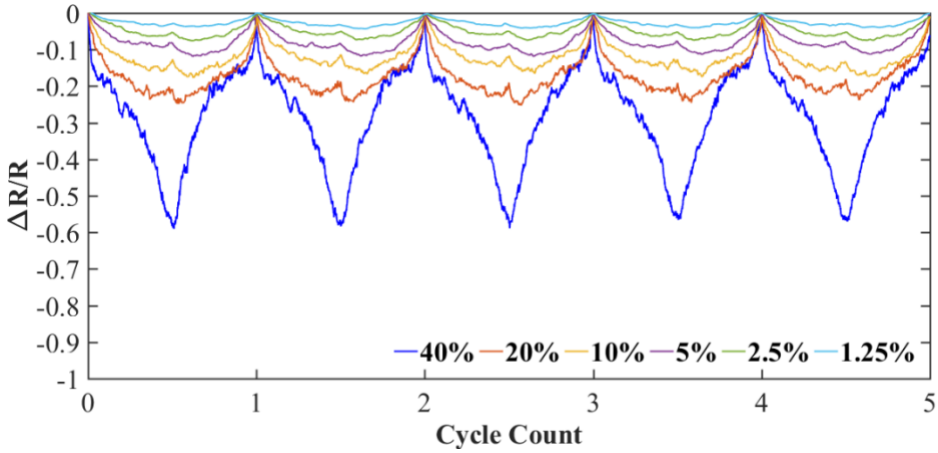

Fig1. 3 Sensing functions of porous CNF/PDMS (direct method) at 3% wt. CNF at different max compressive strains.

A common way of characterizing the sensing capability of a piezoresistive material is its relative resistance change normalized by the applied strain, also known as gauge factor. This is calculated with equation (2):

$$GF = \frac{(R_o - R)/R_o}{\varepsilon} \tag{2}$$

Table 2. Gauge factor of CNF/PDMS (direct method) at 3% wt. CNF at different max compressive strains

Strain	Resistance change	Gauge factor
1.25%	4.1%	3.28
2.5%	7.4%	2.96
5%	11.8%	2.36
10%	16.5%	1.65
20%	25.3%	1.27
40%	58.9%	1.47

DOI: https://doi.org/10.26799/cp-nanotechfrance2018

where R_o is the original resistance, R is the resistance at a point in time, and ε is the applied strain. Table 2 lists the gauge factor for each test at different max strains. A high gauge factor was obtained when the maximum strain was low. However, the gauge factor reduced as the maximum strain increased up to 40%, due to the elastic nature of PDMS.

4. Conclusion

This paper presented a direct approach to manufacturing porous nanocomposite materials using CNF nanoparticles and PDMS elastomer. CNFs were deposited on sugar crystals before used for nanocomposite fabrication. By adjusting the amount of CNFs used during fabrication, the weight concentration of CNFs in the nanocomposites was controlled in the range of 1 wt.% to 9 wt.%. Good CNF distribution was obtained and verified by FESEM images. The electrical conductivity was characterized using the two-probe method. Piezoresistive sensing function of the nanocomposites was tested under compressive cyclic load conditions. A maximum gauge factor of 3.28 was obtained using the developed nanocomposites, showing the good sensitivity of the developed porous nanocomposites.

References

1. C. Lucarotti, C.M. Oddo, N. Vitiello, and M.C. Carrozza, *Synthetic and bio-artificial tactile sensing: A review.* Sensors, 2013. **13**(2): p. 1435-1466.
2. W. Luo, Y. Liu, and M. Saha. *CNT Bucky Paper Enhanced Sandwich Composites for In-Situ Load Sensing*. in *ASME 2017 International Mechanical Engineering Congress and Exposition*. 2017. American Society of Mechanical Engineers.
3. V. Eswaraiah, K. Balasubramaniam, and S. Ramaprabhu, *Functionalized graphene reinforced thermoplastic nanocomposites as strain sensors in structural health monitoring.* Journal of Materials Chemistry, 2011. **21**(34): p. 12626-12628.
4. S. Duan, K. Yang, Z. Wang, M. Chen, L. Zhang, H. Zhang, and C. Li, *Fabrication of highly stretchable conductors based on 3D printed porous poly (dimethylsiloxane) and conductive carbon nanotubes/graphene network.* ACS applied materials & interfaces, 2016. **8**(3): p. 2187-2192.
5. S. Wu, J. Zhang, R.B. Ladani, A.R. Ravindran, A.P. Mouritz, A.J. Kinloch, and C.H. Wang, *Novel electrically conductive porous PDMS/carbon nanofiber composites for deformable strain sensors and conductors.* ACS applied materials & interfaces, 2017. **9**(16): p. 14207-14215.
6. J.-W. Han, B. Kim, J. Li, and M. Meyyappan, *Flexible, compressible, hydrophobic, floatable, and conductive carbon nanotube-polymer sponge.* Applied physics letters, 2013. **102**(5): p. 051903.
7. T. Kashiwagi, E. Grulke, J. Hilding, K. Groth, R. Harris, K. Butler, J. Shields, S. Kharchenko, and J. Douglas, *Thermal and flammability properties of polypropylene/carbon nanotube nanocomposites.* Polymer, 2004. **45**(12): p. 4227-4239.
8. B. Schartel, P. Pötschke, U. Knoll, and M. Abdel-Goad, *Fire behaviour of polyamide 6/multiwall carbon nanotube nanocomposites.* European Polymer Journal, 2005. **41**(5): p. 1061-1070.
9. E.S. Steigerwalt, G.A. Deluga, D.E. Cliffel, and C. Lukehart, *A Pt− Ru/graphitic carbon nanofiber nanocomposite exhibiting high relative performance as a direct-methanol fuel cell anode catalyst.* The Journal of Physical Chemistry B, 2001. **105**(34): p. 8097-8101.
10. X. Chen, S. Wei, A. Yadav, R. Patil, J. Zhu, R. Ximenes, L. Sun, and Z. Guo, *Poly (propylene)/Carbon Nanofiber Nanocomposites: Ex Situ Solvent-Assisted Preparation and Analysis of Electrical and Electronic Properties.* Macromolecular Materials and Engineering, 2011. **296**(5): p. 434-443.
11. G. Williams, B. Seger, and P.V. Kamat, *TiO2-graphene nanocomposites. UV-assisted photocatalytic reduction of graphene oxide.* ACS nano, 2008. **2**(7): p. 1487-1491.
12. Y. Li, L. Tang, and J. Li, *Preparation and electrochemical performance for methanol oxidation of Pt/graphene nanocomposites.* Electrochemistry Communications, 2009. **11**(4): p. 846-849.

Proceedings of the Nanotech France 2018 International Conference (Nanotech France 2018)
Paris, France, June 27 - 29, 2018
DOI: https://doi.org/10.26799/cp-nanotechfrance2018

Fabrication of polyaniline-graphene/polystyrene nanocomposites for flexible gas sensor

Jolly Bhadra, Anton Popelka, Asma Abdulkareem, Noora Al-Thani
Center for Advanced Materials, Qatar University, P.O. Box 2713, Doha, Qatar

Abstract

This research work presents the fabrication of a polyaniline-graphene (PANI-G) nanocomposite-coated polystyrene (PS) nanofiber mat for generating a flexible and highly sensitive gas sensor. Preparation of the PANI-G nanocomposite and its deposition on the surface of the nanofiber mat are performed via in-situ chemical polymerization. The surface morphology of the prepared flexible films is investigated using SEM. Morphology studies reveal that the PANI-G nanocomposite forms a uniform coating on the surface of PS fibres. Chemical properties analysis, carried out by FTIR and XRD, reveals the formation of a chemical interaction between the nanocomposites and the polymer fibre surface. The TGA study showed an increase in the thermal stability of the coated polymer fibres compared to the pure fibres. Addition of nanocomposite increased the electrical conductivity of the coated sample by the ninth order. The nanocomposite-coated PS flexible film is tested for its use in a sensor for carbon dioxide gas (20-100 ppm). Due to the higher surface area, the film shows a high sensitivity towards carbon dioxide gas; as the gas concentration increases the surface resistivity also increased. At the same time, the gas sensor shows good repeatability, low response time, and low recovery time.

Keywords: Nanocomposite, Electrospin nanofiber, insitu chemical polymerization, flexible thinfilm, gas sensor

1. Introduction

Currently a number of flexible conductive film based electronic devices have been widely used in touch screens, electronic skins, environmental sensors, and wearable perspiration analyzer [1]. Among all these electronic devices gas sensor applications has become one of the fastest growing research area due to its significant importance in monitoring air surrounding us [2]. Depending on different sensing techniques and principles lots of polymeric materials [3, 4], semiconductors [5, 6] and organic/inorganic composites [7, 8] have been used as sensing materials. The performance assessment of a chemical gas sensor are done on the basis of parameters like sensitivity, selectivity, time response, stability, durability, reproducibility, and reversibility [9–10]. Among various applications polymer composite based gas sensors are one of the most widely studied gas and vapor sensors because of their unique responses to each analyte gases. Several research groups have observed high response and sensitive polymer-based sensors for detection of volatile organic compounds [11-12].

Among the various conducting polymers, polyaniline (PANI) is an intrinsically gas sensitive polymer. The responsive nature of PANI to environmental pollutants such as NH_3, CO, SO_2 and other greenhouse gases, is highly dependent on the processing techniques employed. Another additional advantages of PANI are environmentally friendly and stable polymer, simple synthesizing method, simple doping-dedoping chemistry and low cost [13, 14]. Alternatively carbon based nanomaterials, such as graphene which is a 2D single layered material [15, 16] with high specific surface area and extraordinary room temperature electron mobility of 20,000 cm^2/Vs, it has a resistivity of 10^{-6} Ω.cm, and its carrier density $10^{12}/cm^2$ electrical, mechanical and chemical properties very useful for gas and vapor sensing [17, 18].

Another important aspect of chemical gas sensor that greatly affects the sensor efficiency is available surface are of the material that are exposed to the analyte gas. A number of chemical and physical methods are already used to produce material with high surface area. However, electrospinning is one of the most convenient and widely

DOI: https://doi.org/10.26799/cp-nanotechfrance2018

used methods to obtain nano or micro fibrous structure mechanically. Keeping these strategies in mind in this research PANI-graphene composites have been successfully prepared and deposited by insitu polymerization on the surface of electrospin polystyrene (PS) fibers investigated by several researchers. The obtained flexible conducting films are used for sensing application.

2. 2. Materials and Experimental Methods

This section describes the specification of the materials and different chemicals used for the experiment, and the description of the methods adopted to prepare the samples and further to characterize the materials after preparation.

2.1. Materials

Aniline, N, N-Dimethylformamide, Polystyrene, Graphite are purchased from Sigma Aldrich Co., Ltd, USA. Hydrochloric Acid, Ammonium peroxodisulphate, Sodium nitrate, Sulphuric acid are purchased VWR CHEMICALS Analwr Normapur. potassium permanganate, Hydrogen peroxide are purchased from BDH Laboratory Supplies Pools, BH15 TD, England. All the chemicals are used without further treatment.

2.2. Experimental methods

This section gives the experimental detail of the sample preparation and methods adopted to undergo material characterization. PS nanofiber membrane is prepared by electrospinning at room temperature. Initially the 20 % PS solution is prepared by dissolving in dimethyl formamide (DMF) under constant stirring. Electrospinning process is performed in a horizontal configuration setup and the working conditions adopted are as follow: 15 cm distance from the needle to the collector, a flux of 1.5 ml/h provided by syringe pump and a 15 KV voltage is applied to the needle to yield nanofibers. The fibers produced are collected on a rotated collector covered with an aluminium foil, and then they are dried at room temperature for 24 h. The surface of PS membrane in an aluminum foil is treated for 30 seconds under dynamic conditions at atmospheric pressure using radio frequency plasma force system manufactured by (Venus 75-HF, PlasmaEtch) in USA. Graphene oxide (GO) has been prepared by a modified Hummers method.

The synthesis of polyaniline (PANI) is performed using chemical polymerization of aniline in an aqueous acidic medium. Aniline monomer is added into acidic solution under constant stirring. Dropwise ammonium persulphate solution is added to aniline solution under stirring. The solution turns green indicating the formation of PANI and the stirring kept standing for overnight in an ice bath maintained at 0-5 °C temperature to obtained polymerized dark-green precipitate. After that, the polymerized solution is then filtered and washed several times with distilled water until the filtrate became acid free. The precipitate are dried in an oven at 40°C for 24 h to obtain conducting form of PANI. The nanocomposite coated samples are prepared by insitu polymerization process. The electrospun mats are weight and plasma treated before coating. Then electrospun fiber mats are dipped inside the reaction medium during polymerization, to obtain nanocomposite coated films. The obtained mats are washed with DI water and dried at room temperature.

2.3.Characterization techniques

Scanning electron microscopy (SEM) is employed to study the surface morphology of electrospin PS nanofibers, and grain size of PANI and Graphene and PANI-Graphene composite using a nano-SEM Nova 450. A Fourier-transform infrared spectrometer (FTIR) (8101 M, Shimadzu) is used for the study of chemical interaction between the polymers. To study the thermal properties of the PANI, thermogravimetric analysis (TGA) is performed using a Perkin Elmer Pyris TGA. The electrical properties are studied by measuring the in-plane I-V characteristics and four-probe conductivity. Finally, a Keithley 2400 source meter is used to measures the gas sensitivity measurements.

Proceedings of the Nanotech France 2018 International Conference (Nanotech France 2018)
Paris, France, June 27 - 29, 2018
DOI: https://doi.org/10.26799/cp-nanotechfrance2018

3. Result and Discussion

3.1. Scanning Electron Microscopy

SEM analysis of all the samples has been performed; the images are shown in Figure 1. In images of neat electrospun PS fibers are uniform microfibers with average diameter of 3µm. SEM images of both PANI and PANI-GO coated PS fiber mats show a uniform conducting coating on surface of PS fibers. However PANI-GO coated mat over covered the mat, that may affect availability of specific area for gas sensor application.

3.2. Fourier Transform Infrared Spectroscopy

The FTIR analysis of all the samples are done inorder to know the chemical properties and interaction among PS, PANI and graphene. Figure 2 shows the FTIR spectra of neat PS, PANI coated PS mat and graphene-PANI coated PS mat. For pure PS a band is observed at 3081.2 cm-1 – 3001.11 cm-1 due to C-H aromatic tension, 2923.91 cm-1 and 2850.40 cm-1 because of CH_2 asymmetric and symmetric tension, 19430.19 –1728.23 cm-1 as a result of aromatic ring mono substitution; 1452.28 cm-1 deformation of the aromatic ring; 1069,65 cm-1 due to flexion C-H in plane. All the signature peaks of PS are seen in IR spectra of PANI coated and graphene-PANI coated PS mates. However, there are difference in intensity.

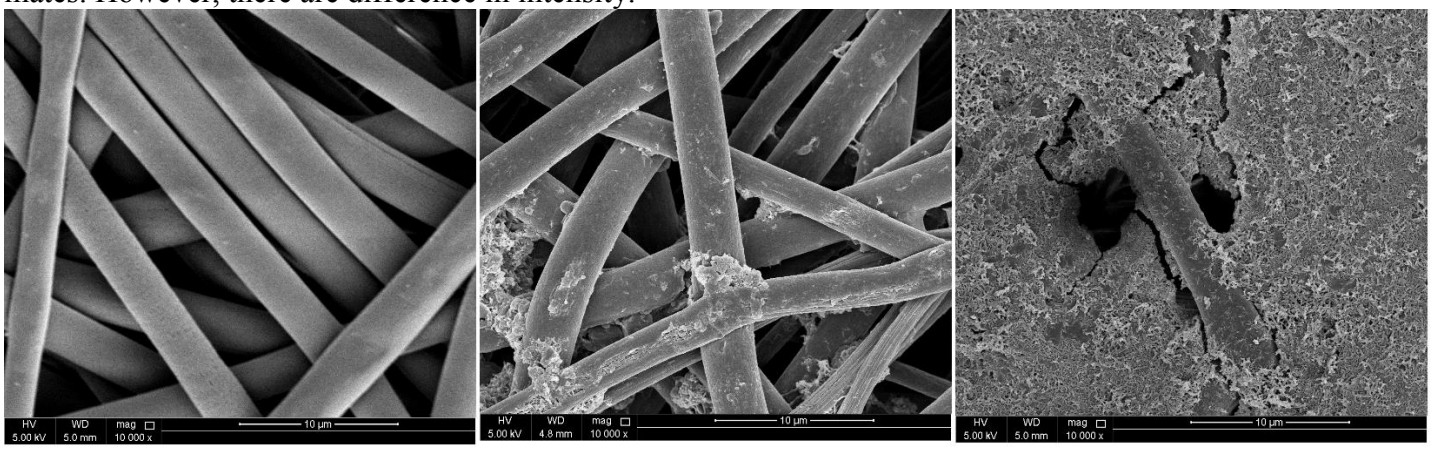

Figure 1: SEM images of (a) Electrospun PS fibers mat, (b) PANI coated PS fibers, (c) PANI-GO coated PS fiber

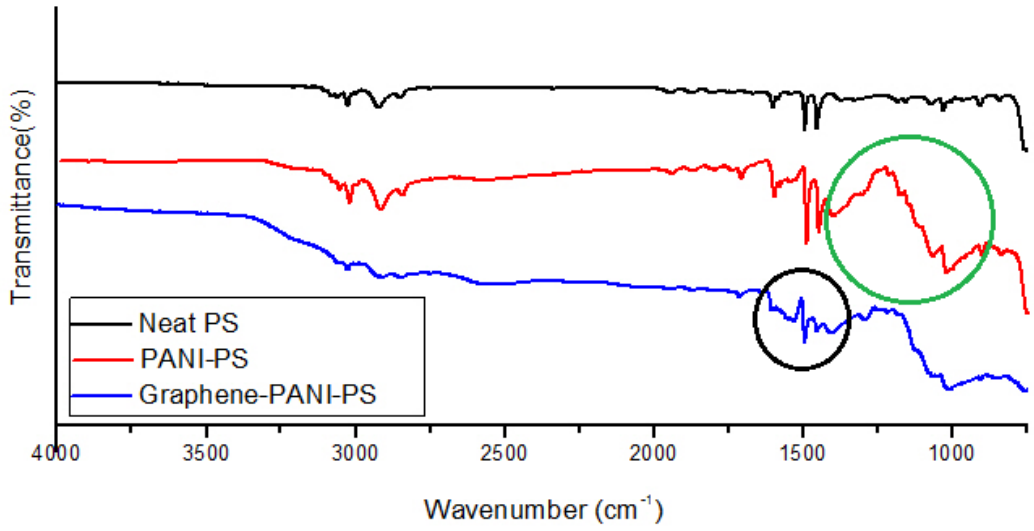

Figure 2: FTIR images of PS, PANI coated PS fibers and PANI-GO coated PS fiber

DOI: https://doi.org/10.26799/cp-nanotechfrance2018

3.3. Thermal Gravimetric Analysis

The TGA analysis of all the samples are done under heating rate of 10 min^{-1} from room temperature to 600 °C as shown in Figure 3. The results reveal that pure PS has one-step and 100% degradation at around 418 °C whereas the coated samples have multiple degradation steps. It can be seen that the thermal degradation of coated PS fibres start soon the rise of temperature, 30 °C. The initial 20% weight loss of lower temperatures are mainly due to evaporation of water (up to125 °C) and dopant anions (up to 435 °C). Above 435 °C the weight loss corresponds to the complete decomposition of the polymer. Observing the final degradation temperature, it has been found that GO-PANI coated PS fibre has highest thermal stability among all.

3.4 CO_2 sensitivity measurement

Gas sensitivity measurement of nanocomposite coated flexible sensors are done under continuum flow of gas at room temperature and relative humidity of 47%. A schematic diagram of setup used to measure gas sensitivity is shown in Figure 3. The whole system is divided into three sections, the gas sources, the measuring camber and the electrometer. The test sensor are placed inside the chamber with electrical connections. Test sensor are deposited with sliver electrodes and connection with copper wire. The chamber is connected to inlet and outlet for both air and CO_2 gases. Two-probe configuration determines the DC electric resistance of the samples exposed to CO_2 gas. The change in voltage of samples against constant current (0.1 μA) is measured by passing gas through the glass chamber at a fixed flow-rate. The obtained resistance are used to calculate sensitivity (S %) using the following equation,

$$S = \left[\Delta R / R_0\right] \text{----------(1)}$$

Where,$\Delta R = (R - R_0)$, R and R_0 represent the resistance of sensor measured in presence of analyte gas and air, respectively.

In the present study, the sensing capability of nanocomposite coated flexible polymer sensors towards CO_2 gas has been explored. Both PANI and PANI-GO nanocomposites coated gas sensors have been explored as a CO_2. Figure 4 describes sensitivity of PANI and PANI-GO nanocomposites coated gas sensors. From the Figure 5, it is clear that between two composites PANI-GO have higher sensitivity then PANI coated composite towards CO_2 gas. Response time and recovery time are found to 65 Seconds. Good repeatability as sensor is exposed with same concentration of CO_2 gas. Figure 6 shows increase in sensitive with increase in CO_2 gas concentration.

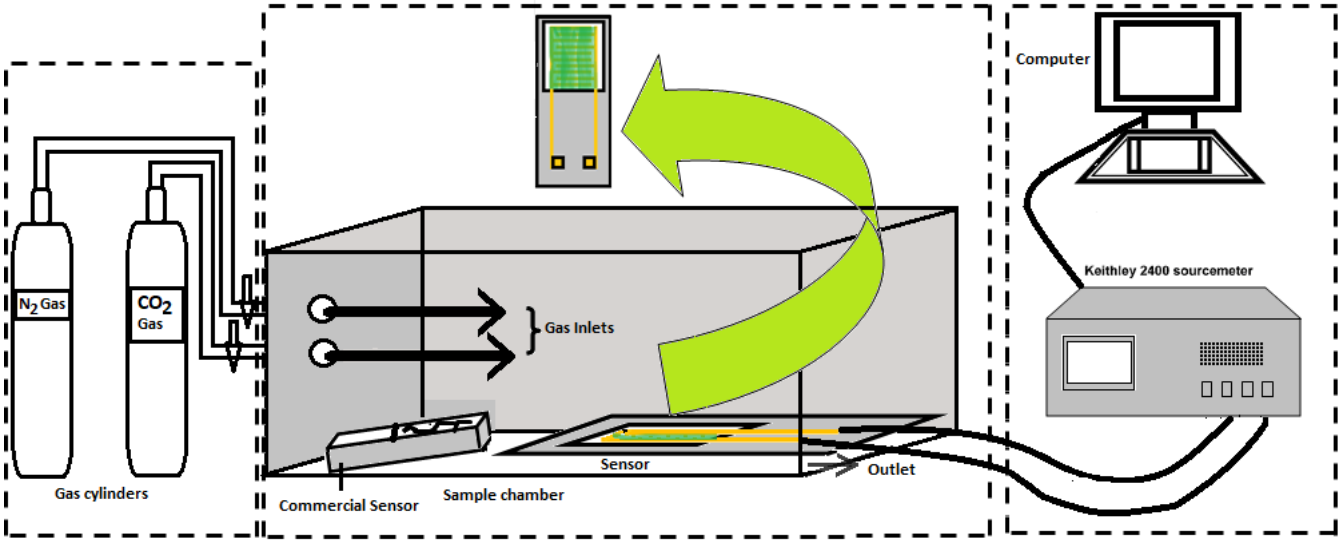

Proceedings of the Nanotech France 2018 International Conference (Nanotech France 2018)
Paris, France, June 27 - 29, 2018
DOI: https://doi.org/10.26799/cp-nanotechfrance2018

Figure 3: Schematic diagram of gas sensing setup.

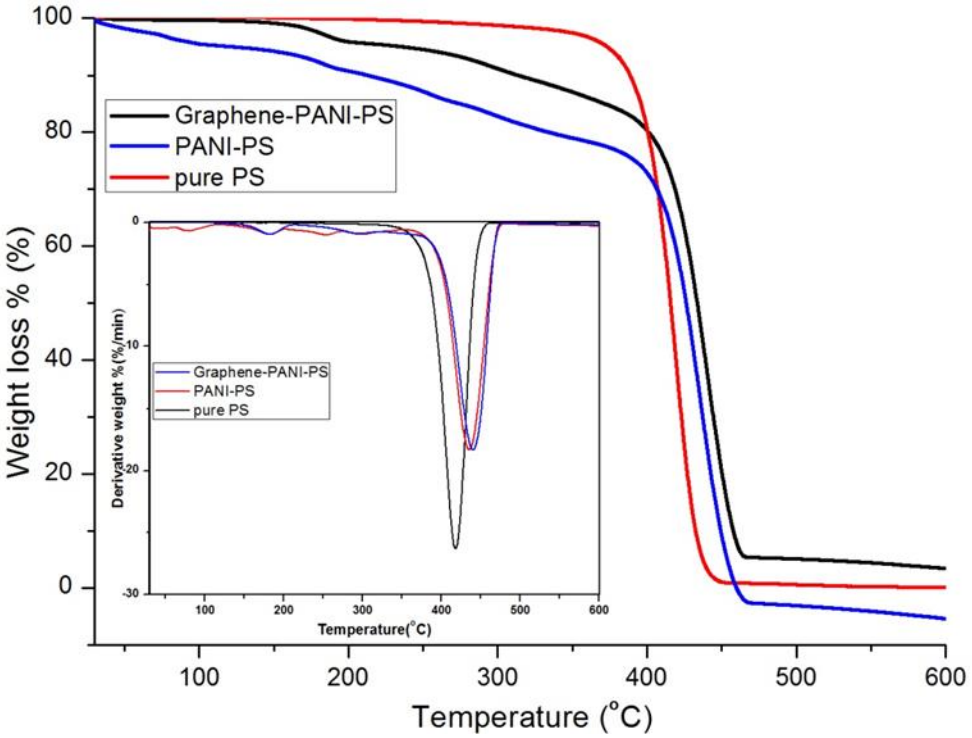

Figure 4: TGA and DTA thermogram of PANI and PANI-GO coated electrospin fiber and Pure PS.

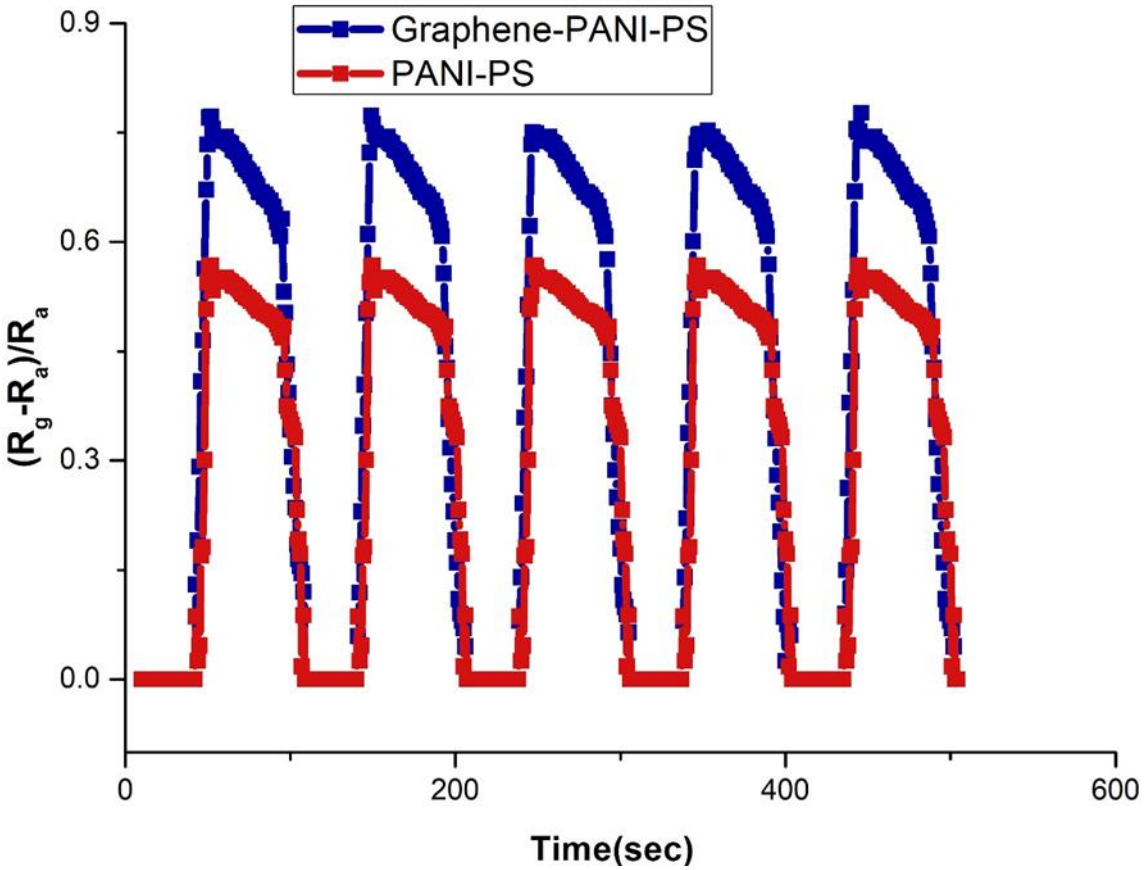

DOI: https://doi.org/10.26799/cp-nanotechfrance2018

Figure 5: Sensitivity of PANI-GO coated sensor towards different CO_2 concentration.

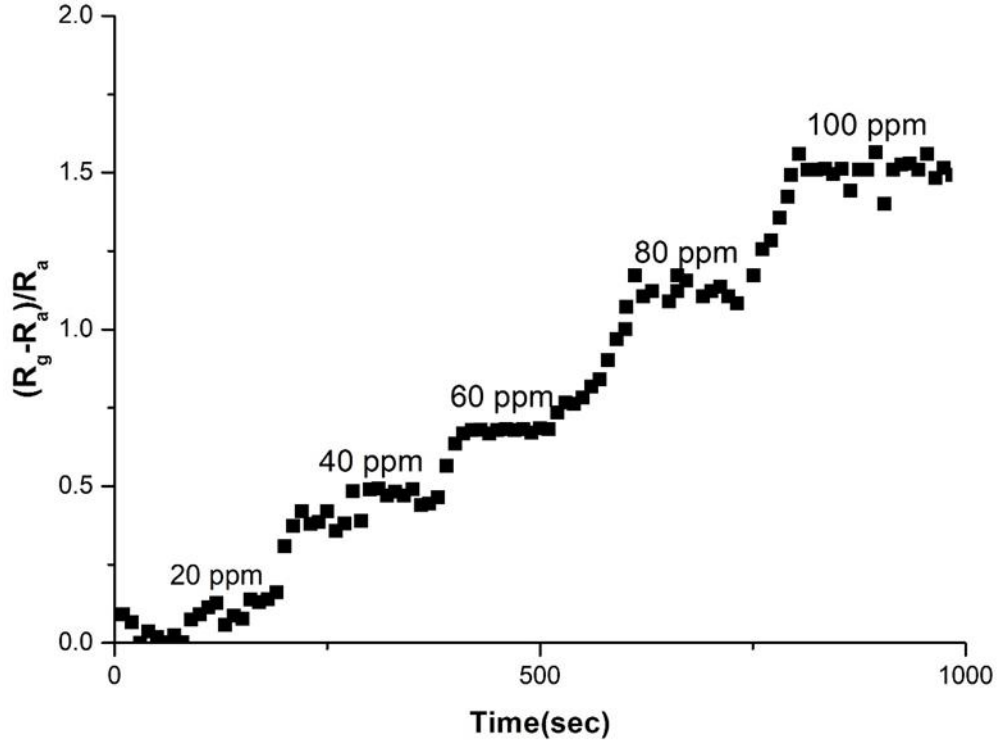

Figure 6: Repeatability of PANI and PANI-GO coated fiber CO_2 gas.

4. Conclusion

In this work, PANI and PANI-GO coated flexible gas sensors are prepared using insitu chemical polymerization casting method. Morphological studies reveals that size of electrospun pure PS microfiber 3μm and PANI nanofiber are 2-10 nm. In addition, SEM image shows uniform coating of nanocomposites around PS fibers. The presence of chemical interaction between polymers and nanocomposites are observed from the results of FTIR. Enhancement of thermal stability of nanocomposite coated PS fiber are noticed from thermal studies. Electrical conductivity values are increased due to addition of Graphene along with PANI during nanocomposite formation. Nanocomposite coated gas sensor had highest sensitivity towards CO_2 gas. Response time and recovery time are found to 65 Seconds. Good repeatability is observed as sensor is exposed with same concentration of CO_2 gas. Sensitive increases with increase in CO_2 gas concentration.

5. Acknowledgements

The authors express their deep sense of gratitude to students of Al-Bairaq for their contribution in the experimental work. Also supporting one of the authors to participate in the conference. Authors would also like to acknowledge the Office of Vice President for Research and Centre for Advanced Materials for the constant support during this research work.

6. References

1. W.Ting et al. , "Flexible Transparent Electronic Gas Sensors." , *Small,* vol. 12, no.28, pp.3748-3756, 2016.

2. C. Liu, et al. ,"Transparent air filter for high-efficiency PM2.5 capture.", *Nature Communications*, vol. 6, pp. 6205, 2015.

3. H. Bai and G. Shi, “Gas Sensors Based on Conducting Polymers." *Sensors,* vol. 7, no. 3, pp. 267-307, 2007.

4. K. C. Persaud, "Polymers for chemical sensing.”, *Materials Today*, vol. 8, no. 4, pp. 38-44, 2005.

5. V. Nair , “Role of electrospun ZnO-NiO metaloxide nanocomposite fibers for sensor applications”, in *proceedings of International Conference on Industrial Engineering and Operations Management (IEOM),* 2015.

6. J.Miao, M. Jianjun et al. “Electrospinning of nanomaterials and applications in electronic components and devices.” *Journal of nanoscience and nanotechnology*, vol.10, no. 9, pp. 5507-19, 2010.

7. Z. Ahmad, Q. Zafar, K. Sulaiman, R Akram and K. Karimov, ”A Humidity Sensing Organic-Inorganic Composite for Environmental Monitoring”. *Sensors,* vol.13, no.3, pp. 3615-3624, 2013.

8. I. Olenych, et al., “Organic-inorganic nanocomposites for gas sensing”, *in proceedings of International Conference Radio Electronics & Info Communications (UkrMiCo),* 2016.

9. C. Wang, L. Yin, L. Zhang, D. Xiang and R. Gao,”Metal Oxide Gas Sensors: Sensitivity and Influencing Factors”. *Sensors*, vol. 10, no.3, pp. 2088-2106, 2010.

10. B. Ding, M. Wang, J. Yu, and G. Sun, ”Gas Sensors Based on Electrospun Nanofibers”. *Sensors*, vol. 9 no.3, pp.1609-1624 ,2009.

11. A. N. Mallya, et al., "Conducting polymer–carbon black nanocomposite sensor for volatile organic compounds and correlating sensor response by molecular dynamics.", *Sensors and Actuators B: Chemical*, vol. 201, pp. 308-320, 2014.

12. F. Hossein-Babaei, and A. Hooshyar Zare ,"The selective flow of volatile organic compounds in conductive polymer-coated microchannels.", *Scientific Reports*, vol. 7, pp. 42299, 2017.

13. A. Haynes, and P.I. Gouma. “Polyaniline-Based Environmental Gas Sensors”. *Sensors for Environment, Health and Security, Dordrecht, Springer Netherlands*, 2009

14. J. Y. Shimano, and A. G. MacDiarmid "Polyaniline, a dynamic block copolymer: key to attaining its intrinsic conductivity?" *Synthetic Metals*, vol.123, no**.**2, pp. 251-262, 2001.

15. S.W. Ng, et al., "Graphene-based two-dimensional Janus materials.", *NPG Asia Materials*, vol. **10**, no. 4, pp. 217-237, 2018.

DOI: https://doi.org/10.26799/cp-nanotechfrance2018

16. V. Singh, et al., "Graphene based materials: Past, present and future." *Progress in Materials Science*, vol. 56, no.8, pp.1178-1271, 2011.

17. S. Basu, and P. Bhattacharyya, "Recent developments on graphene and graphene oxide based solid state gas sensors." *Sensors and Actuators B: Chemical* , vol. 173, pp. 1-21, 2001.

18. U. Latif and F. L. Dickert ,"Graphene Hybrid Materials in Gas Sensing Applications", *Sensors*, vol. 15, no.12, pp. 30504-30524, 2015.

Proceedings of the Nanotech France 2018 International Conference (Nanotech France 2018)
Paris, France, June 27 - 29, 2018
DOI: https://doi.org/10.26799/cp-nanotechfrance2018

Tunable Lipid Polymer Hybrid Nanoparticles for Enhanced Hydrophilic Drug Loading

Sara H. Omar[1], Rihab Osman[1], Wael Mamdouh[2]*, Gehanne A.S. Awad[1]
[1] Faculty of Pharmacy, Ain Shams University
African Union Organization St. Abbassia, Cairo, Egypt, sara_omar@aucegypt.edu
[2]The American University in Cairo (AUC), Department of Chemistry, School of Sciences and Engineering,
AUC Avenue P.O. Box 74, New Cairo 11835, Cairo, Egypt, wael_mamdouh@aucegypt.edu

Abstract
The emergence of nanotechnology has exerted remarkable impact on drug delivery; yet, encapsulation of water soluble drugs remains challenging. Efficacy of water soluble (hydrophilic) drugs is strongly limited by their poor intracellular absorption and rapid clearance. In addition, the leakage of water soluble molecules, from the polymeric matrix into the external phase, makes their encapsulation troublesome. Here, we report on the preparation of tunable hybrid lipid polymeric nanoparticles (NPs) that carried up to 51.29 ±1.5% of a cationic-hydrophilic drug. The Core shell (rivastigmine/ L-α-phosphatidylcholine / poly-lactide/glycolide) Riv/EPC/PLGA hybrid NPs showed an average diameter of 119.4±5.1 nm. The use of core shell hybrid NPs platform for efficiently delivering hydrophilic drugs is a promising approach with a very high potential in curing many diseases.

Keywords: lipid-polymer hybrid, nanoparticles, hydrophilic drugs, core-shell, bio-surfactant.

1 Introduction

Lipid polymer hybrids were developed to fabricate a combined superior drug delivery system, imitating the biological properties of the cell wall. The use of phospholipids privileges the architecture of a biodegradable hydrophobic polymer core with the flexibility of the liposome [1]. The polymer core and the lipid shell are strongly associated together *via* a variety of forces including hydrophobic interactions, van de Waal forces, and electrostatic interactions with other non-covalent forces. Hence, hybrid nano-platforms provide an opportunity to overcome the low liposomes stability and provide a tunable drug release profile [1]. Hydrophilic drugs which are generally poorly associated with hydrophobic polymers or suffered from premature leakage from liposomes can be better entrapped in these hybrid systems.

Hydrophilic drugs suffer from the disadvantage of enzymatic degradation, poor distribution and short half life, which compels frequent dosing[2]. This minimizes their therapeutic values and increases their side effect as well as patient discomfort. Hydrophilic moieties' restricted clinical application is majored in central nervous system (CNS) and tumor diseases. Since they do not pass the BBB (in case of CNS therapeutics), and are not being retained within tumour in case of antitumor drugs[3]. Strategies to improve therapeutic values of such molecules have been limited due to the difficulty in achieving high encapsulation efficiency, due to drug leakage in the external media[4]. In this work, the incorporation of the model hydrophilic drug, Riv, in the designed lipid polymer platform will be considered with the aim of achieving a high loading efficiency. Riv acts as an acetylcholinesterase inhibitor in dementia diseases and Alzheimer[5].

Synthesizing hybrid platforms are usually achieved through different methodologies, yet, smallest particle size has been reported with nanoprecipiation method[6]. The use of the nanoprecipitation method for the production of this newly introduced delivery system had been reported to be a simple rapid-single step method of preparation [4]. Nanoprecipitation occurs by a rapid diffusion of the organic phase and the polymer into the aqueous non-solvent phase [7]. Once the polymer has migrated into the aqueous medium, it is immediately precipitated entrapping the drug. Therefore, this method is more suitable for encapsulating hydrophobic drug [4]. Thus, using nanoprecipitation for encapsulating hydrophilic substances, inside the polymer capsules, remains a challenging task. Among the methods introduced to increase the encapsulation of hydrophilic drug is changing the outer phase pH or changing solvent/ anti solvent composition [8,5].

Nonetheless, the limit to encapsulate cationic drug in hybrid lipid/polymeric NPs using nanopreicipition remains more challenging. Cationic drugs sometimes fail to be entrapped into lipid-polymeric NPs, and even fail to form NPs [9].This

DOI: https://doi.org/10.26799/cp-nanotechfrance2018

was ascribed to a sort of interaction that occurs between the anionic PC and the cationic drug [1]. To overcome these challenges, we improved the entrapment efficiency of cationic-hydrophilic drug in hybrid lipid polymeric NPs. We first optimized the NPs formation environment, using conventional surface active agents (C-SAA) and bio-surfactant (B-SAA), as a function of size. Then a layer of lipids was introduced and decorated with anionic bio-SAA to allow for rapid diffusion within tissues. The formulated platform was then loaded with drug using different S/AS systems. This novel platform represents a new approach for delivering a high payload of water soluble molecules.

2 Materials and methods:

Poly (lactic-*co*-glycolic acid) (PLGA) copolymer, PURASORB PDLG (DL-lactide and glycolide) 5002A (50/50 DL-lactide/glycolide copolymer acid terminated) were kindly provided by Purac Biomaterials (Gorinchem, The Netherlands). Rivastigmine tartarate HCl (Riv) was kindly provided by (Hikma co., Egypt). L-α-phosphatidylcholine(EPC), from dried egg yolk, Poloxamers (P-188) and (P-407) were purchased from Sigma chemical co., USA. Phosphatidylethanolamine from egg yolk (PE) was kindly provided by lipoid company (Switzerland). Sodium cholate (NaC), Taurodeoxycholic acid (TDA), Taurocholic acid (TCA) and Soybean lecithin (SPC) were purchased from Fluka, Germany. Polyvinyl alcohol (PVA), Mw 31,000 was purchased from Sigma-Aldrich, UK. Acetonitrile and ethanol absolute (both HPLC grade) were purchased from Fisher Scientific UK Bishop meadow road, Loughborough). Dialysis tubing (visking diameter 28mm) MWCO 12.000-14.000 were purchased from Serva, Germany. All other chemicals and reagents were of analytical grade and were used without further modification.

2.1 Optimization of plain PLGA-NPS prepared with C- SAA and B-SAA

Blank PLGA-NPs were prepared by the nanoprecipitation method [10]. Briefly, accurately weighed PLGA dissolved in the organic solvent was added dropwise/at once on the aqueous phase containing a SAA with magnetic stirring at specified rpm and time. The system was left for stirring at 750 rpm at room temperature for organic solvent removal. The prepared dispersions were then purified by dialysis against frequently renewed distilled water for 12 h. The obtained samples were either directly characterized for particle size (PS) and zeta potential or freeze dried. For drug loaded NPs, the drug was added to the organic phase. Results were performed in duplicates of different batches. The investigated process and formulation variables are shown in table 1.

2.2 Synthesis of Riv-EPC/PLGA hybrid NPS

Hybrid lipid polymeric NPs were prepared adopting one step approach following a modified protocol of (Chan et al., 2009) [11]. Briefly, PLGA and drug were dissolved in water miscible organic solvent, while, the aqueous phase contained the lipids, B-SAA (unless else mentioned). Organic phase was added on the aqueous phase at once, under stirring at 1000rpm and the procedure was completed as before under section 2.1. Results were performed in triplicates of different batches.

2.3 NPs characterization

Particle size (PS) and Zeta potential (ζ) determination:

Freshly prepared dispersions were used for PS determination using Malvern Zetasizer ZS-Nano after proper dilution. Dynamic light scattering technique was used to determine the hydrodynamic average diameter expressed in intensity and the PS distribution expressed as PDI. The surface charge for selected NPs was determined by the measurement of the ζ of the freshly prepared NPs dispersion using zetasizer. ζ was calculated according to Helmholtz Smoluchowsk from NPs electrophoretic mobility [12]. Before determination, all samples were diluted with distilled water to the same concentration used in PS analysis.

2.3.2 Morphological examination:

Physical dimension of NPs was assessed on Field emission scanning electron microscope (FESEM) and a JEM-HR_2100, TEM instrument, following (Y. Hu et al. 2015) [13].

2.3.3 Drug loading determination:

Riv chromatographic separation was carried out using reverse phase C-18 column using a mobile phase consisting of acetonitrile, acetate buffer (20 mM) 35:65 (v/v) adjusted to pH 6.4 with acetic acid. The elute flow rate was 1 mL/min with injection volume of 20 uL, was monitored at 220 nm wavelength [14].

DOI: https://doi.org/10.26799/cp-nanotechfrance2018

For drug loading and encapsulation, an accurately weighed amount of the freeze dried powders (5mg) was dispersed in 1 mL of alkaline (0.1 N NaOH) 0.5% SDS [15]**.** After stirring for a night, the clear solutions were filtered using a nylon syringe filter (0.22µm), and assayed for drug concentrations.
Encapsulation efficiency and loading capacity percentage was calculated using Eqs. (1) and (2) below:

$$\text{EE (\%)} = [\text{Actual drug in freeze dried/ Initial drug added}] * 100 \quad (1)$$

$$\text{LC (\%)} = \left[\text{Entrapped } \frac{\text{Drug}}{\text{NPs}} \text{ weight}\right] * 100 \quad (2)$$

1. Results and discussion

In this work, lipid polymer hybrids were prepared using nanoprecipitation method. Aiming at producing NPs in the range of 100nm, we started by optimization PLGA NPs size. Thereafter, we adjusted lipid polymer ratio to secure highest possible load with minimum size. The major factors to be optimized were: PS, PDI and zeta potential.

3.1 Optimization of the preparation protocol:

Optimized parameters were: 1) process variables, 2) organic to aqueous volume ratio, 3) polymer concentration and solvent/antisolvent type and 4) SAA type and concentration.

Error! Reference source not found. Smaller PS with narrower PDI was obtained with the high flow rate (turbulence) of aqueous phase. NPs prepared at a ratio of 1:2 polymer/SAA, recorded the least PS. Size reduction, down to (82.4-83.8 nm) was also seen with acetonitrile in the organic phase, along with 15% ethanol in the aqueous phase, when used in the ratio of 1:2 with the least polymer concentration (0.125%). These results were in accordance with literature where they reported the major role of polymer concentration in controlling PS, since PS enlargement was observed with higher concentrations of PLGA [4] [10].
Surface coating with P-188 displayed the smallest PS as compared to other C-SAA. Moreover, being an ionized, natural SAA(NaC); as a bile salt, gave NPs with the smallest PS (36.8-40 nm) with a relatively high zeta potential (-43.8mV).

3.2 Characterization of plain PLGA-SAA NPs

The size and morphology of the selected NPs (with C-SAA and B-SAA) were characterized by TEM and SEM. Figure 1 shows spherical non-aggregated homogeneously dispersed NPs. The NPs size was in agreement with the PS measured by dynamic light spectroscopy.

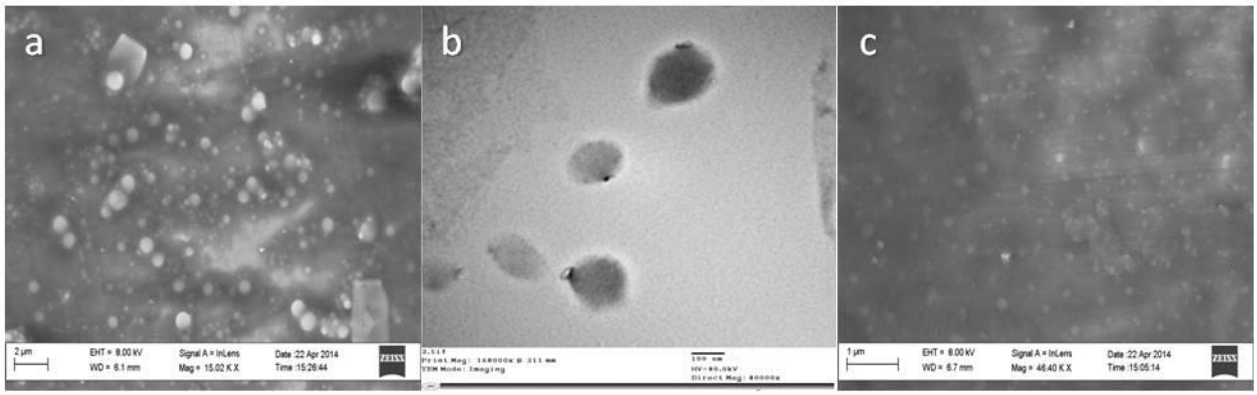

Figure 1: SEM (a) and TEM (b) images of C-SAA (P-188)/PLGA NPs and SEM (c) of B-SAA(NaC)/PLGA -NPs

3.3 Riv-EPC/PLGA hybrid lipid polymeric NPs

3.3.1 Effect of solvent/antisolvent system on size of PLGA hybrid lipid polymeric NPs

Figure 2(a), depicts the slight but significant increase in PS that appeared when the concentration of ethanol in the aqueous phase was subjected to an increase, till 0.25% ethanol, followed by an abrupt particle enlargement at 50%

DOI: https://doi.org/10.26799/cp-nanotechfrance2018

ethanol. Meanwhile the PDI exhibit a fluctuating pattern where the least value was seen with 15% ethanol followed by a sharp decrease, ending up with minimal values at higher ethanol percentages.

Among the three phospholipids, EPC was preferred over SPC regarding the size and PDI, Figure 2b. Confirming the assembly of PLGA NPs coated with the lipids, hybrid NPs was characterized using SEM (Figure 3a), as well as TEM (Figure 3b). Small spherical NPs with similar morphology and smooth surfaces were detected by SEM. The TEM clearly evidenced the formation of a continuous thick lipid coat around the polymeric particles confirming the preparation of hybrid core shell lipid polymer particles.

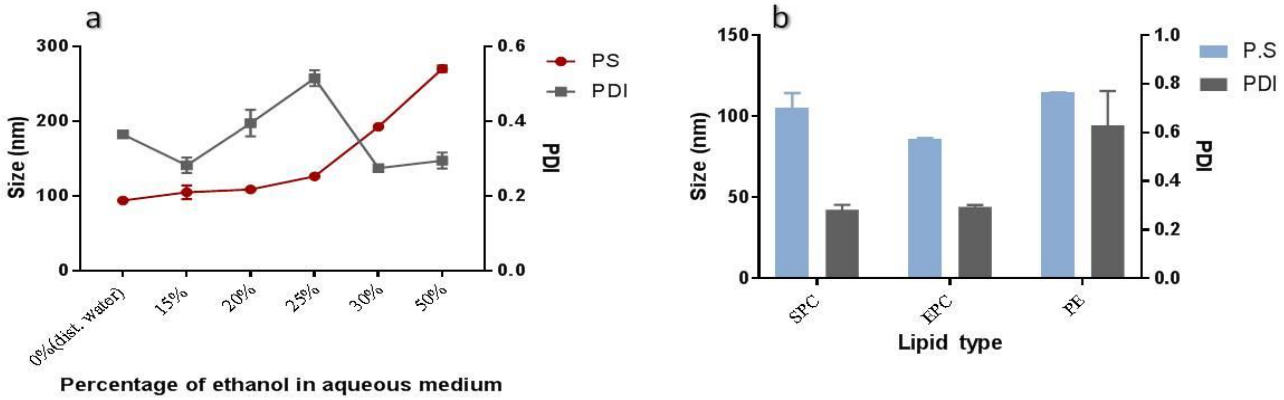

Figure 2: (a) Influence of ethanol on PS and PDI; (b) Influence of lipid type on PS and PDI of hybrid NPs.

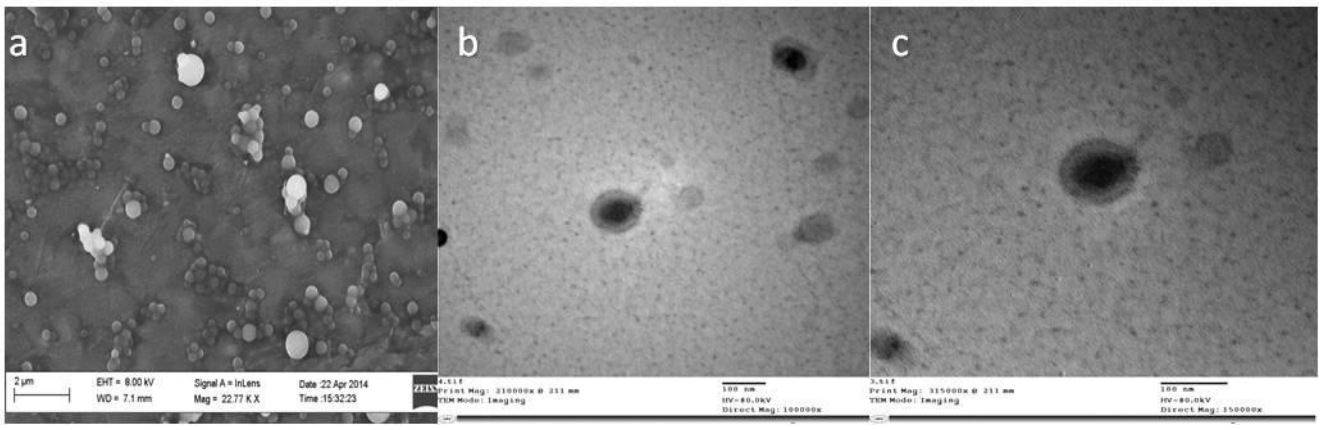

Figure 3: (a) SEM image showing spherical hybrid lipid polymeric NPs; (b,c) TEM images showing core shell structure of EPC-PLGA- NPs

Addition of Riv drug caused a significant increase in size from 86.5±1.1nm to 119.4±5.1 and 121.2±4.8nm prepared with 1:10 and 2:10 drug to polymer ratios, respectively. This increase in size was accompanied by respective drug EE% of 51.29±1.5 and 15.4±4.08 %, Figure 4. Cationic drugs were reported to be difficulty encapsulated into lipid-polymeric NPs, and sometimes it is their presence causes a failure of formation of NPs [9]. Poor encapsulation was due to a sort of interaction that occurs between the anionic PC and the cationic drug (Riv), impeding availability of free drug for encapsulation during the self - assembly of PLGA NPs [1]. Cheow and *co*-workers solved the problem by replacing some of the PC with cationic repelling lipids. To break the cationic drug - anionic lipid interaction [16]**.** However in our study the inclusion of NaC in a specified amount increased the EE% to 51.29%. The ionic interaction of Riv with BS ions, due to the formation of lipophilic ion-pair rendered the drug less soluble in the aqueous media, resulting in higher encapsulation and less drug leak.

DOI: https://doi.org/10.26799/cp-nanotechfrance2018

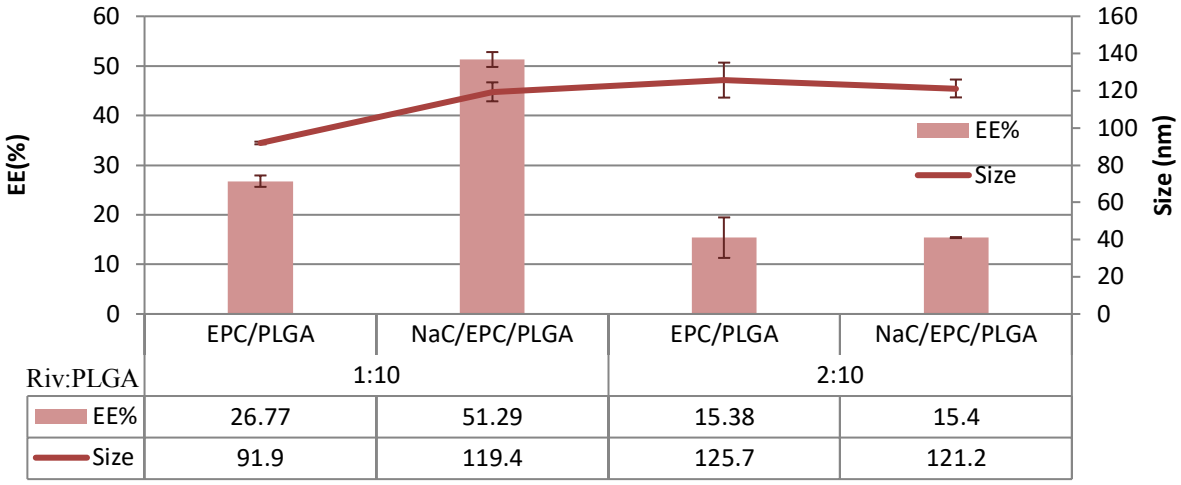

Figure 4: Size and EE% of hybrid NPs prepared from different ratios of drug: polymer

Among the approaches reported in literature to increase EE% of Riv, are: 1) using basic external media PH 9, 2) using Riv free base, 3) and incorporating Riv into liposomes in the presence of cationic lipids. For instance, Tamilselvan et al. increased the encapsulation of Riv in PLGA /P-127 NPs- using nanoprecipiation by raising the aqueous media pH to 9 [17]. NPs ranged in size from 110±12 to 240±5 and in EE% from 62.4±1.5 to 85.9±1.8 depending on the ratio of the drug to polymer and PH of AS. On the meantime, Riv liposomes were prepared in the size range of 67.51- 528.7 nm and had the EE of 84.4-97.4%, varying according to ratios of PC, dihexadecyl phosphate and cholesterol, [18]. It is worth mentioning that for liposomes, Riv was loaded into Didecyldimethyl ammonium bromide (DDAB), with/without Tween 80. Liposomes had the size of 373.3-6324 nm and EE 33.6-60%, [19]. Soya lecithin and cholesterol were formerly used in the preparation of microparticles of Riv in the size of 10.0 ± 2.8 mm with 80.0 ± 5.0 EE %. Another report showed successful loading of Riv onto the functionalized and non funtioncalized mesoporous silica NPs with maximum EE% of 41%, [20]. Meanwhile, in this research we introduced a new S/AS for the increasing the EE% of Riv as well as keeping a small size ~100 nm.

Conclusion

Among the experimental parameters, addition of organic phase at once in combination with high stirring speed was found to yield smaller PLGA-NPs in diameter. Polymer concentration was found to have a positive effect on increasing the size. Acetonitrile, in ratio of 1:2(organic: aqueous), yielded smaller NPs as compared to acetone. Ratio of SAA/P was the key player along with the concentration of polymer. The ratio 2:1 SAA/P showed the least PDI and size decreased with different low concentrations depending on the type of surfactant. In a contrasting fashion, polymer concentration and B-SAA had a positive effect on decreasing PS and PDI of NPs. As compared to water, 15% ethanol in the non-solvent phase enhanced PDI of NPs prepared from PLGA with NaC. Upon comparing three types of natural lipids, EPC was found to give optimum size and PDI when used in the ratio of 2:20 L/P with NaC.

References

1. B. Mandal, H. Bhattacharjee, N. Mittal, H. Sah, P. Balabathula, L. A. Thoma, and G. C. Wood, "Core – shell-type lipid – polymer hybrid nanoparticles as a drug delivery platform," *Nanomedicine Nanotechnology, Biol. Med.*, vol. 9, no. 4, pp. 474–491, 2013.
2. S. Arpicco, L. Battaglia, P. Brusa, R. Cavalli, D. Chirio, F. Dosio, M. Gallarate, P. Milla, E. Peira, F. Rocco, S. Sapino, B. Stella, E. Ugazio, and M. Ceruti, "Recent studies on the delivery of hydrophilic drugs in nanoparticulate systems," *J. Drug Deliv. Sci. Technol.*, vol. 32, pp. 298–312, 2016.
3. E. Nance, C. Zhang, T. Y. Shih, Q. Xu, B. S. Schuster, and J. Hanes, "Brain-penetrating nanoparticles improve paclitaxel efficacy in malignant glioma following local administration," *ACS Nano*, vol. 8, no. 10, pp. 10655–10664, 2014.

4. U. Bilati, E. All, and E. Doelker, "Development of a nanoprecipitation method intended for the entrapment of hydrophilic drugs into nanoparticles," vol. 24, pp. 67–75, 2005.
5. A. K. Seth, S. Kumar, and Y. C. Yadav, "pharma science monitor an international journal of pharmaceutical sciences development of a rapid , accurate and sensitive uv spectroscopic method for estimation of rivastigmine tartrate entrapped in nanoparticles," no. 3, pp. 216–235, 2011.
6. L. I. Zhang and L. Zhang, "Lipid polymer hybrid nanoparticles: synthesis, characterization and applications," vol. 1, pp. 163–173, 2010.
7. K. Miladi, S. Sfar, H. Fessi, and A. Elaissari, *Polymer Nanoparticles for Nanomedicines*. 2016.
8. T. Govender, S. Stolnik, M. C. Garnett, L. Illum, and S. Davis, "PLGA nanoparticles prepared by nanoprecipitation : drug loading and release studies of a water soluble drug," vol. 57, pp. 171–185, 1999.
9. W. S. Cheow and K. Hadinoto, "Colloids and Surfaces B : Biointerfaces Factors affecting drug encapsulation and stability of lipid – polymer hybrid nanoparticles," *Colloids Surfaces B Biointerfaces*, vol. 85, no. 2, pp. 214–220, 2011.
10. S. A. Joshi, S. S. Chavhan, and K. K. Sawant, "European Journal of Pharmaceutics and Biopharmaceutics Rivastigmine-loaded PLGA and PBCA nanoparticles : Preparation , optimization , characterization , in vitro and pharmacodynamic studies," *Eur. J. Pharm. Biopharm.*, vol. 76, no. 2, pp. 189–199, 2010.
11. J. M. Chan, L. Zhang, K. P. Yuet, G. Liao, J. Rhee, R. Langer, and O. C. Farokhzad, "Biomaterials PLGA – lecithin – PEG core – shell nanoparticles for controlled drug delivery," *Biomaterials*, vol. 30, no. 8, pp. 1627–1634, 2009.
12. H. Xu, Y.-H. Deng, K.-Q. Wang, and D.-W. Chen, "Preparation and Characterization of Stable pH-Sensitive Vesicles Composed of α-Tocopherol Hemisuccinate," *AAPS PharmSciTech*, vol. 13, no. 4, pp. 1377–1385, 2012.
13. Y. Hu, R. Hoerle, M. Ehrich, and C. Zhang, "Engineering the lipid layer of lipid-PLGA hybrid nanoparticles for enhanced in vitro cellular uptake and improved stability," *Acta Biomater.*, vol. 28, pp. 149–159, 2015.
14. K. Arumugam, M. R. Chamallamudi, R. R. Gilibili, R. Mullangi, S. Ganesan, S. S. Kar, R. Averineni, G. Shavi, and N. Udupa, "Development and validation of a HPLC method for quantification of rivastigmine in rat urine and identification of a novel metabolite in urine by LC-MS/MS," *Biomed. Chromatogr.*, vol. 25, no. 3, pp. 353–361, 2011.
15. P. Subbarayan, V. A. Dennis, C. Lee, E. Nyairo, and S. R. Singh, "Encapsulation and in vitro characterization of protein in PLGA-chitosan nanoparticles for efficient drug delivery," *Tech. Proc. 2011 NSTI Nanotechnol. Conf. Expo, NSTI-Nanotech 2011*, vol. 3, pp. 348–351, 2011.
16. A. Ranganathan, R. Hindupur, and B. Vallikannan, "Biocompatible lutein-polymer-lipid nanocapsules: Acute and subacute toxicity and bioavailability in mice," *Mater. Sci. Eng. C*, vol. 69, pp. 1318–1327, 2016.
17. N. Tamilselvan, C. V. Raghavan, K. Balakumar, and S. Karthik, "in Pharmaceutical and Nano Sciences brain targeted delivery of rivastigmine polymeric nanoparticles through oral administration to treat," vol. 3, no. 6, pp. 536–551, 2014.
18. M. F. Ismail, A. N. Elmeshad, and N. Abdel-hameed, "Potential therapeutic effect of nanobased formulation of rivastigmine on rat model of Alzheimer ' s disease," pp. 393–406, 2013.
19. S. N. El-helaly, A. A. Elbary, M. A. Kassem, and M. A. El-, "Design , Development and Statistical Evaluation of Positively Charged Rivastigmine Liposomes," vol. 2014, no. 4, pp. 1–8, 2014.
20. M. Karimzadeh, L. Rashidi, and F. Ganji, "Mesoporous silica nanoparticles for efficient rivastigmine hydrogen tartrate delivery into SY5Y cells," *Drug Dev. Ind. Pharm.*, vol. 43, no. 4, pp. 628–636, 2017.

Proceedings of the Nanotech France 2018 International Conference (Nanotech France 2018)
Paris, France, June 27 - 29, 2018
DOI: https://doi.org/10.26799/cp-nanotechfrance2018

Tunnel Barrier Optimization for Room Temperature Operation of Single Electron Transistors

Raj Shah, Rasika Dhavse
Department of Electronics Engineering, SVNIT, Surat, Gujarat, India

Abstract
Room temperature operation of Single Electron Transistors (SET) and its CMOS process compatibility open up a new window of hybrid SET-MOS circuits for ultra-low power and/or high-performance applications. For successful operation of SET at room temperature, Coulomb Blockade (CB) and Quantum Mechanical Tunneling (QMT) must be witnessed. As CB and QMT depend profoundly on tunnel barriers, there has to be strategic barrier optimization. This paper proposes barrier engineering of a grounded gate SET. It employs aluminum island in UTB SOI device with poly source and drain. SiO_2 tunnel barrier is optimized between 1 nm to 4 nm to obtain room temperature operation and enhance current driving capability of the SET. Mathematical analysis for all SET structures is carried out using orthodox theory of CB and QMT while Sentarus TCAD is used for process simulation and device characterization. CMOS compatible processes have been used for process simulation of SET for all tunnel barrier thicknesses. Schenk direct tunneling model, doping dependent mobility model and default drift diffusion model are incorporated for device operation. CB and QMT have been analyzed at room temperature using current-voltage (I-V) and charge-voltage (Q-V) characteristics. This analysis is further extended to compare the CB voltage (V_{CB}) and change in electrostatic charging energy (ΔE) with simulated results. Tunnel barriers of 3 nm and 4 nm thicknesses unveil notable CB of 23.44 mV and 40.80 mV with tunneling current of 0.072 μA, and 0.00715 μA respectively, at room temperature.

Keywords: single electron transistor, tunnel barrier optimization, room temperature operation, Coulomb blockade, quantum mechanical tunneling, TCAD

1. Introduction

Single Electron Transistors (SETs); enable high level of integration and huge power reduction over conventional CMOS [1]. By virtue of process compatibility and hybridization capability of SET with CMOS [1-3], recently SET-MOS hybrid circuits are proposed for ultra-low power and/or high-performance applications. However, to facilitate mass production of such hybrid circuits and consequently chips, it is compulsory to ensure stable room temperature operation of SETs.

SETs are made up of two tunnel junctions having a common quantum dot island. They are governed by two principle mechanisms viz: Coulomb Blockade and Quantum Mechanical Tunneling (QMT), which drive the device OFF and ON, respectively. The Coulomb Blockade energy, E_C which is to be overcome to cause QMT across the tunnel junction is given by Eq. (1),

$$E \quad /_2 \tag{1}$$

Room temperature operation of SET for an advanced technology node thus demands hyper-downsizing of tunnel junction capacitance. It is obtained by shrinking the quantum dot island. This requires very high precision process control and is limited to few samples only which restrict the reproducibility/repeatability of the device for large scale processing [4-6]. Alternately, tunnel barriers can be engineered so as to achieve lower value of tunnel junction capacitance. Various dielectric stacks have been proposed for tunnel barriers like TiO_x–TiO_2, TiO_x-Al_2O_3 stacks and WSe_2-WTe_2 [7, 9]. However, stacking different dielectrics lead to process complexity and device reliability issues. The tunnel barrier should have good adhesiveness of dielectric material with island and source/drain to restrict the defects and reproducibility of the device. As such, the obvious choice for dielectric material is Silicon Dioxide. In this work, SiO_2 thickness has been optimized to scale down the junction capacitance of a SET over SOI wafer for room temperature operation. Strategic modeling and planning of the device is presented with comprehensive analysis. Sentaurus TCAD tools are used for simulations. The characteristics are plotted to evaluate the effect of tunnel barrier on Coulomb Blockade and QMT mechanisms at room temperature.

2. Tunnel Barrier Modeling in SET

2.1. Theoretical Modeling of SETs

Proceedings of the Nanotech France 2018 International Conference (Nanotech France 2018)
Paris, France, June 27 - 29, 2018
DOI: https://doi.org/10.26799/cp-nanotechfrance2018

SET structure is demonstrated in Fig. 1a shown below.

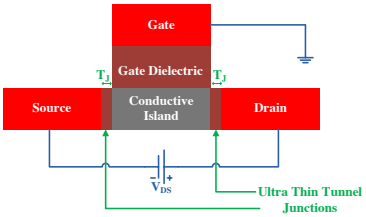

Fig. 1a: SET Structure.

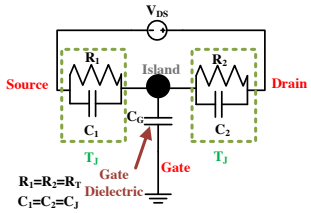

Fig. 1b: SET Equivalent Circuit.

It has a conductive nano-island, surrounded by two identical tunnel junctions with thicknesses T_J. Tunnel barrier thickness should offer sufficient barrier height to support CB to achieve low OFF current and provide sufficiently small barrier width to allow QMT ascertaining high ON current [7]. The gate voltage tunes the current in island by controlling number of electrons through gate capacitance, C_G. Thermal energy plays important role at higher temperature by contributing energy to electrons. The equivalent circuit for SET is shown in Fig. 1b. Voltage source V_{DS} has been applied at drain to source while gate has been grounded. The dot shown at centre is an island and the tunnel barriers are represented by RC combination where R is the tunnel resistance which should be higher than quantum resistance [8]. The voltage at an island when n number of electrons present is given by [7],

(2)

where, Q_0 is the background charge and C_T is total island capacitance ($2C_J + C_G$). The voltage required to tunnel an electron from/to the island and is given by [8],

(3)

where, V_{CB1} is the coulomb blockade voltage in Volts and C_J is the junction capacitance in attofarad. Source to drain tunneling voltage under the influence of gate voltage is [8],

(4)

where, V_{CB} is the total coulomb blockade voltage in Volts. The change in electrostatic energy due to tunneling of single electron in eV is given by [8],

(5)

If T=0 and there are n electrons then it is given by,

(6)

which should be greater than zero for each tunneling event, e is the elementary charge of an electron, K_B is the Boltzmann constant and T is temperature in K.

2.2. Strategy for Tunnel Barrier Optimization

From (3) to (9), it is clear that increase in the T_J decreases C_J. As C_J decreases, C_T also decreases and it leads to increase in the V_{CB} and ΔE. Increase in ΔE further leads to decrease in the r_i which ultimately decrease the tunneling current. Similarly decreasing the T_J lead to decrease CB region and increase QMT. So, for successful room temperature operation of SET, T_J can be optimized strategically.

3. Device Structure and Physical Models

3.1 Process Simulation

Fabrication process flow for the proposed device is shown in Fig. 2.

Proceedings of the Nanotech France 2018 International Conference (Nanotech France 2018)
Paris, France, June 27 - 29, 2018
DOI: https://doi.org/10.26799/cp-nanotechfrance2018

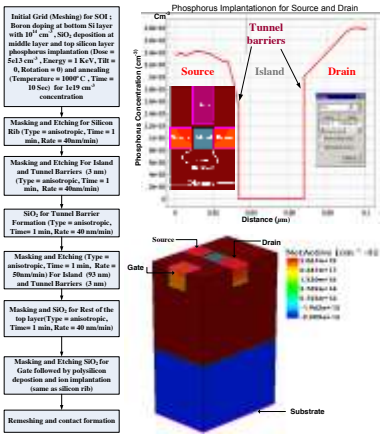

Fig. 2: Process Flow, Doping Profile and SET Structure.

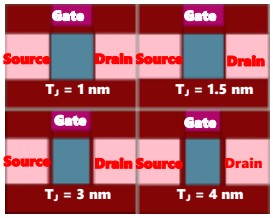

Fig. 3: Simulated SET Structures.

Table 1 Capacitance Calculations

T_J (nm)	C_J (aF)= $\epsilon_{OX}A_J/T_J$	C_G (aF)= $\epsilon_{OX}A_G/d_G$	C_T (aF)= $(2C_J+C_G)$
1	42.16	1.49	85.85
1.5	28.10	1.35	57.55
3	14.05	1.07	29.17
4	10.54	0.7	21.78

SOI wafer has 150 nm thick boron implanted (10^{14} cm^3) silicon bottom layer, 150 nm thick BOX (SiO_2) layer and 40 nm thick phosphorus implanted (10^{19} cm^3) silicon top layer. Two ultra-thin tunnel junctions (1 nm to 3 nm) of SiO_2 surround a 28 nm wide aluminum island. N-type doped polysilicon side gate is aspirated from the island with 30 nm gap consists the oxide layer (SiO_2) as gate dielectric. Island is capped from all directions by depositing SiO_2. Tunnel barrier optimization can be noticed from the Fig. 3. The Table 1 shows the calculated values of capacitances for all structures.

3.2 Device Simulations

The current density in the device majorly depends upon the tunneling process. So, the Direct Tunneling model by Schenk has been used at the silicon/oxide interfaces. The other physics models used for device characterization are Masetti and Phillips Unified Mobility models for accounting doping and temperature dependency, Band2Band Schenk Recombination model for rapidly varying electric field at insulator and Barrier Lowering model at metal/oxide interface due to image force effects [10].

4. Results and Analyses

This paper concentrates on tunnel barrier engineering for room temperature operation of SET. Junction capacitances of the device are varied by altering the tunnel barrier thickness from 1 nm to 4 nm. Since CB and QMT are to be observed exclusively, the gate has been grounded. Fig.4 shows the effect of the barrier thickness on the device conduction at room temperature.

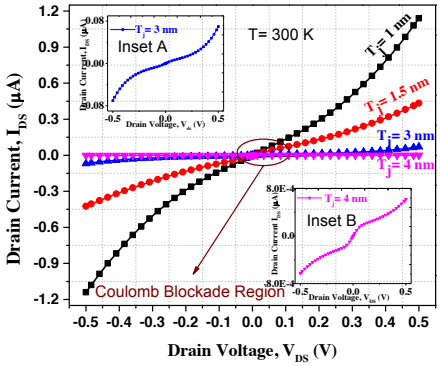

Fig. 4: Output Characteristics at Room Temperature.

Table 2 Extracted I_{ON} at Room Temperature

T_J (nm)	I_{ON} (μA)
1	1.18
1.5	0.45
3	0.072
4	0.00715

Table 3 Comparison of I_{ON}

Ref.	I_{ON} (μA)
[3]	0.004
[5]	0.002
[6]	60e-6
[7]	0.1
This Work	1.18

It is observed that the device is highly symmetrical indicating reversible nature of CB and QMT. It is observed that the tunneled current inversely depends on the barrier thickness. The CB can be clearly observed for 3 nm and 4 nm tunnel barrier structures at room temperature. For 1 nm and 1.5 nm tunnel barrier structures, thermal energy overcomes CB and significant tunneling current is observed. This experimentation has led to a conclusion that devices with 3 nm and 4 nm tunnel junction barriers exhibit both CB and QMT satisfactorily in the regime of consideration. Table 2 shows the maximum drain current I_{ON} obtained with each tunnel barrier variation and Table 3 shows this work ensures high drain current compared with other references.

DOI: https://doi.org/10.26799/cp-nanotechfrance2018

The charge-voltage characteristics illustrate staircase pattern indicating periodic CB oscillations as shown in Fig. 5

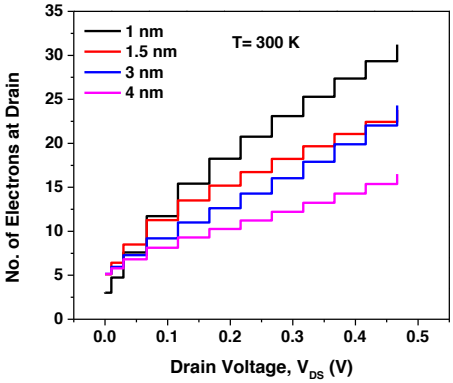

Fig. 5: Charge-Voltage Characteristics.

Table 4 Extracted Parameters

Tj (nm)	V_{CB} (mV)	E (meV)
1	18.39	42.2
1.5	27.54	37.6
3	23.44	39.7
4	40.80	31.0

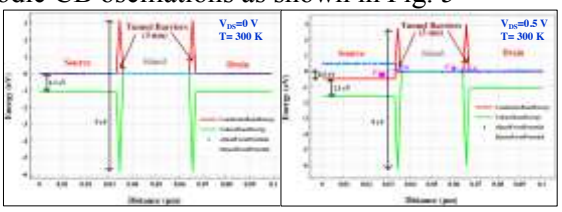

Fig. 6 Energy Band Diagram for CB and QMT

With increasing drain voltage, more and more number electrons (fixed for a particular CB interval) are transported from source to drain through the island. It is observed that step-size of the staircase pattern increases monotonically with reduction in tunnel barrier thickness. V_{CB} can be extracted as inverse derivative of the charge-voltage profile. ΔE due to tunneling of single electron can also be calculated from this profile. Table 4 shows the simulated V_{CB} and ΔE for the devices under consideration, at room temperature. Fig. 6 shows the energy band diagram of 3 nm tunnel barrier structure with V_{DS}=0 V where tunneling is prohibited and V_{DS}= 0.5 V where CB is overcome at room temperature.

5. Conclusion

CB, which is a signature mechanism of SET, usually manifests itself at low temperatures. However, for mass production of hybrid SETMOS circuits, room temperature operation of SET is must. In this work, tunnel barrier is engineered on SOI wafer so that the device qualifies for controlled CB and QMT at room temperature. It is observed that SiO_2 barrier of 3 nm and 4 nm thickness exhibits significant CB of 23.44 mV and 40.80 mV with tunneling current of 0.072 µA and 0.00715 µA, respectively. The process compatibility and device simulation results persuade hybrid SETMOS logic and memory circuits for ultra-low power and low voltage applications. The influence of the gate voltage on the behaviour of the device at room temperature will be targeted in future.

References

1. K. Likharev, "Single-electron transistors: Electrostatic analogs of the DC SQUIDS," in *IEEE Transactions on Magnetics*, vol. 23, no. 2, pp. 1142-1145, March 1987.
2. R. Parekh, A. Beaumont, J. Beauvais and D. Drouin, "Simulation and Design Methodology for Hybrid SET-CMOS Integrated Logic at 22-nm Room-Temperature Operation," in *IEEE Transactions on Electron Devices*, vol. 59, no. 4, pp. 918-923, April 2012.
3. S. Mahapatra, V. Vaish, C. Wasshuber, K. Banerjee and A. M. Ionescu, "Analytical modeling of single electron transistor for hybrid CMOS-SET analog IC design," in *IEEE Transactions on Electron Devices*, vol. 51, no. 11, pp. 1772-1782, Nov. 2004.
4. K.-C. Kang, J.-E. Lee, J.-H. Lee, J.-H. Lee, H. Shin and B.-G. Park, "Poly-silicon quantum-dot single-electron transistors," *Journal of the Korean Physical Society*, vol. 60, no. 1, pp. 108–112, 2012, doi: 10.3938/jkps.60.108.
5. Y. Sun, Rusli and N. Singh, "Room-Temperature Operation of Silicon Single-Electron Transistor Fabricated Using Optical Lithography," in *IEEE Transactions on Nanotechnology*, vol. 10, no. 1, pp. 96-98, Jan. 2011.
6. V. Ray, R. Subramanian, P. Bhadrachalam, L.-C. Ma, C.-U. Kim, and S. J.Koh, "Cmos-compatible fabrication of room-temperature single-electron devices," *Nature nanotechnology*, vol. 3, no. 10, pp. 603–608, 2008.
7. K. G. El Hajjam *et al*., "Tunnel Junction Engineering for Optimized Metallic Single-Electron Transistor," in *IEEE Transactions on Electron Devices*, vol. 62, no. 9, pp. 2998-3003, Sept. 2015.
8. C. Hamaguchi, *Basic semiconductor physics*. Springer Science & Business Media, 2009.
9. H. Ilatikhameneh, T. A. Ameen, G. Klimeck, J. Appenzeller and R. Rahman, "Dielectric Engineered Tunnel Field-Effect Transistor," in *IEEE Electron Device Letters*, vol. 36, no. 10, pp. 1097-1100, Oct. 2015.
10. Sentaurus Device User Guide

Proceedings of the Nanotech France 2018 International Conference (Nanotech France 2018)
Paris, France, June 27 - 29, 2018
DOI: https://doi.org/10.26799/cp-nanotechfrance2018

Nanoformulations of encapsulating Essential Oil in polymeric nanocarriers with antioxidant and antibacterial properties

Amro Shetta[1], James Kegere [2], Wael Mamdouh,[3]*

[1]The American University in Cairo (AUC), Department of Chemistry, School of Sciences and Engineering, Cairo, Egypt, amrpharma@aucegypt.edu

[2]The American University in Cairo (AUC), Department of Chemistry, School of Sciences and Engineering, Cairo, Egypt, kegerejames@aucegypt.edu

[3]The American University in Cairo (AUC), Department of Chemistry, School of Sciences and Engineering, Cairo, Egypt, wael_mamdouh@aucegypt.edu

Abstract

Chitosan (CS) nano-carrier was used as an encapsulating agent for Peppermint Essential Oil (PO) by using two-steps method starting with emulsification and followed by ionic cross-linking method. The PO loaded chitosan colloidal nanoparticles were characterized by different techniques; Dynamic light scattering (DLS), Fourier transform infrared (FT-IR) spectroscopy, Thermogravimetric analysis (TGA), and powder X-ray diffraction (XRD). The morphology and size of CS/PO NPs were detected by Transmission electron microscopy (TEM) that showed spherical shape of the nanoparticles with an average size range below 100 nm. The EE % and LC % of CS/PO NPs reached 82% and 22%, respectively. Moreover, the PO nano-encapsulation improved the PO antioxidant activity by about 2 folds and showed superior antibacterial activity of CS/PO NPs against *Staphylococcus aureus* and *Escherichia coli* by about 99.9% and 97.5%, respectively. The results obtained will enhance the usage of nano-encapsulated PO in the Food and Pharmaceutical sectors.

Keywords: Chitosan; Peppermint oil (PO); Nanoparticles; Thermal stability; Antioxidant activity; Antibacterial activity

1. Introduction

Peppermint oil (PO) is an example of essential oil (EO) that is obtained by steam distillation of peppermint *(Mentha piperita)* leaves of *Labiatae* herbs family [1]. The biomedical activities of PO are mainly due to the presence of Menthone and Menthol [2]. Despite the huge potential of using EOs in different sectors specially in food industry [3], however,there are a few drawbacks of using pure EOs such as: high volatility and high thermal degradation. Chitosan (CS) is a polysacharide that is naturaly drived from chitin after deacetylation reaction [4]. Chitosan has been receiving a significant interest in the biomecial sector, especially encapsulation studies where CS is used as the main carrier. The interesting findings of the different CS/EOs encapsulation studies were mainly highlighing the significant improvement in the activities of the encapsulated EOs versus their bulk counterparts.

The aim of the present work is to encapsulate PO in CS NPs via emulsionfication and ionic cross linking with sodium tripolyphostphate (TPP) as represent in Figure (1). The following formula were prepared with (CS: PO) weight ratios of (1:0.25, 1:0.50, 1:0.75 and 1:1.00 w/w). The encapsulation process was investigated by through different characterization techniques. The antioxidant activity of PO before and after encapsulation was evaluated by 2,2-diphenyl-1-picrylhydrazyl radical (DPPH). Finally, to study the antibacterial activity of pure and encapsulated PO against *Staphylococcus aureus* and *Escherichia coli*, agar dilution and colony counting method were used.

Proceedings of the Nanotech France 2018 International Conference (Nanotech France 2018)
Paris, France, June 27 - 29, 2018
DOI: https://doi.org/10.26799/cp-nanotechfrance2018

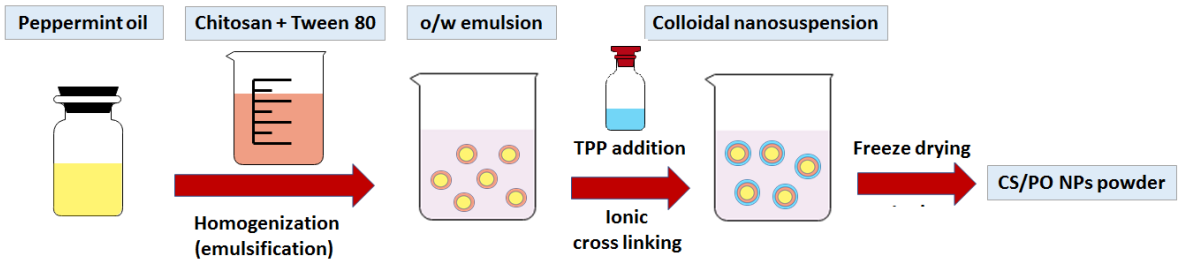

Fig. 1. Schematic representation of the emulsification ionic gelation method.

2. Results and discussion

2.1. Characterization of NPs, EE% and LC%.

DLS measurements (table 1) showed an average diameter of 217.2 nm for CS NPs while CS/PO NPs showed an average diameter ranged between 226.3 - 249.7 nm. It showed be pointed out that the maximum NPs size appeared for CS/PO NPs (1:0.75 w/w). Results showed a significant increase in the average diameter of NPs as a function of initial PO content which are in a good agreement with the findings of Hosseini et al.[5].

Table 1: Encapsulation efficiency (EE) and loading capacity (LC) of PO, and Z-average diameter of CS NPs and CS/PO NPs.

CS: PO (w/w)	Z-average diameter (nm)	EE %	LC %
1:0.00	217.2 ± 6.42	0	0
1:0.25	231.4 ± 12.72	82.1 ±7.5	8.15 ±0.7
1:0.50	249.7± 2.78	79.4 ± 4.1	13.1 ± 0.7
1:0.75	252.6± 3.48	76.7 ± 1.3	17.6 ±0.5
1:1.00	238.9 ± 9.56	78.4 ± 1.9	22.2 ± 0.5

Results were reported as mean ± SD, $n = 3$.

UV-vis spectroscopy was used to estimate the EE% and LC%. CS/PO NPs. As represented in (Table 1), Encapsulation efficiency (EE%) values ranged from 76.7-82.1%. The results showed an increase in EE% as a function of the PO content. In the same way, the loading capacity (LC%) values ranged from 8.15-22.2%. The results indicated that LC% increased as a function of initial PO content. The EE% and LC% findings were found to be in agreement with the findings of Keawchaoon and Yoksan [6].

FTIR spectra of CS NP showed characteristic peak of hydroxyl chemical group that appeared at 3433 cm^{-1}, Sp^3 C-H stretching appeared at 2933 cm^{-1} and amide stretching peaks appeared at 1642 and 1550 cm^{-1} (Fig. 2(a)). Pure PO spectra showed sharp characteristic peaks at 1710 cm^{-1} due to carbonyl stretching (Fig. 2(b)). The spectra of CS/PO NPs (Fig. 2(c-f)) showed all the characteristic peaks of CS and PO with significant enhancement in intensity of carbonyl stretching peak as a function of PO content. It should be pointed out that all carbonyl peaks stretching peak of encapsulated PO were shifted from 1710 cm^{-1} to 1731 cm^{-1}. The results of FTIR analysis identified the encapsulation of PO in the CS NPs.

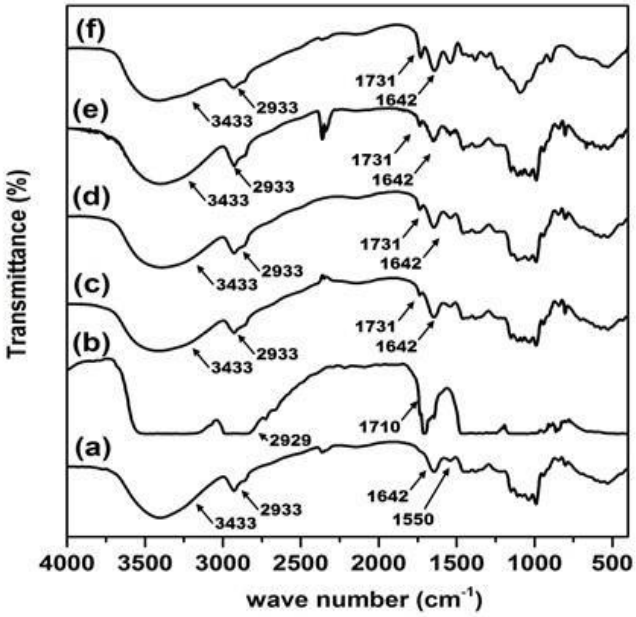

Fig. 2. FT-IR of CS NP(a), pure PO (b) and CS/PO NPs (c-f) prepared using different initial weight ratios of CS: PO: (c) 1:0.25, (d) 1:0.50, (e) 1:0.75 and (f) 1:1.00 w/w

2.2. Evaluation of the antioxidant activity of PO, CS and CS/PO NPs

According to (Fig. 3), DPPH radical scavenging ability was identified for predetermined CS/PO NPs and the corresponding PO and CS NPs amounts. CS NPs have antioxidant activity that ranges between 9.3 to 21.13% for concentration ranges between 6 to 48 mg/mL respectively. On the other hand, both CS/PO NPs and corresponding amounts of pure PO (range between 0.4 – 3.5 mg/mL) show a concentration-dependent antioxidant activity and were in the range of 24.4 - 71.4 and 13 to 52.3%, respectively. It is important to note that the limited antioxidant activity of CS/NPs was found to be in agreement with the findings of Chen et al.,[7]. The reason behind that might be related to the CS, TPP cross-linking which masks the CS amino groups responsible for the reaction with DPPH molecules. Surprisingly, the antioxidant activity of encapsulated PO was significantly higher than free PO by 2 folds. However, the antioxidant activity of PO was not significantly higher than CS NPs.

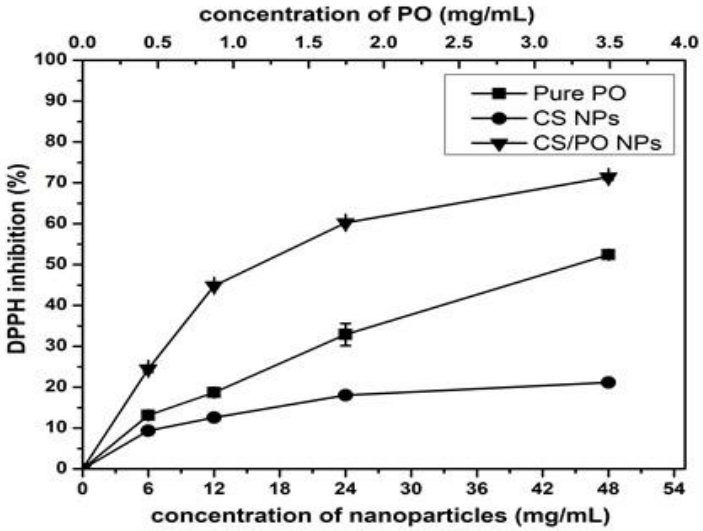

Fig. 3. DPPH inhibition (%) of pure PO, CS NPs and CS/PO NPs.

DOI: https://doi.org/10.26799/cp-nanotechfrance2018

2.3. Evaluation of the antibacterial activity of CS/PO NPs

As represented in Table (2), pure PO showed antibacterial activities of 60.2±6.12 % and 94.53± 0.53% against *S. aureus* and *E.coli*, respectively. Pure PO antibacterial activities rely on the penetration of phytochemical components through the phospholipid of cell membrane, the coagulation of cell contents, and the damage of proteins and lipids [8]–[10]. Surprisingly, encapsulated PO showed a significant enhancement of bactericidal activity by about 39.63% and 3.01% against *S. aureus* and *E.coli*, respectively. Therefore, the nano-encapsulation of both bulk EOs was a magical solution for enhancing the antimicrobial potential. These results agree with the findings [11] that showed an enhancement of the antibacterial activity of encapsulated Carum copticum essential oil (CEO) over pure CEO by 1.16 folds. The reason behind the enhancement of bactericidal activity of encapsulated oils might be related to the antibacterial activity of CS NPs themselves that showed bactericidal activity against *S. aureus* and *E.coli* by about 99.1 ± 0.23% and 99.2 ± 0.68%, respectively. CS NPs antimicrobial activity might be due to ionic interaction between the positive charge on CS and the anionic surface of bacteria.

Table 2. % inhibition of bacterial growth

Samples	*S. aureus*	*E. coli*
PO	60.20 ± 6.12 %	94.53 ± 0.53%
CS NPs	99.10 ± 0.23%	99.20 ± 0.68%
CS/PO NPs (1:1.00 w/w)	99.90 ± 0.01%	97.54 ± 0.52%

Results were reported as mean ± SD, $n = 3$.

3. Conclusion

The encapsulation of PO in CS NPs was successful, as confirmed by DLS, FTIR, TEM, TGA, XRD and UV-vis spectroscopy. CS/PO NPs showed a spherical shape with size range of 20-90 nm. The EE% and LC% of CS/PO NPs were about 78-82% and 8-22%, respectively when the initial PO amount was (0.25–1.00 w/w of CS). DPPH assay showed an enhancement in the antioxidant activity of encapsulated PO by about 2 folds. The CS-TPP system showed an ability to preserve the PO TPC. Finally, encapsulated PO showed an enhancement in the antibacterial activity by about 39.63% and 3% against *S. aureus* and *E.coli*, respectively. The previous findings potentiate the usage CS/PO NPs in the Food and Pharmaceutical industries. Further research might be necessary to determine the stability of the PO properties after encapsulation process with CS NPs under different conditions. For examples, other essential oils (EOs) could be used following the same protocols. In addition, different strains of bacteria could also be investigated. Moreover, different forms of PO such as nanofibers instead of NPs forms could be fabricated to investigate the influence of the nanostructures on the final antioxidant and antibacterial activities.

Acknowledgements

We thank Professor Rania Siam for kindly providing S. aureus and E.coli strains. The authors acknowledge the financial support received from the American University in Cairo (AUC) through student and Faculty Support Research Grants.

References

[1] I. Găinar, R. Vîlcu, and M. Mocan, "Supercritical fluid extraction and fractional separation of essential oils," 2002.

[2] W. Dhifi, N. Jelali, W. Mnif, M. Litaiem, and N. Hamdi, "Chemical Composition of the Essential Oil of Mentha Spicata L. from Tunisia and Its Biological Activities," *J. Food Biochem.*, vol. 37, no. 3, pp. 362–368, Jun. 2013.

[3] M. Hyldgaard, T. Mygind, and R. L. Meyer, "Essential Oils in Food Preservation: Mode of Action, Synergies, and Interactions with Food Matrix Components," *Front. Microbiol.*, vol. 3, 2012.

[4] L. Qi, Z. Xu, X. Jiang, C. Hu, and X. Zou, "Preparation and antibacterial activity of chitosan nanoparticles," *Carbohydr. Res.*, vol. 339, no. 16, pp. 2693–2700, 2004.

[5] S. F. Hosseini, M. Zandi, M. Rezaei, and F. Farahmandghavi, "Two-step method for encapsulation of oregano essential oil in chitosan nanoparticles: Preparation, characterization and in vitro release study," *Carbohydr. Polym.*, vol. 95, no. 1, pp. 50–56, Jun. 2013.

[6] L. Keawchaoon and R. Yoksan, "Preparation, characterization and in vitro release study of carvacrol-loaded chitosan nanoparticles," *Colloids Surf. B Biointerfaces*, vol. 84, no. 1, pp. 163–171, May 2011.

[7] F. Chen, Z. Shi, K. g. Neoh, and E. t. Kang, "Antioxidant and antibacterial activities of eugenol and carvacrol-grafted chitosan nanoparticles," *Biotechnol. Bioeng.*, vol. 104, no. 1, pp. 30–39, Sep. 2009.

[8] B. C. Andoğan, H. Baydar, S. Kaya, M. Demirci, D. Özbaşar, and E. Mumcu, "Antimicrobial activity and chemical composition of some essential oils," *Arch. Pharm. Res.*, vol. 25, no. 6, pp. 860–864, 2002.

[9] J. R. Calo, P. G. Crandall, C. A. O'Bryan, and S. C. Ricke, "Essential oils as antimicrobials in food systems – A review," *Food Control*, vol. 54, pp. 111–119, Aug. 2015.

[10] M. N. Gallucci *et al.*, "Antimicrobial combined action of terpenes against the food-borne microorganisms Escherichia coli, Staphylococcus aureus and Bacillus cereus," *Flavour Fragr. J.*, vol. 24, no. 6, pp. 348–354, 2009.

[11] A. Esmaeili and A. Asgari, "In vitro release and biological activities of Carum copticum essential oil (CEO) loaded chitosan nanoparticles," *Int. J. Biol. Macromol.*, vol. 81, pp. 283–290, Nov. 2015.

Proceedings of the Nanotech France 2018 International Conference (Nanotech France 2018)
Paris, France, June 27 - 29, 2018
DOI: https://doi.org/10.26799/cp-nanotechfrance2018

Environmental Impact Assessment of Triboelectric Nanogenerator Materials for Energy Harvesting

M. A. Parvez Mahmud[1], Nazmul Huda[1], Shahjadi Hisan Farjana[1], and Candace Lang[1]
[1]School of Engineering, Macquarie University
Sydney, NSW 2109, Australia
m-a-parvez.mahmud@mq.edu.au, nazmul.huda@ mq.edu.au,
shahjadi-hisan.farjana@mq.edu.au, candace.lang@mq.edu.au

Abstract
Triboelectric materials are widely been utilized to produce electricity, harvesting ambient mechanical energy through movement for sectors and products, from sensors, to biomedical devices, to small portable electronics. Polyethylene terephthalate (PET) and Polymethyl methacrylate (PMMA) lead the market among hundreds of triboelectric polymers to create an autonomous energy supply. Recently emphasis has been given to research on both polymers due to their increasing popularity in triboelectric nanogenerator applications to build self-powered electronics replacing conventional batteries. The production steps of both materials from raw resources are hazardous to the atmosphere in terms of toxicity and human-health effects. However, no quantification of the possible environmental impacts for the manufacturing of PET and PMMA exists. This research paper addresses their comparative environmental effects, in terms of pollutant emissions during manufacturing from raw materials. A comprehensive Life Cycle Inventory (LCI) model is developed for step-by-step systematic evaluation of their environmental impacts. Life Cycle Assessment (LCA) has been carried out by the Impact 2002+ Endpoint, Raw material flows, Eco-indicator 99, IPCC and CED methods, using the Ecoinvent database and SimaPro software. The impacts are considered in 21 categories such as global warming, acidification, eutrophication, terrestrial ecotoxicity, human toxicity, human carcinogenic toxicity, and fine particulate matter formation, marine ecotoxicity etc. The results reveal that there is a more significant environmental impact caused by PET than with PMMA polymer during the manufacturing process. The reason behind these impacts is the amount of toxic chemical elements present as constituents of the PET raw material and its production steps. It can be recommended that a superior environmental performance can be obtained through optimization, especially by carefully selecting substitute elements and machines, taking consideration of the toxicity aspects, and by reducing the impacts associated with designs, production methods and practice.

Keywords: Nanogenerator, polyethylene terephthalate, polymethyl methacrylate, life-cycle assessment, environmental impact, energy harvesting.

1. Introduction

Nowadays triboelectric polymers are getting popular for building triboelectric nanogenerators to manufacture self-powered electronics and sensors [1]. Among many triboelectric materials Polyethylene terephthalate (PET) and Polymethyl methacrylate (PMMA) are widely been used for their better triboelectric properties and enhanced quality [2]. However, assessment of their impacts to human health, ecosystem and resources during the production and waste management steps is essential and yet to be done. Therefore, this research is aimed to do a life-cycle assessment (LCA) based systematic analysis for evaluating and comparing the hazardous emissions of both PMMA and PET. A life-cycle inventory (LCI) is developed for both cases considering all inputs and outputs of the productions plants using Ecoinvent database, which is a global and renowned dataset. The total environmental impacts are assessed and compared by several methods such as: Impact 2002+, IPCC and CED, using SimaPro software [3-4]. Both 'cradle-to-gate' and 'cradle-to-grave' schemes are utilized to assess and compare the impacts within the definite life cycle inventory.

The LCA of triboelectric polymers which have been accomplished by researchers until now are mostly emphasized on the GHG emission evaluations. None of the previous LCA research [2, 5] assessed the ecological effects of PMMA and PET polymer production plants. Furthermore, no work is done that comprehensively considers the ecological effects caused by the total life time of these polymer production plants. This research helps to seal this research gap by accomplishing a systematics LCA of PMMA and PET production technologies following ISO 14040-14043 standards [6]. This work therefore is a pioneer and an inclusive impact evaluation of PMMA and PET polymers through

DOI: https://doi.org/10.26799/cp-nanotechfrance2018

systematic LCA method considering their raw material and energy inputs, and hazardous emission and solid waste outputs during the fabrication stages. The effects are assessed and compared for sixteen impact assessing categories. The findings show that PMMA has a superior performance for maximum considered impact categories than PET. Furthermore, the results by the IPCC and CED approaches indicate that the hazardous greenhouse gas emissions and energy consumption rates of PMMA manufacturing plants is lower for PMMA than for PET. In Section 2, research methodology is described. Section 3 highlights the life-cycle analysis results under the ecological effect indicators, using the Impact 2002+, CED and IPCC approaches, thus recommends the environmental-impact reduction ways for the considered processes.

2. Methodology

Life-cycle impact assessment process involves data collection from the Ecoinvent database for all energy and resource-based inputs during raw material processing, manufacturing, polymer production, transportation, and end-of-life disposals. It also considers the airborne emissions, recyclable waste, land filled waste and dumping during LCA of triboelectric materials and devices. There are four key common elements of a life-cycle assessment such as: goal and scope definition, inventory analysis, impact assessment, and life-cycle interpretation, which follow the international standards ISO 14040, 14041, 14042 and 14043, respectively. The impacts are assessed by Impact 2002+, CED and IPCC methods using SimaPro software. A life-cycle inventory (LCI) is developed for both PMMA and PET production plants considering all inputs and outputs to assess their impacts. Several sustainability matrices are utilized in this regard. The functional unit is considered as 1 m^2. The impacts under carcinogens, non-carcinogens, ionizing radiation, ozone layer depletion, aquatic ecotoxicity, respiratory inorganics, terrestrial ecotoxicity, land occupation, global warming, and non-renewable energy usage categories are assessed and compared by Impact 2002+ methodology for both types of considered triboelectric materials. Moreover, the IPCC and CED methods are used to assess and compare the gas-based emissions and energy consumption rates for during the production of both types of polymers.

3. Results and Discussion

The effects of PMMA and PET polymers during the production of 1 m^2 size are obtained by renowned Impact 2002+ approach utilizing the ecoinvent dataset. Figures 1 depict the comparative effects caused during the production of 1 m^2 of PET and PMMA. The outcome highlight that PMMA is lower impactful than PET for most of the effect measuring categories such as: carcinogens, ionizing radiation, ozone layer depletion, aquatic ecotoxicity, terrestrial ecotoxicity, land occupation, global warming, non-renewable energy usage. Clearly, Impact 2002+ approach highlights that PMMA is more environmentally-friendly than PET production plants. The cause behind getting higher amount effects is the rate of toxic chemicals present as elements of PET raw materials. The impacts can be abated by choosing quality raw ingredients and environmentally superior machineries at various manufacturing stages.

The rate of energy consumption comparison of the PMMA and PET fabrication processes, using CED method is showed at Figure 2. Among several categories fossil fuels-oil, fossil fuels-gas, renewables, biomass, nuclear, and embodied energy consumption rates are higher in PMMA than PET. But fossil fuels-coal based consumption is higher in PET manufacturing plants than PMMA. The comparative hazardous gas-based LCA outputs of the PET and PMMA productions in plant using IPCC approach is depicted in Figure 3. It is transparent from this figure that a low rate of nitrous oxide emitted with PMMA production technologies, and this type of plant is better in terms of environment than the PET polymer manufacturing plants.

DOI: https://doi.org/10.26799/cp-nanotechfrance2018

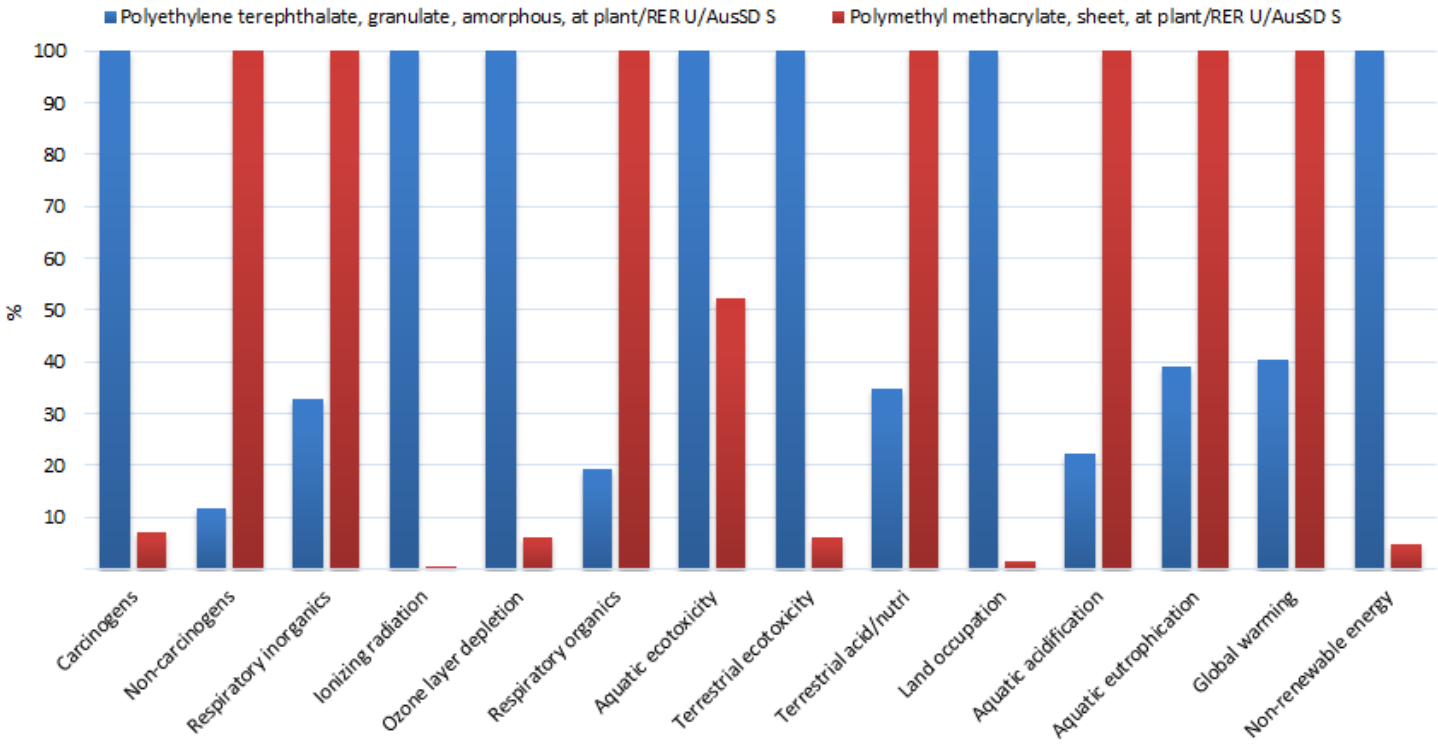

Fig. 1. Comparative life-cycle impact assessment outputs of the PMMA and PET fabrication processes using Impact 2002+ method.

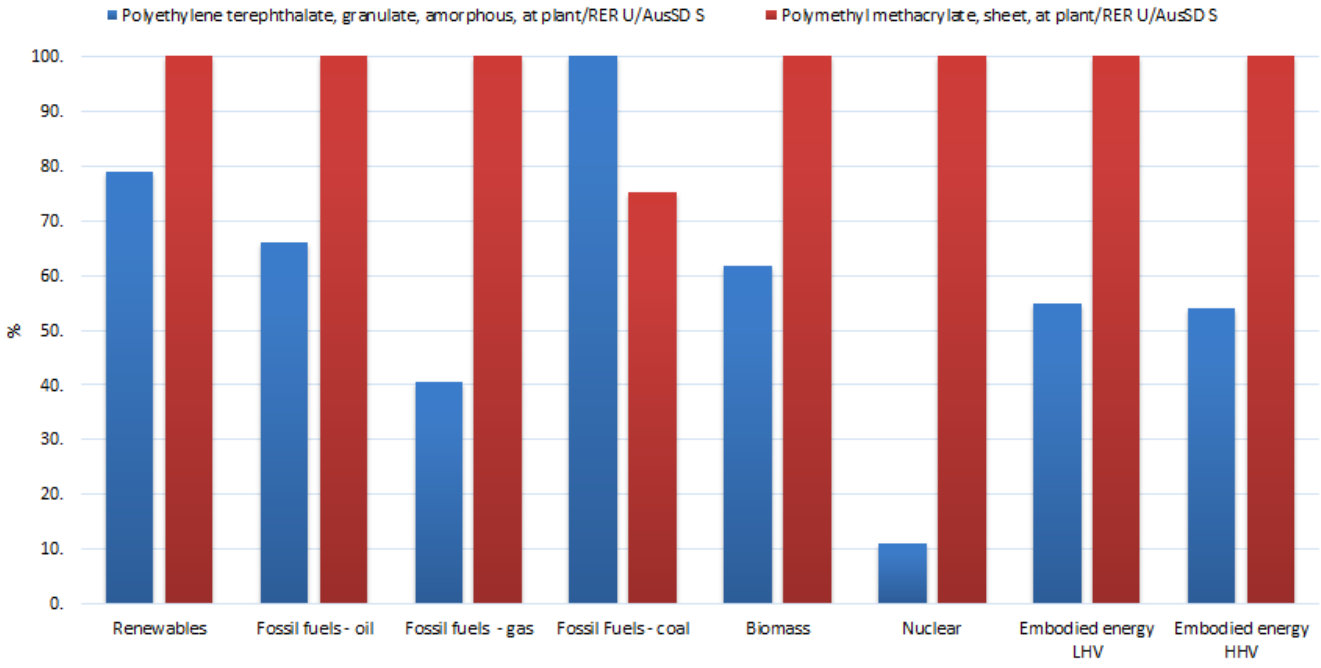

Fig 2. Energy consumption comparison of the PMMA and PET fabrication processes, using CED method.

DOI: https://doi.org/10.26799/cp-nanotechfrance2018

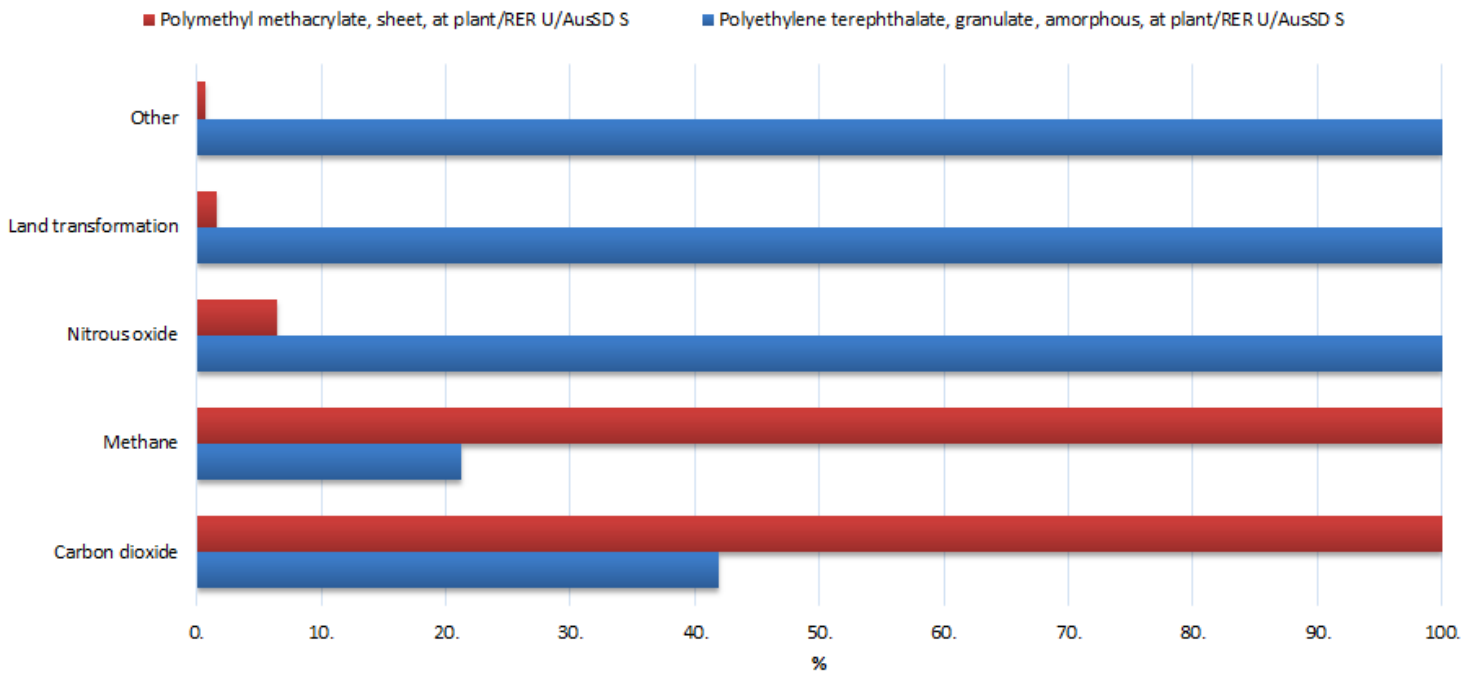

Fig 3. Comparative hazardous gas-based LCA outputs of the PMMA and PET fabrication processes in plant using IPCC method.

4. Conclusion

Triboelectric materials like PMMA and PET are widely been used to develop triboelectric nanogenerator for building self-powered portable electronics. The superior environmental performance of the nanogenerators depends on the environmentally-friendly production of PMMA and PET. This paper focuses the comparative impacts of PMMA and PET through life-cycle assessment by the Impact 2002+, CED and IPCC methods, utilising the ecoinvent database and SimaPro software. The results show that PMMA polymer fabrication plants emit lower GHG, CO_2, NOx and SOx compared to PET manufacturing plants. Moreover, impacts like global warming, ozone formation, acidification, ecotoxicity, and ionizing radiation rates are lower in PMMA polymer plants than for PET. The cause for these outcomes is the amount of hazardous chemicals associated in PET production processes. Therefore, PMMA is an environmentally superior triboelectric material than PET. It is recommended that careful selection of ingredients and machines during the manufacturing of triboelectric polymers can abate associated toxic gas emissions.

References

[1] Te-Chien Houa, Ya Yanga, Hulin Zhanga, Jun Chena, Lih-Juann Chenb, and Zhong Lin Wang, "Triboelectric nanogenerator built inside shoe insole for harvesting walking energy," Rapid Communication, vol. Nano Energy, 2013, vol. 2, pp. 856–862.
[2] Azapagic A, Emsley A, Hamerton I. Design for the environment: the life cycle approach in polymers. In: Hamerton Ian, editor. Polymers: the environment and sustainable development. NY: Wiley & Sons; 2003, vol. 53, pp. 125–131.
[3] PRe. Simapro. 7.18 ed. Amersfoort, The Netherlands; 2008.
[4] Jolliet O, Margni M, Charles R, Humbert S, Payet J, Rebitzer G, et al. IMPACT 2002+: a new life cycle impact assessment methodology. International Journal of LCA, 2003, vol. 8(6), pp. 324–330.
[5] Lee S, Xu X. Design for the environment: life cycle assessment and sustainable packaging issues. International Journal of Environmental Technology and Management 2005, vol. 5(1), pp. 14–41.
[6] M. Finkbeiner, A. Inaba, R. Tan, K. Christiansen, and H.-J. Kluppel, "The new international standards for life cycle assessment: ISO 14040 and ISO 14044," Int J LCA, 2006, vol. 11, pp. 80–85.

Proceedings of the Nanotech France 2018 International Conference (Nanotech France 2018)
Paris, France, June 27 - 29, 2018
DOI: https://doi.org/10.26799/cp-nanotechfrance2018

Synthesis of Polysulfone/Carbon Nanotubes-Polyamide Thin Film Nano-composite Membranes for Forward Osmosis Applications

Ahmed O. Rashed[1], Amal M.K. Esawi[2], Adham R. Ramadan[3]

[1]Department of Chemistry, The American University in Cairo
AUC Avenue, New Cairo, Egypt, ahmed.omia@aucegypt.edu
[2]Department of Mechanical Engineering, The American University in Cairo
AUC Avenue, New Cairo, Egypt, a_esawi@aucegypt.edu
[3]Department of Chemistry, The American University in Cairo
AUC Avenue, New Cairo, Egypt, aramadan@aucegypt.edu

Abstract
Forward osmosis (FO) is gaining potential as a promising alternative to reverse osmosis (RO) in membrane-based water desalination applications. FO water flux, salt rejection and reverse solute flux are three critical parameters affecting membrane performance. In the current study, functionalized multiwalled carbon nanotubes (F-MWCNTs) - polyamide (PA) thin film nano-composite (TFNC) membranes were synthesized on top of polysulfone (PSF) porous support layers by interfacial polymerization (IP) using m-phenylenediamine (MPD) in water and trimesoyl chloride (TMC) in hexane. The PSF support layer was synthesized by phase inversion in a water bath of a casting solution of PSF and polvinylpyrrolidone (PVP) dissolved in anhydrous dimethyl formamide (DMF). Multiwalled carbon nanotubes were functinoalized by oxidation, and then incorporated in the MPD aqueous solution during IP. The amount of F-MWCNTs was varied to study their effect on the membrane morphology and performance. The obtained membranes were characterized using Scanning Electron Microscopy (SEM), Atomic Force Microscopy (AFM), Fourier Transform Infrared Spectrophotometry (FTIR) and Brunauer-Emmett-Teller surface analysis (BET). FO performance was investigated using deionized water as the feed solution and 2M NaCl as the draw solution. It was found that F-MWCNTs enhanced the membrane hydrophilicity and surface roughness. This in turn led to increased FO water flux. The membrane with 0.01 wt/vol% F-MWCNTs showed the highest salt rejection (90.1%) with a FO water flux of 50.23 L/m^2 h and a reverse solute flux of 2.76 g/m^{2}h, thus outperforming thin film composite FO membranes reported in literature. Incorporating F-MWCNTs in the rejection layer of thin film composite membranes presents a promising approach for improving FO membranes performance.

Keywords: Forward osmosis, polysulfone, polyamide, carbon nanotubes, interfacial polymerization, thin film composite membranes.

1. Introduction

The physical phenomenon of forward osmosis (FO) is a spontaneous process that involves the movement of water molecules across a semipermeable membrane from a low osmotic pressure side to a high osmotic pressure side [1][2]. Basically, the difference in osmotic pressure is the driving force across the membrane [3]. FO does not need external pressure, a fact that makes it attractive in different applications [4]. There are multiple membrane types that can be used in FO. Thin film composite (TFC) membranes have been widely used in FO process. An ideal TFC FO membrane should be designed with a porous support layer and a thin active rejection layer. The highly porous, less tortuous support layer with hydrophilic properties is required to minimize the internal concentration polarization (ICP) and to increase the water flux while the rejection layer is required to achieve high salt rejection and to minimize the reverse solute flux from the draw solution. Most TFC membranes have been synthesized with a polyamide rejection layer on top of a porous support layer. Nanoparticles have been added to the membrane layers for enhancing membrane performance [5][6][7][8]. Recently, multi-walled carbon nanotubes (MWCNTs) were used in the fabrication of FO membranes. They can be incorporated into the support layer or the rejection layer to enhance the mechanical strength and to improve membrane performance. However, MWCNTs suffer from low hydrophilicity that makes their dispersion in the polymer matrix challenging. This can be overcome by the functionalization of MWCNTs [9][10].

DOI: https://doi.org/10.26799/cp-nanotechfrance2018

2. Experimental

2.1. Materials

Polysulfone (molecular weight average Mn ~22,000 by MO, Sigma-Aldrich) was used as the polymer for the membrane support layer. Polyvinylpyrrolidone (PVP) powder (average molecular weight 360,000, Sigma-Aldrich) was used as a pore forming agent. Anhydrous dimethyl formamide (DMF) (density 0.944g/ml, purity = 99.8%, Sigma-Aldrich) was used as a solvent. Deionized water (MilliPore) was used as a non-solvent.
For the polyamide rejection layer, m-phenylenediamine (MPD) flakes (molecular weight 108.14 g/mol, purity = 99%, Sigma-Aldrich), and 1,3,5-benzenetricarbonyltrichloride (TMC) (molecular weight 265.48 g/mol, purity = 98%, Sigma-Aldrich) were used as reacting monomers. Deionized water (MilliPore) was used as a solvent for MPD. Hexane (density 0.672, purity > 98.5%, Sigma-Aldrich) was used as a solvent for TMC.
Elicarb MWCNTs (diameter of 10-12 nm, tens of microns in length and a density of 1.7-1.9 g/cm^3, manufactured by Thomas Swan, England) were used as nanofillers. H_2SO_4 (purity = 98%, Sigma-Aldrich) and HNO_3 (purity > 69%, Sigma-Aldrich) were used in the oxidation functionalization of MWCNTs.

2.2. Membrane Support layer preparation

Casting solution of 18 wt% PSF and 2 wt% PVP in DMF was stirred at 200 rpm until PSF and PVP were completely dissolved reaching a clear homogenous solution. The solution was then sonicated for 30 minutes and then left overnight to get rid of all air bubbles. Membrane casting was then carried out using an Elcometer 4040 automatic film applicator with a fixed speed rate of 90 mm/sec. The solution was spread over a glass substrate by a moving casting knife with height of 175 µm. The glass substrate was immersed in a deionized water bath at room temperature for 15 minutes. The resulting membrane was washed several times with deionized water to remove the excess DMF.

2.3. Thin Film Nanocomposite (TFNC) membrane preparation

The rejection layer was prepared by interfacial polymerization (IP) on top of the support layer to produce the thin film composite (TFC) membrane, and the F-MWCNTs were incorporated in the rejection layer to produce TFNC membrane. Different amounts of functionalized MWCNTs (0.01, 0.05, 0.1 and 0.2 g) were dispersed in aqueous solutions of 4 wt/vol% MPD. The dispersion was carried out by ultrasonication. The solution was then poured onto the PSF support membrane layer with excess solution drained off. The composition was then dried using hot air. This was followed by pouring 0.2 wt/vol% TMC/ hexane solution on the top surface of the PSF support with the MPD and F-MWCNTs. The mixture was left for 2.5 minutes for complete IP, followed by curing at 80 ^{o}C. This resulted in the formation of PA rejection layer with incorporated MWCNTs.

2.4. Characterization of the membrane morphology and porosity

Membrane morphology was imaged using Leo Supra 55 (ZEISS) Field Emission Scanning Electron Microscope (FESEM). Membranes were coated with gold using a sputter coater of current (15 mA) for 2 minutes. Membranes porosity and surface area were determined by N_2 adsorption using Micrometrics ASAP 2020 instrument.

2.5. Characterization of the membrane hydrophilicity and roughness

Drop Shape Analyzer (DSA 25) from Kruss, Germany, was used for water contact angle determination, and sessile drop method was used to measure the contact angle of the different membranes in order to evaluate the membranes hydrophilicity while Dimension 3100 Atomic Force Microscope (AFM) from Digital Instruments (Veeco Metrology Group), was used to measure the surface roughness of the synthesized membranes.

2.6. Determination of the membrane FO performance

FO water flux and reverse solute flux were measured using a Sterlitech CF042 FO test cell using FO mode with the rejection layer facing the feed solution. The feed (deionized water) and draw (2M NaCl) solutions were circulated at a rate of 220 ml/min in a closed loop using pumps. The salt rejection was measured using a Sterlitech HP4750 Stirred dead-end cell. FO water, reverse solute flux and salt rejection were measured using equations 1, 2 and 3 respectively.

$$J = \frac{\Delta V}{A\,\Delta t} \tag{1}$$

where J (L/m^{2}h) is the FO water flux, ΔV (L) is the draw solution volume change, A (m^2) is the active membrane area and Δt (h) is the time interval of the experiment.

DOI: https://doi.org/10.26799/cp-nanotechfrance2018

$$Js = \frac{\Delta C\, V}{A\, \Delta t} \quad (2)$$

where Js (g/m2h) is the reverse solute flux, ΔC (g/L) is the feed solution concentration change, V (L) is the feed solution volume at the end of the experiment, A (m2) is the active membrane area and Δt (h) is the time interval of the experiment.

$$R\% = 1 - \frac{Cp}{Cf} \times 100 \quad (3)$$

where *R%* is the salt rejection percent, *Cp* is the permeate concentration and *Cf is* the feed concentration.

3. Results

3.1. Membrane Morphology and Porosity

SEM top surface and cross-section images of the top performing TFNC 0.01% membrane are shown in Fig. 1. The presence of the F-MWCNTs within the PA rejection layer can be observed on the top surface of the membrane while the cross-section indicates the shows the PA rejection layer on top of the support membrane.

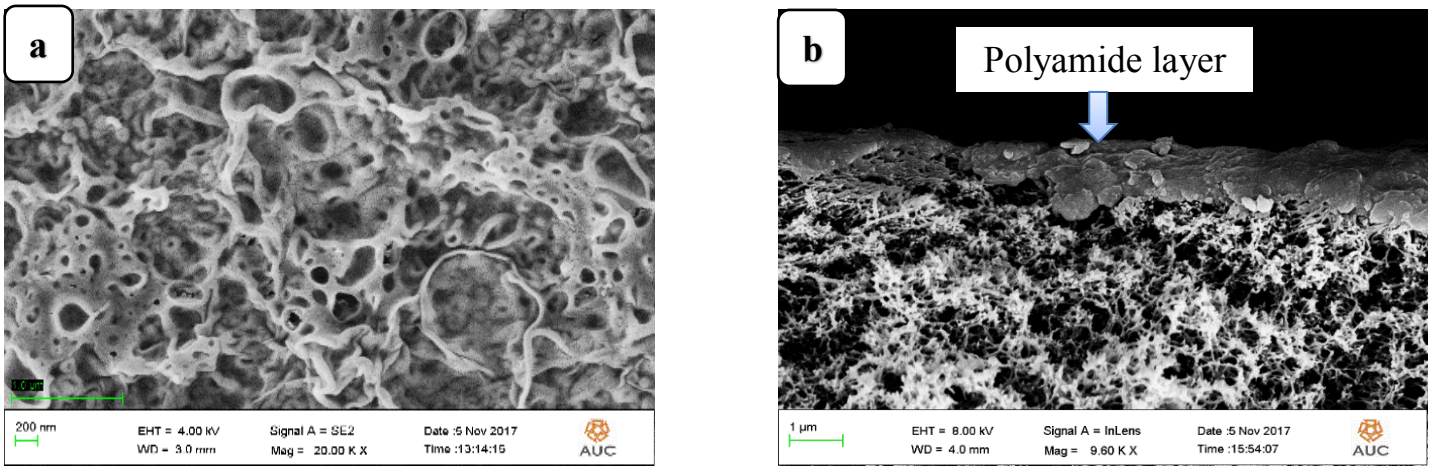

Fig. 1: SEM images of TFNC 0.01% including (a) Top surface, (b) Cross-section

Table 1 summarizes the BET surface area and average pore width for the different TFNC membranes and the blank membrane. It was found that the BET surface area generally increased with increasing F-MWCNT content while the variation of average pore width was observed to be less pronounced.

Table 1: BET surface area and the average pore width of TFNC membranes

Membrane	F-MWCNT wt/vol%	BET surface area (m^2/g)	Average pore width (nm)
Blank	0	18.07	8.43
TFNC 0.01%	0.01	20.62	7.58
TFNC 0.05%	0.05	21.88	8.01
TFNC 0.1%	0.1	20.10	8.45
TFNC 0.2%	0.2	21.69	8.41

3.2. Membrane hydrophilicity and surface roughness

Fig. 2 shows the correlation between the contact angle and FO water flux with increasing the concentration of F-MWCNTs. It was found that increasing F-MWCNTs concentration decreased the contact angle consistently from 62.15±0.43° for blank to 41.85±0.17° for TFNC 0.2%, reflecting the increase in membrane hydrophilicity. It is believed

DOI: https://doi.org/10.26799/cp-nanotechfrance2018

FO water flux increased due to the improved hydrophilicity that increased the attraction between the membrane surface and the water molecules, thus facilitating the flow of water molecules through the membrane surface. In addition, a correlation between surface roughness and FO water flux for the TFNC membranes and the blank is shown in Fig. 3, and it was found that increasing the F-MWCNTs increased the membrane surface roughness with associated increase in the FO water flux.

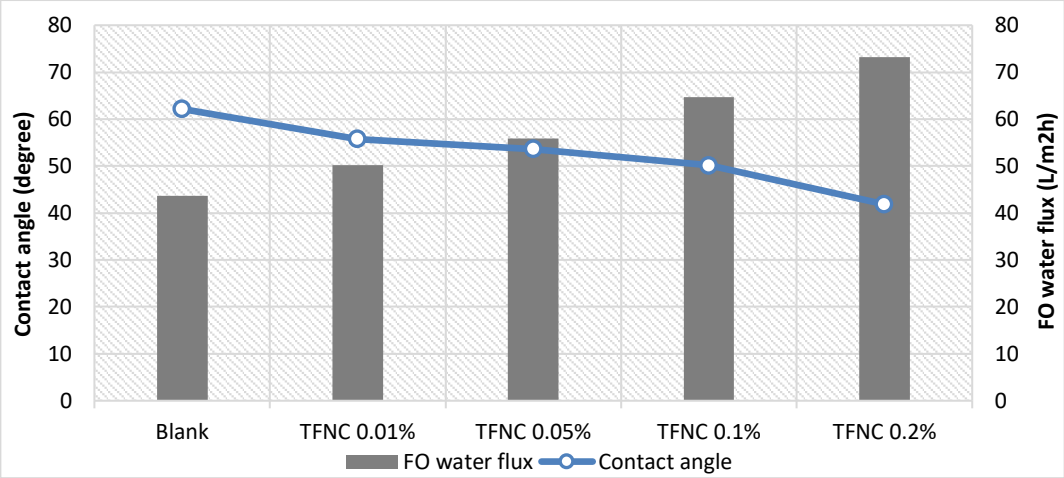

Fig. 2: Contact angle and FO water flux correlation for TFNC membranes and the blank

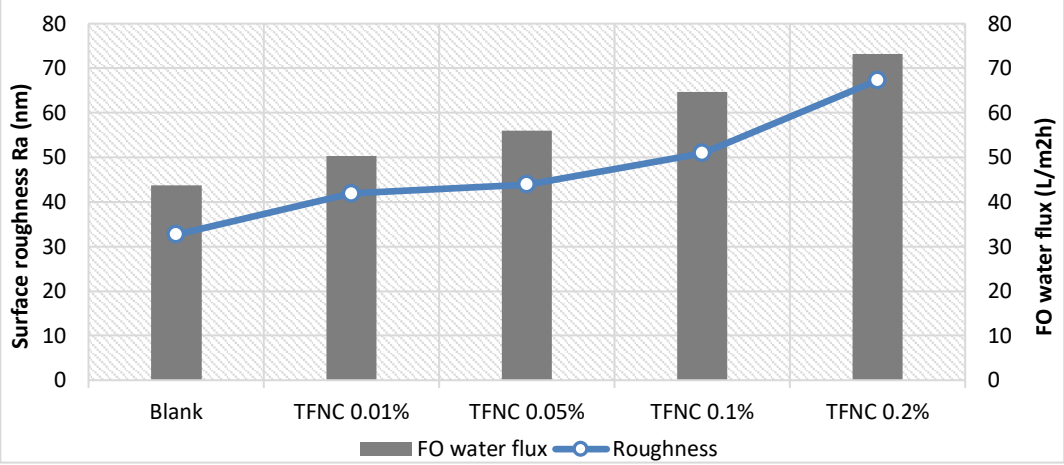

Fig. 3: Surface roughness and FO water flux correlation for TFNC membranes and the blank

3.3. Membrane FO performance

Table 2 presents the FO water flux, reverse solute flux and salt rejection of the blank and TFNC membranes with their different F-MWCNTs concentrations. Increasing the concentration of F-MWCNTs in the membrane rejection layer resulted in the increase in FO water flux from 43.7±0.51 L/m^{2}h for the blank to 73.15±2.66 L/m^{2}h for TFNC 0.2%. This is in accordance with the improved membrane hydrophilicity and surface roughness. On the other hand, the membranes salt rejections were not negatively impacted with the introduction of small amounts of F-MWCNTs. However, higher concentrations of F-MWCNTs (> 0.05 wt/vol) led to an observed decrease in salt rejection because of the possible agglomeration of F-MWCNTs that might interrupt interfacial polymerization, thus reducing polymer cross-linking in the rejection layer, with the result of a significant increase in porosity, which in turn negatively impacts salt rejection. In addition, the membranes reverse solute flux generally increased with increasing the concentration of F-MWCNTs in the rejection layer.

DOI: https://doi.org/10.26799/cp-nanotechfrance2018

Table 2: FO water flux, reverse solute flux and salt rejection of the blank and TFNC membranes

Membrane	FO water flux (L/m^2h)	Reverse solute flux (g/m^2h)	Salt rejection (%)
Blank	43.70±0.51	3.51±0.23	88.30±0.11
TFNC 0.01%	50.23±0.93	2.76±0.21	90.05±0.25
TFNC 0.05%	55.92±2.45	3.74±0.51	89.01±0.36
TFNC 0.1%	64.63±2.51	6.15±0.34	73.64±3.55
TFNC 0.2%	73.15±2.66	8.21±0.65	63.88±1.76

4. Conclusion

Thin Film Nano-Composite membranes (TFNC) were synthesized by the incorporation of carboxyl Functionalized Multi-Walled Carbon Nanotubes (F-MWCNTs) in a polyamide (PA) rejection layer on top of a polysulfone (PSF)/ polyvinylpyrrolidone (PVP) support layer in order to be used in Forward Osmosis (FO) applications including water desalination. The incorporation of carboxyl F-MWCNTs in the rejection layer was found to be effective in improving the FO water flux. This is believed to be associated with the observed increase in membrane hydrophilicity and increased surface roughness. On the other hand, salt rejection was not negatively affected by the presence of small amounts of F-MWCNTS (smaller than 0.1%), Larger amounts of F-MWCNTs led to agglomerations that might have interrupted interfacial polymerization, leading to the observed decrease in salt rejection.

Acknowledgments

I would like to thank The American University in Cairo (AUC) for funding my research studies. I also wish to thank Dr. Mohamed El-Morsi in Mechanical Engineering Department for his help with setting up the FO test cell.

References

1. W. J. Lau, A. F. Ismail, N. Misdan, and M. A. Kassim, “A recent progress in thin film composite membrane: A review,” *Desalination*, vol. 287, pp. 190–199, 2012.
2. S. Zhao, L. Zou, C. Y. Tang, and D. Mulcahy, “Recent developments in forward osmosis: Opportunities and challenges,” *J. Memb. Sci.*, vol. 396, pp. 1–21, 2012.
3. T. S. Chung, L. Luo, C. F. Wan, Y. Cui, and G. Amy, “What is next for forward osmosis (FO) and pressure retarded osmosis (PRO),” *Sep. Purif. Technol.*, vol. 156, pp. 856–860, 2015.
4. A. Subramani and J. G. Jacangelo, “Emerging desalination technologies for water treatment: A critical review,” *Water Res.*, vol. 75, pp. 164–187, 2015.
5. T. Y. Cath, A. E. Childress, and M. Elimelech, “Forward osmosis: Principles, applications, and recent developments,” *J. Memb. Sci.*, vol. 281, no. 1–2, pp. 70–87, 2006.
6. N. Akther, A. Sodiq, A. Giwa, S. Daer, H. A. Arafat, and S. W. Hasan, “Recent advancements in forward osmosis desalination: A review,” *Chem. Eng. J.*, vol. 281, pp. 502–522, 2015.
7. A. Tiraferri, Y. Kang, E. P. Giannelis, and M. Elimelech, “Highly Hydrophilic Thin-Film Composite Forward Osmosis Membranes Functionalized with Surface-Tailored Nanoparticles Highly Hydrophilic Thin-Film Composite Forward Osmosis Membranes Functionalized with Surface- Tailored Nanoparticles ACS Applied Materials,” *ACS Appl. Mater. Interfaces*, vol. 4, pp. 5044–5053, 2012.
8. N. Niksefat, M. Jahanshahi, and A. Rahimpour, “The effect of SiO2 nanoparticles on morphology and performance of thin film composite membranes for forward osmosis application,” *Desalination*, vol. 343, pp. 140–146, 2014.
9. Y. X. Jia, H. L. Li, M. Wang, L. Y. Wu, and Y. D. Hu, “Carbon nanotube: Possible candidate for forward osmosis,” *Sep. Purif. Technol.*, vol. 75, no. 1, pp. 55–60, 2010.
10. M. Amini, M. Jahanshahi, and A. Rahimpour, “Synthesis of novel thin film nanocomposite (TFN) forward osmosis membranes using functionalized multi-walled carbon nanotubes,” *J. Memb. Sci.*, vol. 435, pp. 233–241, 2013.

DOI: https://doi.org/10.26799/cp-nanotechfrance2018

Proceedings of the Nanotech France 2018 International Conference (Nanotech France 2018)
Paris, France, June 27 - 29, 2018
DOI: https://doi.org/10.26799/cp-nanotechfrance2018

Endurance Measurements of Li_xCoO_2-based ReRAM Cells

Van Son Nguyen,[1] Van Huy Mai,[2] Alec Moradpour,[3†] Pascale Auban Senzier,[3] Claude Pasquier,[3] Kang Wang,[3] Marcelo J. Rozenberg,[3] Nathalie Brun,[3] Katia March,[3] Pierre-Antoine Albouy,[3] John Giapintzakis,[4] Christian N. Mihailescu,[4] Evripides Kyriakides,[4] Charis M. Orfanidou,[4] Thomas Maroutian,[5] Guillaume Agnus,[5] Philippe Lecoeur,[5] Silvia Matzen,[5] Pascal Aubert,[5] Sylvain Franger,[6] Raphaël Salot,[7] François Jomard,[8] David Alamarguy,[1] Pascal Chrétien,[1] Pavan Nukala,[9] Brahim Dkhil,[9] and Olivier Schneegans[1]

[1] Lab. de Génie Élect. et Électronique Paris, CNRS, Upmc/PSaclay Univ., CentraleSupélec, Gif/Yvette, France
[2] Departement of Optical Electronic Devices, Le Quy Don Technical University, Hanoi, Vietnam
[3] Laboratoire de Physique des Solides, CNRS, Université Paris-Saclay, Orsay, France
[4] Department of Mechanical & Manufacturing Engineering, University of Cyprus, Nicosia, Cyprus
[5] Centre de Nanosciences et de Nanotechnologies, CNRS, Université Paris-Saclay, Orsay, France
[6] Institut de Chimie Moléculaire et des Matériaux d'Orsay, CNRS, Université Paris-Saclay, Orsay, France
[7] Liten-CEA de Grenoble, Grenoble, France
[8] Groupe d'Etude de la Matière Condensée, Université de Versailles Saint-Quentin-En-Yvelines, Versailles, France
[9] Lab. Structures, Propriétés et Modélisation des Solides, CNRS, CentraleSupélec, Gif-sur-Yvette, France

Abstract
The conductivity of Li_xCoO_2-based cells can be modified by the application of adequate voltages. It is thus possible to switch {electrode/film/electrode} cells reversibly from a high-resistance state R_{High} (initial and highest state of a cell) to a low resistance state R_{Low} (lowest achievable resistance), with a R_{High}/R_{Low} ratio over 2 orders of magnitude. It is also possible to obtain several intermediate resistance states. Hence, this resistive switching (RS) behaviour observed in lithium cobalt oxides appears very interesting towards nonvolatile resistive memories (Re-RAM) in the field of nanoelectronics. Here, we report preliminary results obtained on endurance, which is defined as the maximum number of write/erase cycles possible to achieve without degradation.

Keywords: resistive switching, lithium cobalt oxides, thin films, nonvolatile resistive memories (ReRAM), write/erase cycles, endurance

1. Introduction

A new promising class of Li-based RS materials has recently been observed. Such a class embodies oxide-based RS devices for memristive systems with Li-based nanobatteries [1]. The actual switching mechanism has been a matter of debate, but more detailed studies allowed linking RS with lithium migration [1-3]. Concerning the applicability towards Re-RAM, write/erase endurance (defined as the maximum number of write/erase cycles possible to achieve without degradation) is one of the key parameters to examine. Figure 1 shows an example of cycling (endurance > 1000 cycles), with a R_{High}/R_{Low} ratio > 100.

Proceedings of the Nanotech France 2018 International Conference (Nanotech France 2018)
Paris, France, June 27 - 29, 2018
DOI: https://doi.org/10.26799/cp-nanotechfrance2018

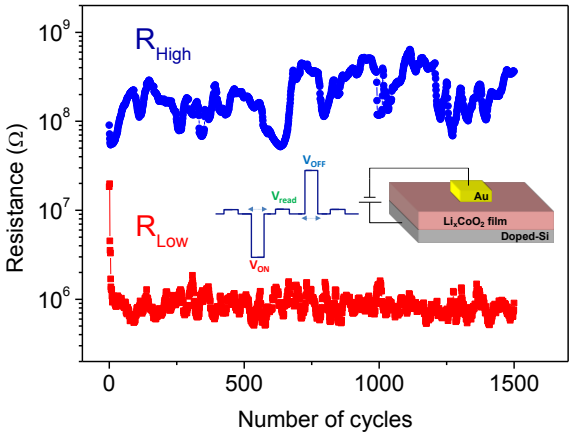

Fig. 1: Endurance measurement of a 100x100 µm {Au / Li_xCoO_2 / doped Si} device. The inset shows the shape of pulses used to switch the device and to measure R_{Low} and R_{High} (at a lower read voltage).

2. Results: influence of pulses shape, current compliance and cell size

2.1. Influence of pulses shape and current compliance

Endurance has been examined for 100x100 µm cells [2]. Either too long pulse duration (>1000ms) or too high voltage (>10V) yields low endurance (<100 cycles) due to breakdown, as can be seen in Figure 2 (left). Hence, towards higher endurance, (-7V/100ms +10V/50ms) pulses have almost been used in following experiments.
Endurance has also been studied as a function of current compliance. For instance, it has been observed that a 0.1mA compliance allows a much longer endurance than a 1mA compliance (Figure 2 right).

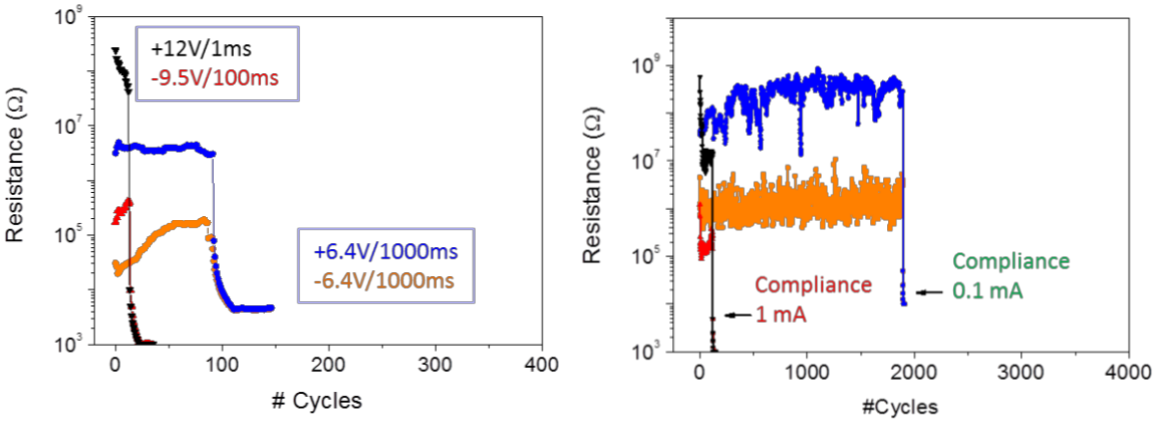

Fig. 2: ***Left*** : Endurance of 100x100µm cells for different switching pulses: (-9.5V/100ms and +12V/1ms) pulses typically lead to an endurance < 50 cycles. Lower voltage but much longer duration (-6.4V/1000ms and +6.4V/1000ms) yields endurance < 150cycles.
Right : R_{High} and R_{Low} states as a function of cycle number, recorded on a 100x100 µm device. For 1mA current compliance, the observed endurance often reaches less than 250 cycles whereas for 0.1mA compliance, the endurance is much higher (~ 2000 cycles).

Proceedings of the Nanotech France 2018 International Conference (Nanotech France 2018)
Paris, France, June 27 - 29, 2018
DOI: https://doi.org/10.26799/cp-nanotechfrance2018

2.2. Influence of cell size

The influence of downscaling appears very promising. Cells of 500×500 µm² only sustain a few hundred cycles (not shown here) after which a very low resistance value is finally reached (the electric field applied is too low to allow switching back to R_{High}). On the contrary, smaller cells of 10×10 µm² far exceed 5000 cycles (see Figure 3). This may be attributed to the fact that the probability of presence of film defects decreases with the downscaling of the cells [3].

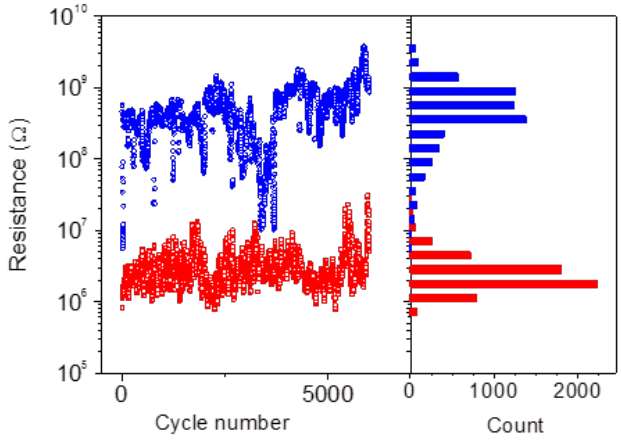

Fig. 3: R_{High} and R_{Low} states as a function of cycle number, recorded on a 10x10 µm device. The endurance reaches beyond 5000 cycles with a R_{High}/R_{Low} ratio ≈1000 [3].

4. Conclusion

Li_xCoO_2, which is widely used in rechargeable batteries, exhibits a resistive switching phenomenon, which appears very interesting for potential applicability to high density nonvolatile data storage.

The influence of parameters such as pulse shape (duration, voltage), current compliance, has been studied; optimized values have been experimentally determined.

The preliminary results concerning R_{High}/R_{Low} ratio and endurance of 10x10µm devices are promising for future applications. Further work is needed to explore the influence of downscaling towards nanoscale.

Acknowledgements

This work was supported by the French National Research Agency (ANR) as part of the "Investissements d'Avenir" program (Labex NanoSaclay, reference:ANR-10-LABX-0035).

References

1. V.H. Mai et al. *Memristive and neuromorphic behavior in a Li_xCoO_2 nanobattery*, Sci. Rep. 5, 7761 (2015).
2. V.S. Nguyen, Ph.D. thesis dissertation, October 20th 2017, Paris-Saclay Univ., France.
3. V.S. Nguyen et al. *Direct Evidence of Lithium Ion Migration in Resistive Switching of Lithium Cobalt Oxide Nanobatteries*, Small, 1801038 (2018)

Proceedings of the Nanotech France 2018 International Conference (Nanotech France 2018)
Paris, France, June 27 - 29, 2018
DOI: https://doi.org/10.26799/cp-nanotechfrance2018

Improved Reaction Activities by Nanofluidic Electrolytes in Vanadium Redox Flow Batteries

Jungmyung Kim[1], Heesung Park[†]

[1] Graduate School of Mechanical Engineering, Changwon Natl. University
20 Changwondeahak-Ro, Changwon-Si, South Korea, sky369iuiu@gmail.com
[†] Department of Mechanical Engineering, Changwon Natl. University
20 Changwondeahak-Ro, Changwon-Si, South Korea, heesungpark@changwon.ac.kr

Abstract

The limitation of energy storage capacity in vanadium redox flow batteries impedes further commercialization of the battery. The concept proposed in this study is to overcome the limit by using nanofluidic electrolytes. Multi-walled carbon nanotubes (MWCNTs) are chosen to disperse in electrolytes due to their high surface to volume ratio. Three nanofluidic electrolytes with different weight percentage of MWCNT (0.05, 0.1, 0.2 wt%) have been tested and compared with pristine electrolyte. Half-cell test with cyclic voltammetry has shown that the electrochemical reaction performance is proportional to the content of MWCNT in nanofluidic electrolytes. The redox reaction of nanofluidic electrolytes are enhanced by the increased electrochemical activity, reversibility and lower polarization effect. The electrochemical performance (peak current density, potential difference, maximum current density ratio) of the half-cell increased proportionally to the particle weight of the nanofluid. We concluded that the nanofluidic electrolytes can considerably improve the energy storage capacity with optimized content of MWCNT.

Keywords: Vanadium redox flow battery, Nanofluid, Electrochemical performance, Multi-walled carbon nanotube

1. Introduction

The current energy supply policy is facing a problem of inconsistency of power demand/supply and limited conditions of large-scale power supply system [1]. The energy storage system is a promising technology to tackle the problem by compromising the power demand and supply. Vanadium redox flow battery (VRFB) is a strong candidate for the ESS application due to the benefits of extensibility, independent capacitance, high energy efficiency, long lifetime, and low cross-over contamination. Various redox couples [2], cell components [3], electrode materials [4], and reduction of side reactions [5] have been under the investigation to increase electrochemical performance. Although the energy storage of VRFB extends to MW which is sufficient for the distributed and smart grid applications, there still requires a breakthrough technology to overcome the low energy storage density of VRFB. Wei et al. visualized the hydrogen evolution reaction which reduced energy storage capacity in VRFB [4]. Nonetheless, lithium-ion battery offers up to 500 Wh/L whereas VRFB does 33 Wh/L due to the limited solubility of vanadium species (1-2 M) [6]. Therefore, progressive technology is required to overcome the limitation of energy storage density in VRFB.

Recently, nanoparticles have drawn attention to increase electrochemically active sites of carbon felt electrode in VRFBs [7-10]. Bismuth nanoparticles [7] and nanorods [8] were employed to replace noble metal with offering high-performance electrodes for VRFBs. Li et al. [9] demonstrated that single-walled carbon nanotubes served as an electrode catalyst for VRFBs. Carbon paper electrode was modified by including a thin layer of multi-walled carbon nanotubes to increase the active area in a location where the electrochemical reaction occurred [10]. Wu et al. proposed cost effective and high-performance electrode by growing N-doped carbon nano-spheres on graphite felt fibres [11]. They demonstrated the superior performances of energy efficiency and capacity retention by conducting single cell test. Li et al. investigated carbon electrode with hollow nanofibers which provided more active sites, higher pore volume, and short diffusion pathways for ions and electrons resulting in enhanced energy storage [12]. Blasi et al. achieved high electrochemical performance in VRFB by using

DOI: https://doi.org/10.26799/cp-nanotechfrance2018

the electrode based on carbon nanofiber with Mn_3O_4 nanoparticles [13]. Meanwhile, nanofluids have been also used to improve thermal properties or lubrication characteristics [14-17]. There have been a few attempts [6,18] to develop electroactive nanofluids for VRFB; however, the impact of the nanofluidic electrolyte on the electrochemical reaction and energy storage has not been addressed yet. The aim of our study is to prove the concept that nanoparticles dispersed in electrolyte can enhance the electrochemical performance and energy storage capacity. In this regard, nanofluidic electrolyte is manufactured by using multi-walled carbon nanotubes (MWCNT). We have chosen MWCNTs as nanoparticles due to their high porosity and surface-to-volume ratio, which offers increased electroactive sites resulting in the enhanced electrochemical kinetics of VRFB. The electrochemical performance has been compared between pristine and nanofluidic electrolytes with different MWCNT concentrations. It is shown that the MWCNT nanofluidic electrolytes significantly increase the reversibility and active area at the reaction zone.

2. Experimental

This research presents the applicability of electrical energy storage devices by analyzing the rheological and electrochemical properties of nanofluids in which nanoparticles are homogeneously dispersed in electrolyte for VRFB.

2.1. Materials

Nanoparticles for nanofluids use commercial MWCNTs (Nanostructured & Amorphous Materials, < 10 nm Diameter, 5-15 μm Length, 95% Purity). The electrolytic solution for VRFB was 1.6 M $VOSO_4$, 4 M H_2SO_4.

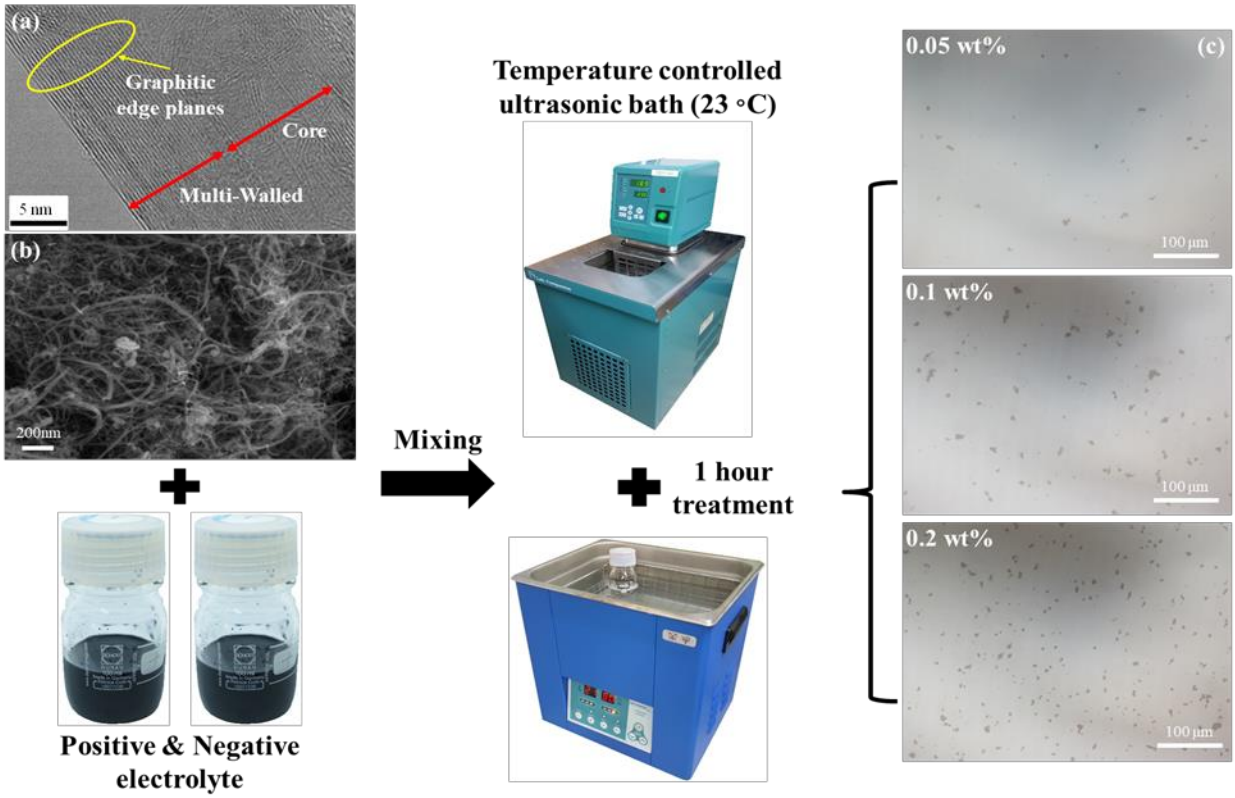

Fig. 1: Schematic diagram of manufacturing process of nanofluidic electrolytes; (a) TEM (b) SEM images; (c) dispersed MWCNTs images by taking sample nanofluidic electrolytes after completion of dispersing process.

2.2. Preparation of nanofluid

DOI: https://doi.org/10.26799/cp-nanotechfrance2018

The increased electrochemical performance of nanofluids is expressed by the multiple graphite edges of MWCNTs. Fig. 1(a) and (b) show the TEM and SEM images of a single MWCNT and MWCNT powder, respectively. As shown in Fig. 1 (c), three different weights of MWCNT powders were homogeneously dispersed by the 490 W sonicator in the pristine electrolytes for comprising 0.05, 0.1 and 0.2 wt% nanofluidic electrolytes, respectively and the dispersion of nanofluidic electrolytes was visually inspected by optical microscopy. And it should be denoted that the temperature of sonicator was kept at 23 ± 1 °C to prevent unwanted precipitation of the electrolyte as illustrated in Fig. 1.

2.3. Electrochemical performance

Half-cell test (NuVant System, Powerstat-05), which are typical for measuring the electrolyte performance, were performed to confirm the electrochemical performance increase according to the nanoparticle content of the electrolyte for VRFB. Half-cell test was performed to observe the change of electrochemical performance of MWCNT nanofluid electrolyte for VRFB.

3. Results

The electrochemical characteristics of the electrolytes constituting the positive and negative electrolyte of the VRFB system were analysed by half-cell. Also, investigate the effect of nanofluidic electrolyte on the electrochemical reaction, CV tests were performed for positive (VO_2^+/VO^{2+}) and negative (V^{2+}/V^{3+}) electrolytes with 0 (pristine), 0.05, 0.1, and 0.2 wt% MWCNT, respectively. Fig. 2(a) and (b) show the oxidation-reduction CV curves when the scan rate was 5 mV/s for the positive and negative electrolytes. It should be denoted that the potential window was defined to 0.2 - 1.6 V (positive electrolyte) and -1.2 – 0.4 V (negative electrolyte). For both of the positive and negative electrolyte, the measured oxidation-reduction peak current densities were in the order of MWCNT content. The increased peak current density was caused by the improved electron transfer kinetics of VO_2^+/VO^{2+} and V^{2+}/V^{3+} couples. Therefore, it can be seen that the electrochemical activities of the positive and negative nanofluid electrolyte were enhanced by increasing MWCNT content. The increased active sites of nanofluid electrolyte also improved the oxidation potential from 1.066 V (0 wt%) to 1.028 V (0.05, 0.1, 0.2 wt%). The nanofluid electrolyte with 0.2 wt% MWCNT exhibited the good electrochemical performance considering large peak current density and small oxidation-reduction potential difference. Although peak current density increased with MWCNT content in electrolyte, the minimum ratio of peak current density and peak potential difference were 1.38 and 0.14 V for 0.1 wt% positive nanofluidic electrolyte.

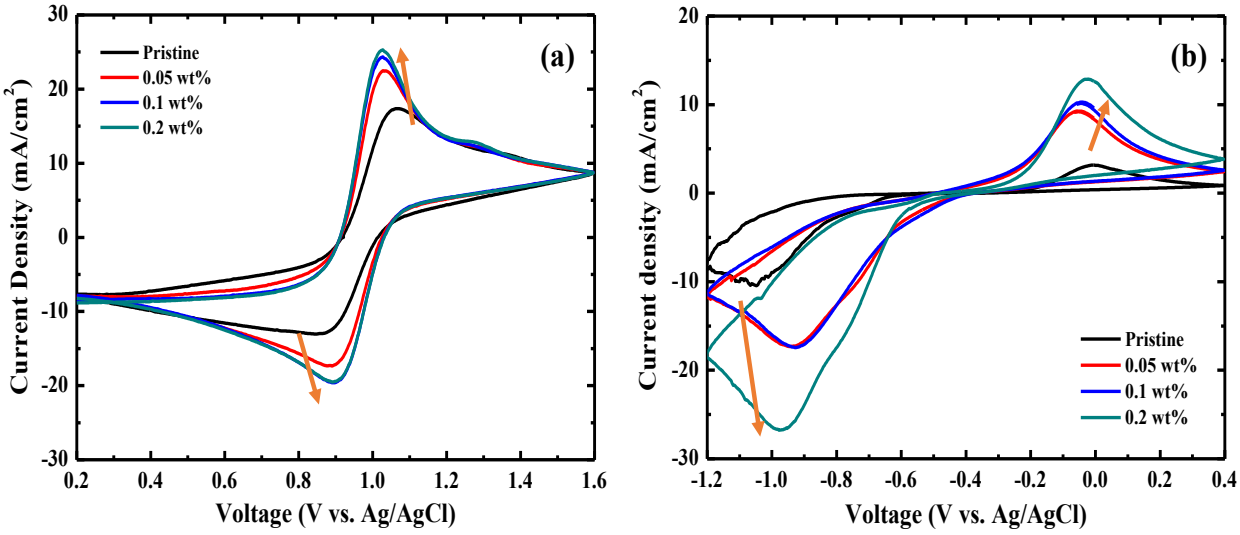

Fig. 2: Cycle voltammograms of the pristine and nanofluid electrolytes; (a) Positive electrolyte, (b) Negative electrolyte at a scan rate of 5 mV/s.

DOI: https://doi.org/10.26799/cp-nanotechfrance2018

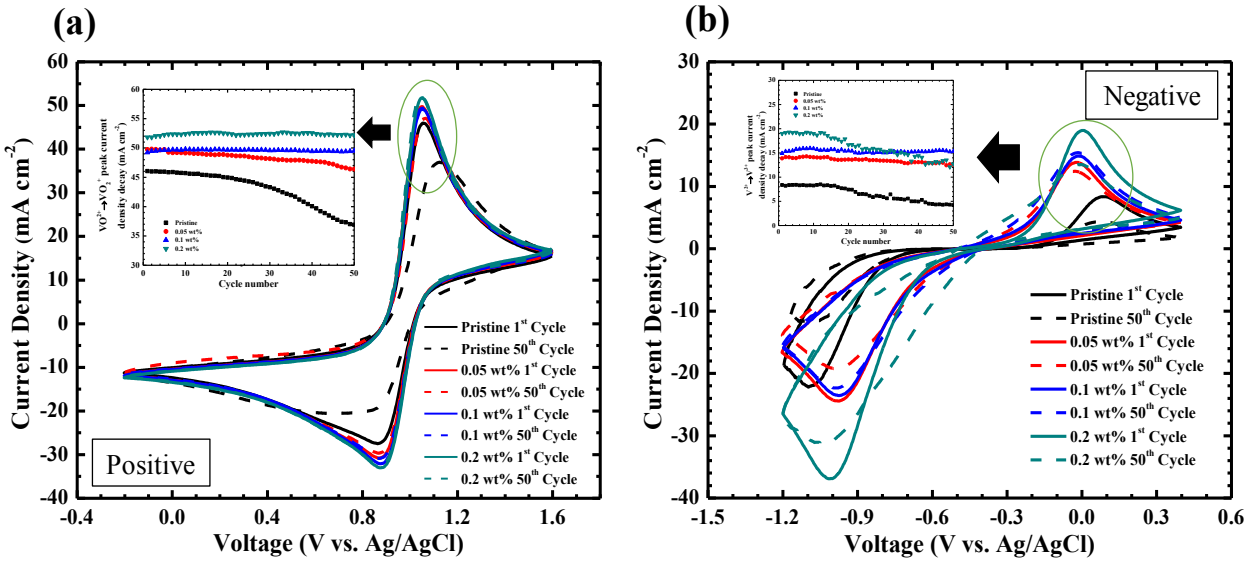

Fig. 3. CV curve for 20 mV/s scan rate and peak current density change over 50 cycles; (a) Positive, (b) Negative electrolyte.

The electrochemical stability of the nanofluid electrolytes were investigated by conducting 50 charge/discharge cycling test. Fig. 3a shows that the peak current densities of positive pristine electrolyte were considerably reduced for oxidation-reduction reaction after 50 charge/discharge cycles, whereas nanofluid electrolytes with 0.1 and 0.2 wt% MWCNT showed unchanged peak current densities during the cycles. Meanwhile, negative pristine and 0.2 wt% nanofluid electrolytes indicated clear reductions of peak current densities after 50 cycles as depicted in Fig. 3b. In this regard, the peak current densities corresponding to the cycle number were displayed in Fig. 3a and b (small figures) for oxidation reaction. It can be found that the reduction ratios of peak current density were 19.8% (pristine), 6.84% (0.05 wt%), 1.11% (0.1 wt%), and 1.61% (0.2 wt%) for positive electrolytes, while the ratios were 50.4% (pristine), 12.9% (0.05 wt%), 6.73% (0.1 wt%), and 37.3% (0.2 wt%) for negative electrolytes. It is evident that the nanofluid electrolytes offered more stable electrochemical reaction after 50 charge/discharge cycles than pristine electrolyte. The MWCNTs dispersed in electrolyte contributed to increase active sites resulting in high stable electrochemi-cal reaction. It is also denoted that the positive and negative nanofluid electrolyte with 0.1 wt% MWCNT showed almost unchanged peak current densities during the cycles indicating minimum irreversible loss.

4. Conclusion

In this study, the experimental results were introduced to present the feasibility of nanofluid electrolyte in VRFB. The MWCNTs were chosen as the nanoparticles to manufacture nanofluid electrolyte. The physio-chemical analysis of the MWCNTs revealed the increased active sites of the electrochemical reaction. CV test was carried out to investigate the electrochemical reaction kinetics of V^{2+}/V^{3+} and VO_2^+/VO^{2+} vanadium redox couples by using nanofluid electrolytes. The measured peak current densities and electric potential differences indicated the improved reversibility and polarization effect resulting in enhanced electrochemical performance in the order of MWCNT content. This research is evaluating the performance of the first nanofluid electrolytes applied to VRFB systems.

Acknowledgements

This work was supported by the National Research Foundation of Korea (NRF) grant funded by the Korea government (MSIT) (No. NRF-2017M1A3A3A02016566)

References

DOI: https://doi.org/10.26799/cp-nanotechfrance2018

1. L. Wei, T. S. Zhao, L. Zeng, Y. K. Zeng, and H. R. Jiang, "Highly catalytic and stabilized titanium nitride nanowire array-decorated graphite felt electrodes for all vanadium redox flow batteries," J. Power Sources, vol. 341, pp. 318–326, 2017.
2. W. Wang et al., "A new redox flow battery using Fe/V redox couples in chloride supporting electrolyte," Energy Environ. Sci., vol. 4, no. 10, pp. 4068–4073, 2011.
3. J. Mun, M.-J. Lee, J.-W. Park, D.-J. Oh, D.-Y. Lee, and S.-G. Doo, "Non-Aqueous Redox Flow Batteries with Nickel and Iron Tris(2,2′-bipyridine) Complex Electrolyte," Electrochem. Solid-State Lett., vol. 15, no. 6, p. A80, 2012.
4. L. Wei, T. S. Zhao, G. Zhao, L. An, and L. Zeng, "A high-performance carbon nanoparticle-decorated graphite felt electrode for vanadium redox flow batteries," Appl. Energy, vol. 176, pp. 74–79, 2016.
5. L. Liu, Z. Li, J. Xi, H. Zhou, Z. Wu, and X. Qiu, "Rapid detection of the positive side reactions in vanadium flow batteries," Appl. Energy, vol. 185, pp. 452–462, 2017.
6. D. P. Dubal and P. Gomez-Romero, "Electroactive graphene nanofluids for fast energy storage," 2D Mater., vol. 3, no. 3, p. 031004, 2016.
7. B. Li et al., "Bismuth nanoparticle decorating graphite felt as a high-performance electrode for an all-vanadium redox flow battery," Nano Lett., vol. 13, no. 3, pp. 1330–1335, 2013.
8. B. Li et al., "Nanorod niobium oxide as powerful catalysts for an all vanadium redox flow battery," Nano Lett., vol. 14, no. 1, pp. 158–165, 2014.
9. W. Li, J. Liu, and C. Yan, "The electrochemical catalytic activity of single-walled carbon nanotubes towards VO_2^+/VO^{2+} and V^{3+}/V^{2+} redox pairs for an all vanadium redox flow battery," Electrochim. Acta, vol. 79, pp. 102–108, 2012.
10. M. P. Manahan, Q. H. Liu, M. L. Gross, and M. M. Mench, "Carbon nanoporous layer for reaction location management and performance enhancement in all-vanadium redox flow batteries," J. Power Sources, vol. 222, pp. 498–502, 2013.
11. L. Wu, Y. Shen, L. Yu, J. Xi, and X. Qiu, "Boosting vanadium flow battery performance by Nitrogen-doped carbon nanospheres electrocatalyst," Nano Energy, vol. 28, pp. 19–28, 2016.
12. L. Li, S. Peng, J. K. Y. Lee, D. Ji, M. Srinivasan, and S. Ramakrishna, "Electrospun hollow nanofibers for advanced secondary batteries," Nano Energy, vol. 39, no. May, pp. 111–139, 2017.
13. A. Di Blasi, C. Busaccaa, O. Di Blasia, N. Briguglioa, G. Squadritoa, and V. Antonuccia, "Synthesis of flexible electrodes based on electrospun carbon nanofibers with Mn_3O_4 nanoparticles for vanadium redox flow battery application," Appl. Energy, vol. 190, pp. 165–171, 2017.
14. E. Sadeghinezhad et al., "A comprehensive review on graphene nanofluids: Recent research, development and applications," Energy Convers. Manag., vol. 111, pp. 466–487, 2016.
15. S. Liang, Z. Shen, M. Yi, L. Liu, X. Zhang, and S. Ma, "In-situ exfoliated graphene for high-performance water-based lubricants," Carbon N. Y., vol. 96, pp. 1181–1190, 2016.
16. C. Hermida-Merino, M. Pérez-Rodríguez, M. M. Piñeiro, and M. J. Pastoriza-Gallego, "Evidence of viscoplastic behavior of exfoliated graphite nanofluids," Soft Matter, vol. 12, no. 8, pp. 2264–2275, 2016.
17. Y. K. Fang et al., "Synthesis and thermo-physical properties of deep eutectic solvent-based graphene nanofluids," Nanotechnology, vol. 27, no. 7, p. 075702, 2016.
18. E. V. Timofeeva, J. P. Katsoudas, C. U. Segre, and D. Singh, "Rechargeable Nanofluid Electrodes for High Energy Density Flow Battery," NSTI-Nanotech, vol. 2, no. May, pp. 679–682, 2013.

Proceedings of the Nanotech France 2018 International Conference (Nanotech France 2018)
Paris, France, June 27 - 29, 2018
DOI: https://doi.org/10.26799/cp-nanotechfrance2018

SiO_2 nanoparticles as a carrier to overcome the cellular delivery of nucleotide drugs

Svetlana Vasilyeva[1], Alexander Shtil[2], Inga Grin[1], Dmitry Stetsenko[1]

[1] Institute of Chemical Biology and Fundamental Medicine, Siberian Branch of the Russian Academy of Sciences, 8 Lavrentiev Avenue, Novosibirsk 630090, Russia, svetlana2001@gmail.com
[2] N. N. Blokhin Cancer Research Centre, Moscow, Russia

Abstract
A drug delivery system based on amino-modified SiO_2 nanoparticles carrying covalently attached triphosphates of nucleoside analogues (dNTP) has been proposed. Conjugates of SiO_2 nanoparticles and phosphorylated dideoxynucleoside antivirals zalcitabine, AZT, lamivudine and ddU (the latter entirely inactive against HIV in its nucleoside form) have been obtained. The conjugates exhibit similar cytotoxicity and cell cycle perturbations in vitro and faster cell accumulation at much lower dose compared with parental drugs, illustrating their therapeutic potential. The results suggest that SiO_2 nanoparticles could be an efficient transport system for delivering phosphorylated nucleosides into cells to increase their potency as antiviral or anticancer drugs.

Keywords: SiO_2 nanoparticles, copper(I)-catalyzed azide-alkyne cycloaddition, phosphorylated dideoxynucleoside analogues, HIV-1, colon cancer cells, cytotoxicity, silica-based biomaterials

1. Introduction

Nucleoside analogues represent the cornerstone of any antiviral regiments and are widely used in cancer chemotherapy. The therapeutic efficiency of nucleoside analogues strongly depends on their intracellular accumulation and conversion into 5'-triphosphate (dNTP). The low conversion results in the development of drug resistance and high toxicity, ultimately compromising the effectiveness of this therapy. A plausible strategy to avoid resistance can be the use of a pre-phosphorylated nucleoside as a drug to bypass intracellular phosphorylation. However, nucleoside triphosphates are very poorly internalized by cells.
Recent advances in nanotechnology have provided a number of nanomaterials for cellular delivery of nucleotides. Because active dNTPs cannot be directly administrated into cell, we present here strategy for their efficient delivery using SiO_2 nanoparticles as a vehicle [1-4]. A simple and versatile method has been developed for the preparation of SiO_2-dNTP conjugates via click chemistry between SiO_2 nanoparticles containing alkyl azide groups and dNTPs bearing alkynylated γ-phosphate group (Fig. 1).

2. Results

2.1. Sythesis

We have proposed a nanocomposite system, in which a nucleotide is covalently attached to the carrier. The system consists of a bioactive nucleoside triphosphate analogue and

- commercially available amino-modified silicon dioxide nanoparticles. In principle, other types of nanoparticles could have been used that meet the requirements.
- copper-catalyzed AAC click chemistry was used to form the covalent bond as this reaction is known for its high yield, selectivity and reproducibility.
- phosphoramidate linkage was used to maintain substrate properties of dNTP for a range of polymerases.

Conjugates of SiO_2 nanoparticles with phosphorylated antiviral drugs zalcitabine, AZT, lamivudine and ddU (the latter entirely inactive against HIV-1 in its nucleoside form) have been obtained (Fig.1).

2.2. Cellular uptake and substrate properties of nanocomposites

Efficient cellular delivery of SiO_2~dNTP conjugates has been demonstrated by laser confocal microscopy. It was shown that the modified nanoparticles and both types of nanocomposites penetrated into the cytoplasm and even into the nuclei

DOI: https://doi.org/10.26799/cp-nanotechfrance2018

of the cells. Almost no cellular uptake of free triphosphates without nanoparticles was observed.The data definitely demonstrated that nucleoside triphosphates bound to nanoparticles were able to penetrate into cells.
A good cell uptake is not sufficient for therapeutic use of the nanocomposites. The triphosphates need to remain the substrates for DNA polymerases. Substrate properties of the nanocomposites were examined using Klenow fragment of E. coli DNA polymerase and HIV-1 reverse transcriptase. We compared the kinetics of polymerization in the reaction mixtures containing four natural dNTPs or three natural dNTPs plus dCTP nanocomposite instead of dCTP. The reaction rate was slightly lower for dCTP nanocomposite instead of dCTP. Some retardation at the initial stage of the reaction could be seen. Interestingly, in the case of Klenow fragment this retardation is significantly more prominent than in the case of HIV reverse transcriptase. It suggests that the nanocomposites are better recognized by viral DNA polymerases than cellular DNA polymerases.

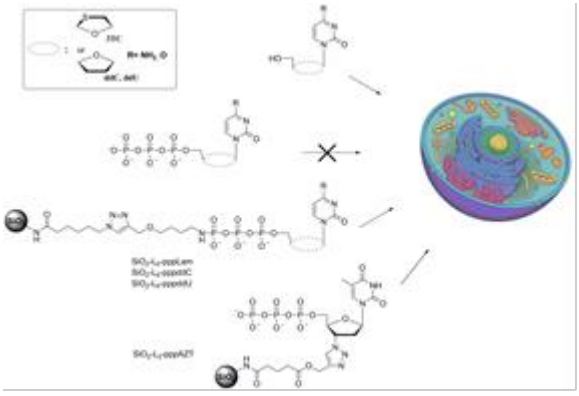

Fig. 1: SiO_2 nanoparticles as a vehicle for delivery of nucleoside triphosphate analogues into cells.

2.3. Anti-HIV-1 properties of nanocomposites SiO_2~pppLam, SiO_2~ppddC and SiO_2~pppAZT
Antiproliferative activity of these nanocomposites was evaluated in human colon carcinoma cell line by MTT test. As expected, the parent lamivudine and ddC exhibited no detectable cytotoxicity whereas nanocomposites of their triphosphates were highly potent. In contrast, the compounds were nontoxic against nonmalignant skin fibroblasts. Nanocomposite of AZT triphosphate was once again less active than AZT itself.

2.4. Cytotoxicity for tumor HCT116 cells vs non-malignant cells
In contrast to inactive parent nucleoside ddU and its triphosphate derivatives, the conjugate of dideoxyuridine triphosphate (pppddU) with SiO_2 nanoparticles was shown to be a potent killer of MCF7 breast adenocarcinoma cells. The results are in agreement with those obtained previously, confirming that cell-penetrating 5'-phosphorylated dideoxynucleoside derivatives can demonstrate much improved and sometimes unexpected properties, for example, more effective inhibition of HIV reproduction. This may lead to re-consideration of the utility of pppddU or other previously ineffective due to the lack of cellular kinases nucleoside analogues as potential anticancer or antiviral drugs after their conjugation to SiO_2 nanoparticles.

2.5. Cytotoxicity of pppddU~L~SiO_2
Nanocomposites of lamivudine and ddC were more active against HIV-1 than the parent nucleosides taking into account the nucleotide loading of the nanoparticles. In addition, ddCTP nanocomposite showed significantly lower toxicity than the parent nucleoside. Nanocomposite of AZT triphosphate was less active against HIV-1 than AZT.

2.6. Accumulation of SiO_2 conjugates of tumor-specific ligands in colon cancer cells HCT116
One of the advantages of our delivery system is the possibility for multi-functionalization. Some of the amino groups can be functionalized with specific ligands for targeted drug delivery. Fluorescein-labeled nanoparticles functionalized with three different tumor-specific ligands (folic acid, biotine aminocaproic acid, 5-F-uracyl) were synthesized. The accumulation of these conjugates in colon cancer cells was studied by flow cytometry. Conjugate with biotine showed cellular uptake a thousand times greater than unmodified nanoparticles. Reduced brightness of conjugates with folic acid and 5-F-uracyl derivative could be attributed not to low uptake but to partial quenching of fluorescence by a ligand due to close location.

DOI: https://doi.org/10.26799/cp-nanotechfrance2018

3. Conclusion

A new type of nanocomposites from SiO_2 nanoparticles and covalently attached phosphorylated nucleoside analogues was obtained. This nanoscale delivery system is easy to prepare. The nanocomposites are able to penetrate into the cytoplasm and even into the nuclei of the cells. A nucleoside triphosphate in the nanocomposite remains the substrate for DNA polymerase. The nanocomposites can be additionally modified with specific ligands for targeted delivery. Our results showed that the nanocomposites possess significant antiviral and anti-proliferative activity. The compounds could be promising candidates for in vivo studies as potential antiviral or anticancer therapeutics.

Acknowledgements

This work has been funded by Russian Science Foundation (grant № 17-44-07003) in the synthesis and study of the antiviral properties of nanocomposites. The synthesis of modified nanoparticles was supported partially by RFBR (grant No. 18-515-05007).

References

1. S. V. Vasilyeva, V. N. Silnikov, N. V. Shatskaya, A. S. Levina, M. N. Repkova, V. F. Zarytova. Bioorg. Med. Chem., 2013, 21, pp. 6101-6114.
2. S. V. Vasilyeva, A. S. Levina, N. S. Li-Zhulanov, N. V. Shatskaya S. I. Baiborodin, M. N. Repkova, V. F. Zarytova, N. A. Mazurkova, V. N. Silnikov. Bioorg. Med. Chem., 2015, 23, pp. 2168-2175.
3. S. V. Vasilyeva, A. A. Shtil, A. S. Petrova, S. M. Balakhnin, P.Y. Achigecheva, D. A. Stetsenko, V. N. Silnikov. Bioorg. Med. Chem., 2017, 25, pp. 1696-1702.
4. S. V. Vasilyeva, I. R. Grin, B. P. Chelobanov, D. A. Stetsenko, Bioorg. Med. Chem.Lett., 2018, 28, pp. 1248-1251.

Proceedings of the Nanotech France 2018 International Conference (Nanotech France 2018)
Paris, France, June 27 - 29, 2018
DOI: https://doi.org/10.26799/cp-nanotechfrance2018

Targeting prostate cancer cells with D2B-gold Nanoparticles

E. Ghanem[1*], M. Sarkis [1], K. Rahme [1], G. Minassian [1], J.D. Holmes [2], H. Y. Naim[3], G. Fracasso[4]

[1]Department of Sciences, Faculty of Natural and Applied Sciences, Notre Dame University, Zouk Mosbeh, Lebanon, [*]eghanem@ndu.edu.lb
[2]Materials Chemistry and Analysis Group, Department of Chemistry University College Cork, Cork, Ireland
[3]Department of Physiological Chemistry, University of Veterinary Medicine of Hannover, Hannover, Germany
[4]Department of Pathology and Diagnostics, University of Verona, Verona, Italy

Abstract
In this study, gold nanoparticles (AuNPs) with an estimate diameter of 25 nm have been synthesized in water using sodium citrate as both reducing and stabilizing agent at ~95 °C and in the presence of sodium hydroxide. The generated AuNPs were characterized using ultraviolet-visible spectroscopy (UV-Vis), dynamic light scattering (DLS) and Zeta potential measurements. Additionally, AuNPs were coated with D2B, a monoclonal antibody (mAb) recognizing an extracellular epitope of the human prostate specific membrane antigen (hPSMA). Binding of antibodies to PSMA induces its endocytosis, thereby marking PSMA as a docking site for the delivery of therapeutic agents. To attain a stabilized and covalent bond between D2B and AuNPs the strong S-Au bond was exploited; so, the sulfhydryl group (SH) in a cysteine of the D2B was utilized. Binding of D2B to AuNPs-citrate colloidal solution caused a red shift with a higher wavelength of about 15 nm in the UV-Vis spectra. Furthermore, as a confirmation of the successful conjugation, DLS revealed an increase in both the AuNPs size from ~25 to ~63 nm and Zeta potential measurements for AuNPs-citrate from ~ -45 mV to -23 mV. The cytotoxicity of D2B-AuNPs was assessed using the WST-1 cell proliferation assay and the agarose gel DNA fragmentation method. Finally, the specific delivery and binding of our customized NPs was tested using flow cytometry and western blot. Our results pave the way for further research using coated NPs as vehicles for drug delivery in *in vitro* as well as *in vivo* models.

Keywords: Gold nanoparticles,antibody, bioconjugation, drug delivery, cellular uptake, prostate cancer, biomedical applications.

1. Introduction

Prostate cancer (PCa) has become a common tumor affecting men, with a high risk above the age of 50 years. In the U.S., prostate cancer is the second leading cause of death in men. Its incidence is largely correlated to age [1], and therefore it is more commonly found in elder men at advanced stages [2]. With millions of people suffering from this disease annually [3], treatment and management of PCa has become a definitive obligation for researchers. Nowadays, chemotherapy is applied systemically for patients who have prostate cancer that has undergone metastasis [4] and this tends to affect healthy tissues along with the tumor of interest resulting in undesirable side effects of treatment [5, 6]. Consequently, there remains a pressing need to further explore the use of targeted therapy in prostate cancer. The new approach for treatment should tackle a more targeted strategy in which the drug or biochemical therapeutic is designed to specifically localize and induce selective killing in tumors. This is referred to as the "magic bullet" approach in which it basically involves the binding of a specific protein receptor that is over-expressed in a tumor, to a drug that is conjugated to a targeting ligand [5]. Among the various proteins associated with prostate cancer, such as ATP synthase, notch receptor [7], androgen receptor [8], and prostate-specific membrane antigen (PSMA), PSMA was shown through screening techniques to be mostly implicated in the diagnosis, management and treatment of the disease [3, 9]. PSMA is a characteristic cell-surface marker of prostate cancer [10] and is found to be overexpressed in the advanced stages of the tumor [11]. The role of PSMA as an enzyme is associated with PCa cells growth, since PSMA hydrolyzes the extracellular polyglutamated folate to mono-glutamic folic acid that is then used by the cells [2]. Moreover, recently, the group of J. Grimm has demonstrated that PSMA activates oncogenic signaling stimulating the metabotropic glutamate receptors by means of the cleavage of vitamin B9. [12]

For this particular reason, we sought to design PSMA targeted gold nanoparticles (AuNPs) that could be used for the treatment of PCa when conjugated to an effective therapeutic payload. Over the years multiple nanosystems have been evaluated for the treatment of cancer; however, our interest in AuNPs mainly emerged due to their significant translational potential in cancer therapy, biocompatibility, small size, and most importantly their safety [13]. Many

DOI: https://doi.org/10.26799/cp-nanotechfrance2018

studies have reported the use of AuNPs for prostate cancer treatment and imaging [14] and have taken advantage of monoclonal antibodies to treat prostate cancer, such as murine J591, 7E11 and human MDX-070 [2, 15]. However, none have reported tagging the AuNPs with antibodies specific for PSMA, such as D2B antibody [16] in order to attain a faster and enhanced selective treatment.

In the present study, AuNPs were coated with D2B and characterized using Zeta potential measurements, UV-Vis spectroscopy, and dynamic light scattering (DLS). To validate the safety of our synthesized gold nanoparticles, two cytotoxicity tests were applied to the prostate cancer cell line PC3-PSMA, namely WST-1 cell proliferation assay and DNA fragmentation analysis by gel electrophoresis. Furthermore, flow cytometry and western blot were applied to confirm the specific binding of D2B to the PSMA receptors and their internalization on the prostatic cancer cells.

2. Materials and Methods

Chemicals

Purified H_2O (resistivity ≈ 18.2 MΩ cm) was used as a solvent. All glassware was cleaned with aqua regia (3 parts of concentrated HCl and 1 part of concentrated HNO_3), rinsed with distilled water, ethanol, and acetone and oven-dried before use. Tetrachloroauric acid trihydrate ($HAuCl_4$, 3H2O), sodium citrate dihydrate ($C_6H_5Na_3O_7.2H_2O$) and sodium hydroxide were purchased from Sigma Aldrich.WST-1 cell proliferation reagent was purchased from Roche. All chemicals were used as received without further purification.

Synthesis of Gold Citrate (AuNP-Citrate) Nanoparticles

A. ***Synthesis of AuNPs-Citrate*** **:** To a 100 mL round flask containing 48 mL of deionized water at 95 °C, 100 µL of NaOH (0.1 M) and 0.961 mL $HAuCl_4$ (13 mM) were added under stiring, followed by the fast injection of 0.625 mL of sodium citrate (0.1 M). The colour of the solution changed from pale yellow to colorless within about 2 mins, then to gray after about 5 mins, then shifted to clear red that deepened with time to deep red wine (~ 30 mins). The solution was kept under stirring for 30 mins after the color was stabilized (deep red) . The obtained nanoparticles have a hydronamic diameter of about 25 nm (size by number from DLS measurement) and a zeta potential of -46 ± 1 mV.

B. Conjugation Protocol**:** To a 50 mL beaker containing 10 mL of the AuNPs-Citrate pristine solution in ice bath, 400 µL of D2B solution (0.099 mg/mL) was added dopwise. The colour of the solution changed gradually from deep red wine to pink violet, the stirring was stopped after about 1 hour of addition. UV-Vis and DLS analysis were performed to confirm the D2B attachement onto AuNPs surface (Figures 1 and 2).

UV-Visible Spectroscopy analysis

Optical spectra were obtained on a UV/Vis Analytikjena SPECORD® 250 PLUS spectrophotometer (300−900-nm range, 0.5 nm resolution).

Dynamic Light Scattering and Zeta Potential measurements

The size distribution and surface charge (zeta potential) of the AuNPs colloidal solutions were determined by dynamic light scattering (DLS) with the Malvern Zetasizer Nano-ZS (model ZEN3600; Malvern Instruments Inc., Westborough, MA, USA) using the default NIBS 173° back scattering technique. The model used in the fitting procedure was based on Mark Houwisk parameters. Data was fitted using the cumulative fit given by the suppliers. Measurements were performed on the pristine solutions of AuNPs (~50 µg/mL) using disposable folded capillary cuvettes at 25 °C. Triplicates of each sample have been made for result comparison efficiency.

WST-1 Cell Proliferation Assay

PC3-PSMA cells (5×10^4 cells/mL) were incubated with various concentrations of D2B-AuNPs. As a control, gold nanoparticles were re-suspended with serum free media. The cells were incubated for 4 hrs in a CO_2 incubator (5% CO_2). All wells were treated with 10µL of WST 1 reagent (Roche), incubated for 2 hrs, and the absorbance was measured at 450 nm using a "*MultiGo-Scan*" ELISA reader.

DNA Fragmentation

PC3-PSMA cells ($2x10^5$ cells/mL) were treated for 4 hrs with the desired concentration of D2B-AuNPs (0, 6, 12, and 20µg/mL), lysed for 25 min on ice (4 °C) and then centrifuged for 27 min at high speed. Phenol Chloroform (1:1) was used to extract the DNA with vigorous vortexing followed by centrifugation at 14800 rpm for 1 min at RT and the top aqueous phase was transferred to a fresh tube.DNA was pelleted with 5M Sodium acetate, 2mL ethanol and centrifuged for 15 min at top speed. The pelleted DNA was resuspended in 60µl of deionized water-RNase solution (0.4 mL water + 5 µl of RNase) and assessed by Nanodrop.

Flow Cytometry

PC3-PSMA cells were seeded at a density of 2 x 10^5 cells/mL prior to a 4 hr treatment with the desired concentration of D2B-AuNPs (0, 6, 12, and 20 µg/ml). Cells were then trypsinized for 1min with 100µl trypsin to dislodge the cells and were resuspended with 200µl of RPMI media. After collecting the cells, 2 µL of FITC was added to each vial and were left to incubate in the dark for 1hr with gentle shaking every 15 min. Samples were read using a PARTEC Cube 8 flow cytometer and data was extracted and further analyzed using the FlowJo software.

Statistical Analysis

The data are reported as means ± SEM and were analyzed by one-way ANOVA. Statistical significance was established at $P < 0.05$, and each experiment was performed and validated at least three times.

3. Results

3.1 Synthesis and Characterization of AuNPs-D2B.

Addition of D2B to AuNPs-citrate colloidal solution caused a red shift (higher wavelength) by about 15 nm in the UV-Vis spectra as shown in Figure 1. This change in colour might be due to the change in the refractive index around the AuNPs as a result to the attachment of D2B [17]. Furthermore, dynamic light scattering (DLS) showed an increase in the AuNPs size from ~25 to about ~ 63 nm (size distribution by number) as a confirmation of the successful conjugation of AuNPs-Citrate with D2B (Figure 2). On the other hand, Zeta potential measurements revealed an increase from ~ -45 mV for AuNPs-Citrate to -23 mV (data not shown).

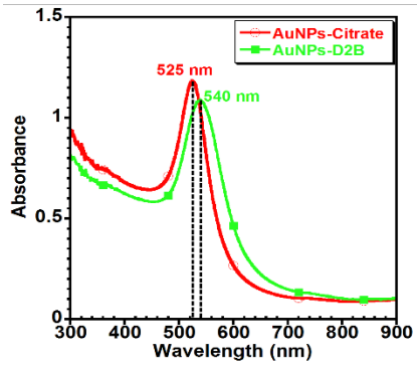

Figure 1. UV-Visible spectra of AuNPs-Citrate (~25 nm) before and after bioconjugation with D2B.

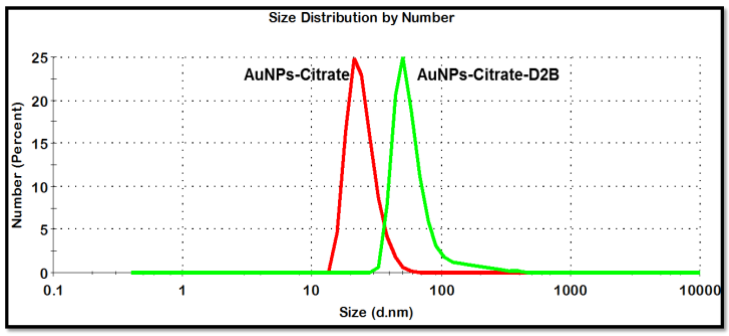

Figure 2. Size distribution by number from DLS on ~ 25 nm AuNPs-Citrate before and after bioconjugation with D2B.

3.2 WST-1 Cell Proliferation Assay

To investigate whether D2B-AuNPs affect the proliferation profile of the prostate cancer cells, a WST-1 reagent was used. The tetrazolium salt, WST-1, is cleaved to a soluble formazan by a cellular mechanism that occurs primarily at the cell surface. This reduction is largely dependent on the glycolytic production of NAD(P)H in viable cells. The results in figure2 support the non-cytotoxic effects of AuNP-D2B, since the absorbance remained almost above 0.5 even after treatment with the highest concentration of AuNP-D2B (20 µg/mL).These results are consistent with the control and correspond to almost 90% survival rate.

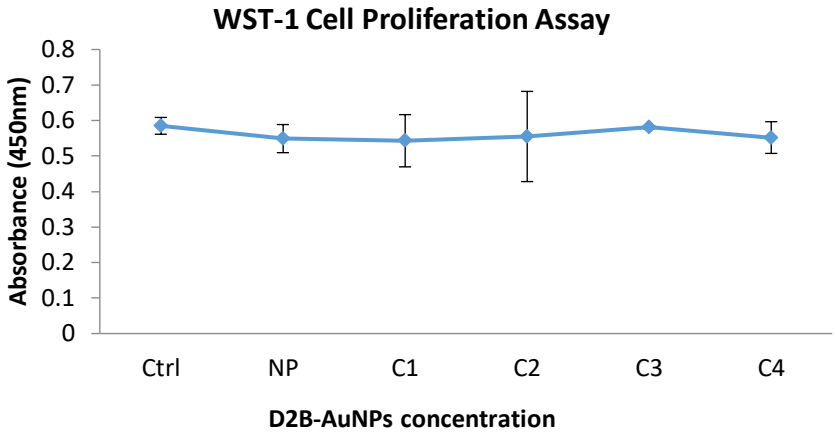

Fig 2: Effect of gold nanoparticles conjugated to D2B antibody (AuNP-D2B) on PC3-PSMA proliferation. Cells treated with variable concentrations of AuNP-D2B: negative control (dH_2O only 20 µg/mL), positive control AuNP at 20 µg/mL, C1=12 µg/mL, C2= 6µg/mL, C3=3µg/mL, C4=1 µg/mL. Proliferation was measured based on WST-1 dye reduction at 450 nm.

3.3 DNA Fragmentation

To evaluate the biosafety and cytotoxic effects of our customized D2B-AuNP, genomic DNA was extracted after treating the PC3-PSMA cells with various concentrations of the NPs ranging between 0 and 20 µg/mL. DNA fragmentation analysis was profiled on a 1 % agarose gel electrophoresis in search for cleaved DNA that is a hallmark of apoptotic cells. The genome remained intact with all the concentrations used as observed by the DNA bands above the 1kb DNA ladder. Therefore, we conclude that our AuNP-D2Bs do not induce apoptosis even at high doses (data not shown).

3.4 Flow Cytometry Analysis

D2B binding to PSMA was tracked by measuring the mean fluorescence intensity (FL1) of a goat monoclonal anti-D2B FITC secondary antibody at the cell surface. Increase in D2B-AuNP concentration induces a dose-dependent increase in FL1 intensity at the surface of PC3-PSMA. Incubating PCa cells with 6 µg/mL of AuNP concentration showed non- significant difference (ns) compared to the control sample. Increasing the concentration of AuNP-D2B to 12 µg/mL and 20 µg/mL resulted in the formation of PSMA-D2B complexes at the cell surface. The 4 hr incubation time period was limiting to internalize all the receptors.

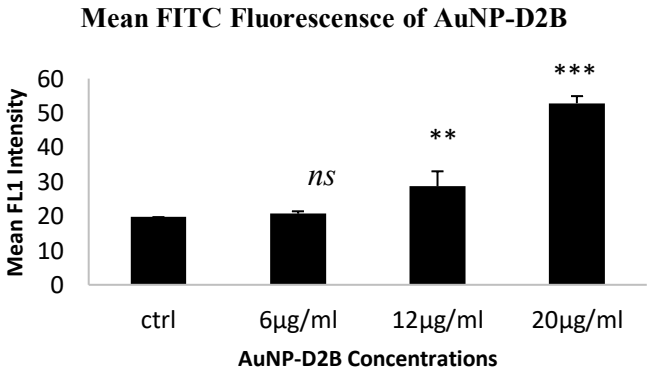

Figure 3: FACS analysis of AuNP-D2B binding to PC3-PSMA. PC3-PSMA cells ($2x10^5$cells/mL) were incubated with increasing concentrations of gold nanoparticles conjugated to D2B (0, 6, 12 and 20µg/ml of AuNP-D2B respectively) for 4 hrs. Using flow cytometry, FITC conjugated secondary antibody (1:500) against D2B was assessed. Fluorescence increased as AuNP-D2B concentration increased (directly proportional). Plots were gated at 50,000 cells per sample (n=3). (ns: non-significant difference)

4. Discussion and Conclusion

DOI: https://doi.org/10.26799/cp-nanotechfrance2018

In the context of targeted prostate cancer treatment, the current study offers an optimized method to conjugate and deliver D2B-coated AuNPs to the surface of prostate cells. The delivery proved to be non-cytotoxic, non-apoptotic, and site specific. Therefore, our results highlight the safe and efficient application of our customized particles *in vivo* to transport therapeutic payloads such as siRNA, chemotherapeutic drugs, or DNA. It remains challenging to test whether the single-chain variable fragment (scFv) of D2B outperforms its complete form with respect to its binding affinity and internalization efficiency.

5. Acknowledgement

We acknowledge financial support from the National Council for Scientific Research Lebanon (CNRS-L-GRP2015 and CNRS-L-GRP2017).

6. References

1. John H. Wasson, et al., *A Structured Literature Review of Treatment for Localized Prostate Cancer.* Arch Fam Med. , 2009. **2**: p. 487-493.
2. William C. Olson, W.D.W.H.a.A.K.R., *Clinical Trials of Cancer Therapies Targeting Prostate-Specific Membrane Antigen.* Reviews on Recent Clinical Trials, 2007. **2**: p. 182-190.
3. Daniyal, M., et al., *Epidemiology, Etiology, Diagnosis and Treatment of Prostate Cancer.* Asian Pacific Journal of Cancer Prevention, 2014. **15**(22): p. 9575-9578.
4. Eton, D.T. and S.J. Lepore, *Prostate cancer and health-related quality of life: a review of the literature.* Psychooncology, 2002. **11**(4): p. 307-26.
5. Flores, O., et al., *PSMA-Targeted Theranostic Nanocarrier for Prostate Cancer.* Theranostics, 2017. **7**(9): p. 2477-2494.
6. Goncalves, A.S., A.S. Macedo, and E.B. Souto, *Therapeutic nanosystems for oncology nanomedicine.* Clin Transl Oncol 2012 **14**: p. 883-890.
7. Pedrosa, A.R., et al., *Notch signaling dynamics in the adult healthy prostate and in prostatic tumor development.* Prostate, 2016. **76**(1): p. 80-96.
8. Marika J. Linja, et al., *Amplification and Overexpression of Androgen Receptor Gene in Hormone-Refractory Prostate Cancer.* American Association for Cancer Research, 2001. **61**: p. 3550-3555.
9. Rajasekaran, A.K., G. Anilkumar, and J.J. Christiansen, *Is prostate-specific membrane antigen a multifunctional protein?* Am J Physiol Cell Physiol, 2005. **288**(5): p. C975-81.
10. Castelletti, D., et al., *Apical transport and folding of prostate-specific membrane antigen occurs independent of glycan processing.* J Biol Chem, 2006. **281**(6): p. 3505-12.
11. Milowsky, M.I., et al., *Vascular targeted therapy with anti-prostate-specific membrane antigen monoclonal antibody J591 in advanced solid tumors.* J Clin Oncol, 2007. **25**(5): p. 540-7.
12. Kaittanis, C., et al., *Correction: Prostate-specific membrane antigen cleavage of vitamin B9 stimulates oncogenic signaling through metabotropic glutamate receptors.* J Exp Med, 2018. **215**(1): p. 377.
13. Jain, S., D.G. Hirst, and J.M. O'Sullivan, *Gold nanoparticles as novel agents for cancer therapy.* Br J Radiol, 2012. **85**(1010): p. 101-13.
14. Mazzocco, C., et al., *In vivo imaging of prostate cancer using an anti-PSMA scFv fragment as a probe.* Sci Rep, 2016. **6**: p. 23314.
15. Sam S. Chang, M., *Overview of Prostate-Specific Membrane Antigen.* REVIEWS IN UROLOGY, 2004. **6**
16. Lutje, S., et al., *Targeting human prostate cancer with 111In-labeled D2B IgG, F(ab')2 and Fab fragments in nude mice with PSMA-expressing xenografts.* Contrast Media Mol Imaging, 2015. **10**(1): p. 28-36.
17. Nghiem, T.H.L., et al., *Synthesis, capping and binding of colloidal gold nanoparticles to proteins.* Advances in Natural Sciences: Nanoscience and Nanotechnology, 2010. **1**(2): p. 025009.